Implementation of an Electrochemical Model for Lithium-Ion Battery Condition Monitoring

DISSERTATION

to attain the academic degree

"DOKTOR DER TECHNISCHEN WISSENSCHAFTEN"

from

Graz University of Technology

Institute of Electrical Measurement and
Measurement Signal Processing

supervisor: Univ.-Prof. Dipl.-Ing. Dr.techn. Georg Brasseur
co-supervisor: Univ.-Prof. Dipl.-Math.techn. Dr.rer.nat. Stefan Volkwein

submitted by: Dipl.-Ing. Martin Sommer

Graz, May 2012

Deutsche Fassung:
Beschluss der Curricula-Kommission für Bachelor-, Master- und Diplomstudien vom 10.11.2008
Genehmigung des Senates am 1.12.2008

EIDESSTATTLICHE ERKLÄRUNG

Ich erkläre an Eides statt, dass ich die vorliegende Arbeit selbstständig verfasst, andere als die angegebenen Quellen/Hilfsmittel nicht benutzt, und die den benutzten Quellen wörtlich und inhaltlich entnommenen Stellen als solche kenntlich gemacht habe.

Graz, am …………………………… ………………………………………………..
(Unterschrift)

Englische Fassung:

STATUTORY DECLARATION

I declare that I have authored this thesis independently, that I have not used other than the declared sources / resources, and that I have explicitly marked all material which has been quoted either literally or by content from the used sources.

……………………………. ………………………………………………..
date (signature)

Acknowledgement

I want to thank my supervisor Univ.-Prof. Dipl.-Ing. Dr.techn. Georg Brasseur for his encouragement as well as the freedom in the formulation of the topic.

Further, I want to thank all members of the Institute of Electrical Measurement and Measurement Signal Processing with special thanks to Dipl.-Ing. Dr.techn. Bernhard Schweighofer and Dipl.-Ing. Dr.techn. Daniel Hrach.

I also wish to thank the ‘COMET K2 Forschungsförderungs-Programm’ of the Austrian Federal Ministry for Transport, Innovation and Technology (BMVIT), the Austrian Federal Ministry of Economics and Labour (BMWA), Österreichische Forschungsförderungsgesellschaft mbH (FFG), Das Land Steiermark, and Steirische Wirtschaftsförderung (SFG) for their financial support.

Additionally, I would like to thank the supporting companies and project partners AVL List GmbH, GAIA Akkumulatorenwerke GmbH, Volkswagen AG, and Virtual Vehicle Competence Center as well as the Institute for Chemistry and Technology of Materials of Graz University of Technology and the Institute of Physical Chemistry of Westfälische Wilhelms-Universität Münster.

In particular I would also like to thank Dr. Jelena Rubesa and Dipl.-Ing Matthias Scharrer from the Virtual Vehicle Competence Center for their support in numerical questions.

Furthermore, I want to thank my second supervisor Univ.-Prof. Dipl.-math.techn. Dr.rer.nat Stefan Volkwein for the technical discussions especially during my short stay at the Department of Mathematics & Statistics at the University of Konstanz as well as his suggestions and comments on this thesis.

Kurzfassung

Neben ihrer großen Bedeutung in der Konsumerelektronik wie z.B. Kameras, Laptops oder Mobiltelefonen kommt der Lithium-Ionen Batterie steigende Bedeutung als Energiespeicher für Elektro- und Hybridfahrzeuge zu. Für einen zuverlässigen Betrieb sowie Erhöhung der Lebensdauer und der damit verbundenen Kostenreduktion, ist eine Zustandsüberwachung der Batterie in Fahrzeugen unerlässlich. Da allerdings nur eine sehr geringe Anzahl an Parametern direkt durch Messungen zugänglich ist, werden leistungsfähige Batteriemodelle, welche das Batterieverhalten exakt wiedergeben können sowie eine klare Trennung der einzelnen chemischen und physikalischen Effekte ermöglichen, benötigt. Deshalb werden in dieser Arbeit sowohl die Entwicklung als auch die numerische Realisierung sowie die Validierung anhand von Messdaten für ein physikalisch-chemisches Modell zur Zustandsdiagnose behandelt. Im ersten Teil der Arbeit werden die elektrochemischen Grundlagen zur Funktionsweise der Batterie kurz zusammengefasst. Des weiteren wird ein Satz gekoppelter partieller Differentialgleichungen basierend auf vorhandener Literatur entwickelt. Der zweite Teil der Arbeit widmet sich der numerischen Realisierung des Satzes von Erhaltungsgleichungen mit besonderem Augenmerk auf numerische Stabilität und Rechengeschwindigkeit. Neben der Integration eines Schemas zur Zeitschrittweitensteuerung und der Verwendung eines modifizierten Newtonschemas werden Wege zur Reduktion des Rechenaufwandes in der Partikeldiffusion aufgezeigt. Zur Validierung des Modells wird im dritten Teil der Arbeit ein Vergleich zwischen Simulation und Messung bei verschiedenen Betriebsbedingungen im Zeit- und Frequenzbereich durchgeführt. Im Zeitbereich ist mit einem rein physikalisch-chemischen Modell ein zu rasches Folgen der simulierten Zellspannung auf Änderungen des Stromes zu beobachten. Wie bei der Bleibatterie wird vermutet, dass dies auf eine unzureichend berücksichtigte Konzentrationsabhängigkeit in den Gleichungen zurückzuführen ist. Im vereinfachenden Impedanzansansatz zur Modellierung einer Batterie wird diese Abhängigkeit durch die sogenannte *Diffusions*- oder *Warburgimpedanz*, welche bei kleinen Frequenzen im Impedanzspektrum auftritt, beschrieben.

Abstract

Besides their important role in consumer electronics such as cameras, laptops or mobile phones, lithium-ion batteries are considered a promising candidate as energy storage for use in electric and hybrid electric vehicle applications. To ensure a reliable use and to extend the lifetime of the battery and thus reducing costs, monitoring of the actual state is an essential task in such vehicles. Furthermore, since only a few quantities are directly accessible by means of measurements a powerful battery model capable to accurately rebuild the battery behavior and further allowing a distinct separation of the underlying chemical and physical processes within the battery is required. Therefore, this work deals with the development, numerical realization and validation of a physico-chemical battery model for condition monitoring applications. In the first part of the thesis the electrochemical fundamentals of the battery are briefly summarized. Further, a set of coupled partial differential equations is developed describing the main processes based on existing literature. The second part of the thesis concentrates on the numerical realization of this set of governing equations with focus on numerical stability as well as calculating speed. Besides the integration of a variable time stepping scheme and the use of a modified Newton scheme the focus is set on reduction of the calculation effort for the particle diffusion. To validate the developed model in the third part of the thesis the obtained simulation results are compared to measurements under various operating conditions in the time and frequency domain. In the time domain it can be observed that with the pure physico-chemical model the simulated cell voltage responds to fast to changes in the input current. Same as for the lead-acid battery it is assumed that this is related to an insufficient incorporation of the concentration dependency in the set of equations. In the simplifying impedance approach for battery modeling this dependency is described by the so-called *Diffusion* or *Warburg Impedance* occurring at low frequencies in the impedance spectrum.

Contents

1. Introduction

1.1. Motivation

Due to their high volumetric and gravimetric energy density lithium-ion batteries have already been established as energy storage in mobile applications such as laptops, cameras or cellular phones in the last two decades. Besides their important role in consumer electronics, lithium-ion batteries are also regarded as promising candidates for use in electric and hybrid electric vehicle applications, given the aspects of legislation on reduction of CO_2 emissions, the worldwide increase of the transport volume and the finiteness of fossil fuels [31]. The advantage of lithium-ion batteries as energy storage in cars originates from their exceptionally high specific energy outperforming competing technologies such as mechanical, electrical or other electrochemical storages even for power-optimized systems distinctively. In fig. 1.1 typical values for specific power and energy of commercially available energy storages are summarized in a so-called ragone diagram assuming a system efficiency of 90 %. Although vehicles with lithium-ion batteries are already available, e.g. Opel Ampera,

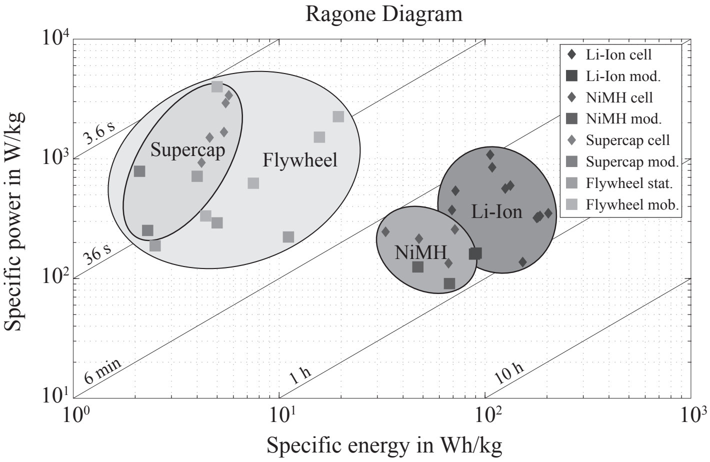

Figure 1.1.: Ragone diagram of common energy storage devices for electric and hybrid electric vehicle applications.

Tesla Roadster, Mercedes S400 Blue Hybrid or the Mitsubishi i-Miev, the battery still remains the crucial component due to high costs, operational safety and lifetime. Thereby, for a reliable use of the energy storage while achieving maximum system efficiency the knowledge of the actual condition of the battery is essential [38]. Based on the actual state of the battery on the one hand the remaining capacity can be predicted and on the other hand predictions can be made on the acceptable current during recuperation as well as the deliverable current during acceleration in order to stay within a specified operating range [16]. This results in an extended lifetime of the battery. Furthermore, monitoring of the battery state allows the early detection of imminent failures of single cells or battery packs allowing to initiate suitable counteractions in time [82].

Since only a few quantities of the battery are directly accessible by measurements such as load current, terminal voltage, temperature or in some cases headspace-pressure for the determination and separation of internal processes as well as monitoring of the actual state of the battery a powerful model capable to accurately predict the battery behavior given these measurements is required. In the following the state of the art of existing battery models is summarized briefly. For further information on the topic of model based condition monitoring it is referred to [93] where it is used for fault diagnosis as well as [86] where a detailed analysis of the relevant quantities and existing strategies for battery condition monitoring is given.

1.1.1. State of the Art of Battery Models

The choice of a suitable model for a particular applications is always a trade-off between calculation time, model accuracy and parametrization effort. Considering these aspects in case of battery modeling, depending on the level of abstraction, a classification into three categories of models can be made.

In the simplest case the battery can be regarded as kind of black box without consideration of the underlying physical processes. Therefore, it is either tried to reproduce the battery behavior directly from measurements by means of curve fitting [20] or some kind of learning models (e.g. neural networks [21] or fuzzy logic [74]). Alternatively, the battery response to a certain input is predicted from data stored in a look-up table [63]. As stated in [46] the main drawbacks of this approach are the huge parametrization effort and the risk of high extrapolation errors outside the measured range. Furthermore, according to [16] black box models are usually restricted to quasi-stationary conditions which is usually not the case in automotive applications.

A more detailed description of the battery can be obtained by the use of an equivalent circuit model. Therefore, using impedance spectroscopy data for the development and parametrization of such a model the most important effects and processes within the battery can be identified and thus being integrated into the model. On the one hand the resulting equivalent circuit can be used to analyze changes in the battery impedance and thus allowing to draw conclusions on the actual state of charge (SOC) and state of health (SOH) [42, 88, 22]. On the other hand, impedance-based battery models are very accurate in reproducing the dynamic behavior of the device [33, 17, 3]. Additionally, equivalent circuit models offer a high versatility and thus can be easily adapted to other kinds of electrochemical energy storages. However, due to the already mentioned strong dependence of the impedance on the battery state (SOC, SOH) as well as temperature, a large amount of measurements is required to parametrize such a model to cover all relevant battery conditions.

Further extending the level of detail finally results in an explicit description of all physico-chemical processes within the battery by means of a set of coupled partial differential equations (PDEs). In case of lithium-ion batteries models of this type are mostly based on the early work of John Newman [27, 32, 28]. Available software solutions based on this set of governing equations are for example the FORTRAN programs of the *Newman Research group* [84], the lithium-ion battery model included in the multiphysics simulation environment COMSOL Multiphysics® [23] or the *Battery Design Studio®* [1] by Robert Spotnitz. Besides the set of equations from Newman there exist also other electrochemical approaches for battery modeling such as e.g. [53, 54] where a mathematical model with focus on thermodynamic consistency is derived, [30, 29] concentrating on many particle modeling and phase transition for $FePO_4$ cathodes as well as [8] dealing with all-solid lithium ion batteries. Compared to the previously described approaches this type of model has the advantage that besides the terminal voltage additional information on internal quantities of the battery such as potential, concentration or temperature distribution depending on the particular load current are obtained. Additionally, since the physico-chemical model can be parametrized on the basis of geometrical as well as material data and not, as the other model types, on measurements in principle the operation range is not limited [46]. Moreover, with increasing computing power of modern PCs and the integration of methods for model reduction as e.g. in [78, 19] the disadvantage of the large computational effort can be overcome, too. However, for a good battery model based on PDEs a detailed knowledge of all underlying processes as well as model parameters is required. Thus, the remaining problems are still the smaller dynamic range compared to equivalent circuit models as well as the difficulties in obtaining some of the required material parameters.

Summarizing, both the equivalent circuit and the physico-chemical model fulfill the requirements for battery condition monitoring in an automotive environment. However, due to the strong cooperation to chemical institutions as well as the access to manufacturer information within the 'COMET K2 project: *Modellierung, Validierung und Test von Lithium-Ionen-Batterien für Hybridfahrzeuge*' allowing the determination of critical model parameters and to ensure a simple extension of the basic model with e.g. thermal or aging models in this thesis a battery model on the basis of the physico-chemical approach is developed. Thereby, the focus of this work is put on improvements on the dynamic behavior as well as model performance with respect to calculation time and robustness.

1.2. Contribution of the Thesis

As stated previously the solution of the coupled set of partial differential equations results in a high computational effort. Therefore, this thesis is focused on the development of an efficient numerical solver based on the control volume (CVM) or finite volume method (FVM) which is particularly suited for the solution of governing equations. Special interest is laid on the solution of the particle diffusion since for that equation only the surface and the average concentration are of interest and not the exact concentration distribution. Two strategies to reduce the calculation effort of that equation have been investigated. The first is based on a change of variables to overcome the nonlinear characteristics of the equation and thus simplifying the integration over the single control volumes published in [79] whereas the second concentrates on point reduction based on a POD analysis [80]. To validate the overall battery model the obtained simulation results are compared to measurements for various operating conditions. From the analysis of the frequency domain behavior same as for the lead-acid battery it is assumed that the deficiencies in the cell response to dynamic excitation are related to an insufficient incorporation of the concentration dependency in the set of equations. In the simplifying impedance approach for battery modeling this dependency is described by the so-called *Diffusion* or *Warburg Impedance*. Based on these findings in [72] an equivalent circuit model of a 70 Ah cell has been developed.

In addition, thesis-related work on the topic of model based condition monitoring has appeared in [93].

Since this thesis is part of the 'COMET K2 project: *Modellierung, Validierung und Test von Lithium-Ionen-Batterien für Hybridfahrzeuge*' fragments that have been developed or extended in cooperation with project partners are explicitly denoted.

1.3. Outline

Chapter 1 gives a short review on existing battery models with respect to their applicability for condition monitoring systems on the basis of which the physico-chemical based approach has been chosen as the most promising candidate to meet the requirements posed on such a system. Moreover, to obtain a deeper insight in the functionality of the battery in chapter 2 the electrochemical fundamentals and underlying processes are summarized. Concluding the first part of the thesis in chapter 3 a set of coupled partial differential equations based on a review on modeling of lithium batteries given in [89] is presented.

The second part of the thesis deals with the numerical realization of the previously defined set of governing equations as well as the validation of the battery model by comparing the simulation results to measurement data for various test cases. Therefore, in chapter 4 starting from a basic implementation a great effort in improving the model performance with respect to robustness and calculation speed has been made. In chapter 5 the obtained simulation results are validated for a 50 mAh pouch cell covering an analysis of the long term as well as the dynamic behavior of the cell by comparing the measurements to the simulation both in the time and frequency domain. Finally, in chapter 6 a summary of the thesis together with a short outlook to possible future work including some further model improvements for a reliable condition monitoring system is given.

2. Electrochemistry of a Lithium-Ion Battery

Secondary or rechargeable lithium-ion batteries consist of two porous electrode materials and an ion-conducting eletrolyte as well as an electronically insolating separator. The chemical reactions inside the battery can be described by the so-called reaction equations. The transition from electronic to ionic conduction is described by the kinetics of the electrode. Both effects are described briefly in the following chapter.

2.1. Electrochemical Reactions

Depending on geometrical properties such as particle size or electrode thickness lithium-ion batteries can be divided into high power and high energy cells. If the particles of the active material are very small the surface where the electrochemical reaction takes place is very big. Thus, high discharge currents can be achieved. On the other hand when the particles are big more lithium can be stored in a single particle and a high energy density can be achieved. Throughout this thesis lithium iron phosphate ($LiFePO_4$) is used as electrode material for the positive electrode and carbon (LiC_6) for the negative. $LiFePO_4$ with its nanosized particles is mainly used in high-power batteries. The active material was patented first in 1999 by John Goodenough [35]. The major advantages of the material including safety aspects, non-toxicity and low price are summarized and compared to other common cathode materials in [69].

2.1.1. Insertion Process

In contrast to many other battery technologies in lithium-ion batteries the active electrode material is not chemically transformed but the Li^+ ions are inserted/deinserted directly in the structure of the active electrode material. Thus, the lattice of the host material suffers only from minor (LiC_6) or even no ($LiFePO_4$) structural changes related to lithium insertion and is not chemically transformed due to current flow.

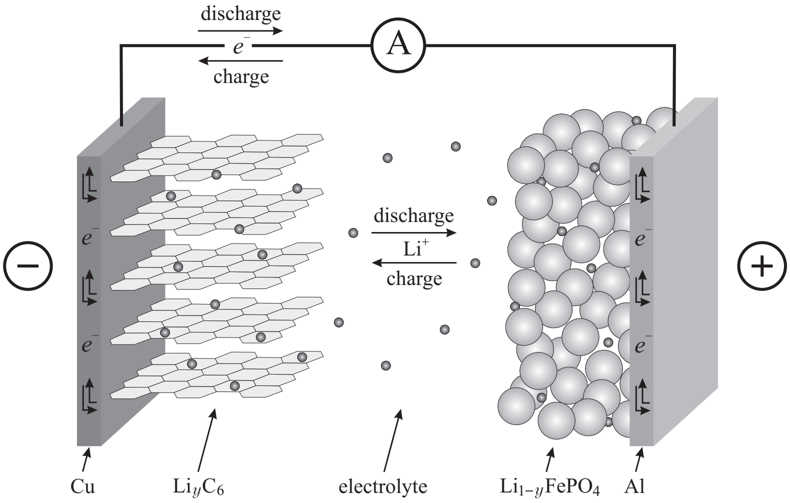

Figure 2.1.: Schematic of a graphite (LiyC$_6$)/lithium iron phosphate (Li$_{1-y}$FePO$_4$) cell on the basis of [82] with the dimensionless parameter $y \in [0,\ 1]$ indicating the amount of lithium stored in an electrode.

During discharge the Li$^+$ ions inside the negative electrode are deinserted from the active material to the electrolyte whereas in the positive electrode the opposite reaction, insertion of Li$^+$ ions into the active material, takes place. Due to the resulting concentration gradient the lithium ions are driven from the negative to the positive electrode. Because of the nonconducting separator the electrons are forced to use a different path via an electric circuit. This basic principle of operation is depicted in fig. 2.1 showing the transport of only the Li$^+$ cation in the electrolyte. The intercalation of the solvated Li$^+$ ion into the host structure of the anode is shown in more detail in fig. 2.4 after [10].

Similar to the layered metal oxide LiCoO$_2$ versus hard carbon described in [16] the reaction equations for the phospho olivine compound LiFePO$_4$ versus LiC$_6$ can be written as follows with

$$\mathrm{Li}_y\mathrm{C}_6 \quad \underset{\text{charge}}{\overset{\text{discharge}}{\rightleftharpoons}} \quad \mathrm{C}_6 + y \cdot \mathrm{Li}^+ + y \cdot \mathrm{e}^- \tag{2.1}$$

$$\mathrm{FePO}_4 + y \cdot e^- + y \cdot \mathrm{Li}^+ \quad \underset{\text{charge}}{\overset{\text{discharge}}{\rightleftharpoons}} \quad \mathrm{Li}_y\mathrm{FePO}_4 \tag{2.2}$$

representing the electrode reactions and

$$\mathrm{Li}_y\mathrm{C}_6 + \mathrm{FePO}_4 \quad \underset{\text{charge}}{\overset{\text{discharge}}{\rightleftharpoons}} \quad \mathrm{C}_6 + \mathrm{Li}_y\mathrm{FePO}_4 \tag{2.3}$$

the overall cell reaction. The dimensionless parameter $y \in [0,\ 1]$ indicates the amount of lithium stored in an electrode with the two boundaries 1 and 0 representing a fully charged/discharged electrode, where either no more lithium can be inserted or deinserted.

Due to the layered structure of the graphite electrode the intercalation process of lithium into the graphite structure occurs at several stages s denoted by roman numerals. This results in a stepwise profile of the potential curve versus lithium for galvanostatic (i = const.) conditions at low current depicted in fig. 2.2 with y being the normalized amount of lithium stored in the electrode and thus also being a measure for the state of charge of the electrode, s the actual stage and t time according to [95]. The plateaus are indicating two-phase regions. Additionally, due to the intercalation of lithium into the host structure of the graphite according to [96] the volume of the electrode is changing by $\sim$ 10% between the lithiated and delithiated state. A detailed description of the intercalation process of lithium into graphite can be found in [89] and [95].

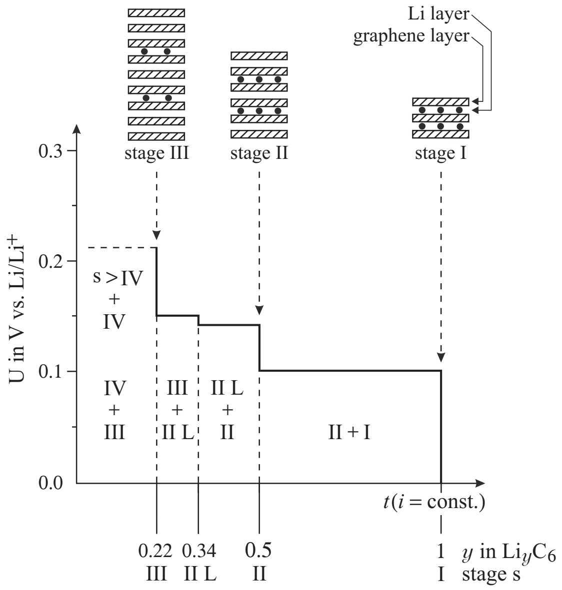

Figure 2.2.: Stage formation of the potential of the graphite electrode versus lithium under galvanostatic (i = const.) conditions at low current related to lithium intercalation into graphite with y being the normalized amount of lithium stored in the electrode and thus being also a measure for the state of charge of the electrode, s the actual stage and t time. The plateaus are indicating two-phase regions. Modified from [95].

2.1.2. Electrolyte Processes

Apart from the transport of the positively charged Li^+ ions in the electrolyte the transport of negatively charged ions such as e.g. PF_6^- from the conducting salt has to be considered. Thus, electroneutrality within the battery is setting up due to the PF_6^- ions within the electrolyte compensating the charge of the Li^+ ions. The conducting salt is added to the solvent mixture to overcome the low conductivity of the electrolyte by increasing the number of charge carriers. Nevertheless, the conductivity of the electrolyte can not be increased in any order because an increase of conducting salt leads to a reduction of free ions due to ion pair formation together with an increase of the viscosity. Figure 2.3 shows a measured conductivity curve passing through a maximum at ∼1.2 mol/l. According to [45] to the left side of the maximum the lack of ions leads to solvent excess whereas to the right side of the maximum the lack of free ions due to ion pair formation together with the increased viscosity leads to salt excess.

In [89] the reaction equations for several solvent mixtures and conducting salts together with common side reactions due to various contaminants in the solvent mixture are summarized. For the battery under consideration the combination ethylene carbonate/ethylmethyl carbonate (EC/EMC) for the solvent and $LiPF_6$ for the conducting salt is used. The reaction equation for the salt together with the side reaction

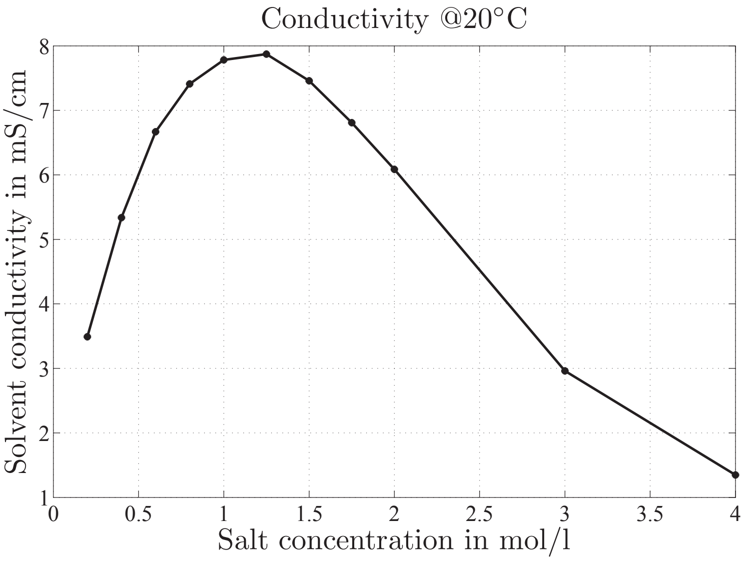

Figure 2.3.: Measured conductivity curve of the electrolyte with a maximum conductivity near 1.2 mol/l.

for water contamination can be summarized as follows

$$LiPF_6 \rightleftharpoons LiF + PF_5 \tag{2.4}$$

$$PF_5 + H_2O \rightarrow PF_3O + 2HF\ . \tag{2.5}$$

The occurrence of hydrogen fluoride (HF) is related to a leakage in the battery housing allowing water to diffuse into the interior of the battery and thus reducing the lifetime of the battery. A detailed mathematical description of the ionic transport in the electrolyte of a lithium-ion battery considering both Li^+ and PF_6^- diffusion is given in [24].

2.1.3. Surface Film Formation

Surface films play a key role in lithium as well as lithium-ion batteries because their operating voltage lies beyond the thermodynamic stability limit of todays electrolyte systems. Further decomposition of the electrolyte is prevented by the formation of such an electrically insulating ‘passivating’ film at the interface of the negative electrode and the electrolyte. At the same time this ‘protective layer’ is selectively permeable for electrochemically active Li^+ ions but ideally impermeable to any other electrolyte component thus behaving as a solid electrolyte interface (SEI), as proposed by [65]. A schematic representation of the SEI in organic solvent-based electrolytes consisting of an electrolyte permeable porous organic layer of poly- and oligomeric decomposition products and an electrolyte impermeable compact layer of inorganic decomposition products such as lithium fluoride (LiF) and lithium carbonate (Li_2CO_3) is shown in fig. 2.4 based on [10]. The properties of an ‘ideal’ SEI can

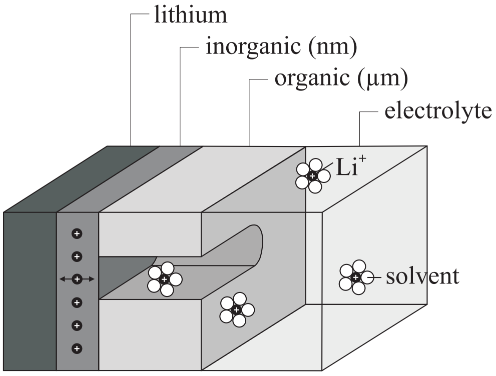

Figure 2.4.: Schematic representation of protective surface film on Li or Li_yC_n anodes in organic electrolytes known as SEI (modified from [10]).

be summarized after [9] and [47] as follows:

- high ionic conductivity for Li^+ cations (t_+ close to 1)
- electrically insulating to prevent further electrolyte decomposition
- well adherent and flexible
- little charge capacity consumption during SEI formation

A more detailed description on the formation mechanisms and composition of surface films in lithium-ion batteries as well as a mechanistic modeling approach of SEI growth can be found in [5] whereas in [4] a simplified model based on film resistances is introduced.

2.1.4. Aging Mechanisms

According to [89] the aging of a battery can be defined as the modification of its properties with time and use. These modifications can lead to an increased cell impedance on the one hand and a decreased cell capacity on the other hand resulting in a reduced power capability and energy content respectively.

Further, as stated in [89] two different aging situations can be distinguished – aging during storage determining the ‘calendar’ life of the battery, and aging during cycling determining the battery’s ‘cycle’ life. Generally, aging during cycling can be described by the degradation of the active material due to lithium insertion/deinsertion, while aging on storage is mainly related to side reactions on the interface between the electrode and the electrolyte depending on SOC as well as temperature. Although both aging situations are mostly considered as additive interactions may definitely occur as stated in [89].

According to [81] the temperature dependency of capacity fade during aging under storage conditions is considered to be of the Arrhenius type

$$\Delta Q = K e^{\left(-\frac{E_a}{RT}\right)} t^z \tag{2.6}$$

with ΔQ being the irreversible capacity loss in %, E_a the activation energy of the chemical process, R the gas constant, T the temperature, t the time, and K a constant. This relation was modified by [11] by introducing the additional parameter z as the exponent of time and thus getting the percentual increase in impedance or percentual loss in power respectively with $z = 0.5$ being typical for diffusion limitation or layer growth. A different approach for modeling the capacity fade of a lithium-ion battery is given in [15] where the corrosion of lithium is investigated following the equation

$$t = \frac{B}{2n\kappa A_{\mathrm{elec}}}\chi^2 + \frac{L_0}{n\kappa A_{\mathrm{elec}}}\chi \tag{2.7}$$

with A_{elec} being the interface area of the anode, κ the specific electronic conductivity of the layer, χ the amount of lithium corroded, L_0 the initial layer thickness, t the time, and n and B coefficients of proportionality. While all these methods focus on aging under storage conditions [70] concentrates on the capacity fade during cycling at elevated temperatures based on a simple physics-based model.

Aging Mechanisms on the Anode

According to [90] aging on the anode is considered to be mostly related to changes at the anode/electrolyte interface due to reactions of the anode with the electrolyte. The dominant aging mechanisms on carbon-based anodes including impedance rise due to SEI formation and growth, lithium corrosion leading to self-discharge and loss

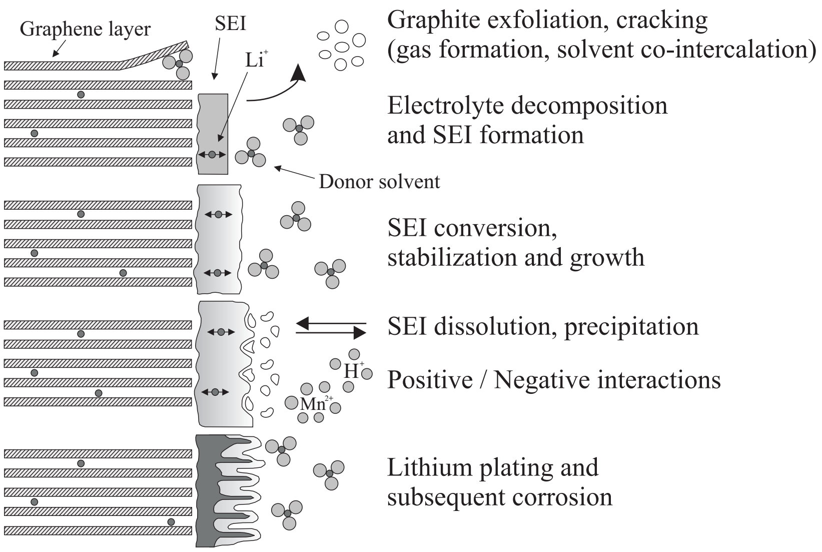

Figure 2.5.: Summary of basic aging mechanisms on the carbon anode due to changes at the anode/electrolyte interface according to [90].

of mobile lithium, and lithium plating occurring at low temperatures as well as inhomogeneous current or potential distribution are depicted in fig. 2.5 after [90].

Aging Mechanisms on the Cathode

Cathode aging is strongly dependent on the composition of the electrode and can be considered as a sum of effects influencing each other making it nearly impossible to study them separately. In [90] aging of the active material itself, degradation of inactive electrode components, the oxidation of electrolyte components, and interaction of aging products with the negative electrode are summarized as the main aging mechanisms on the cathode depicted in fig. 2.6.

According to [47] lithium iron phosphate shows minor aging effects compared to other cathode materials because on the one hand the host material does not undergo any structural changes and on the other hand loss of mobile lithium has not been observed. Thus, aging of the carbon-based anode material can be considered to be the main source of aging for the lithium ion battery investigated.

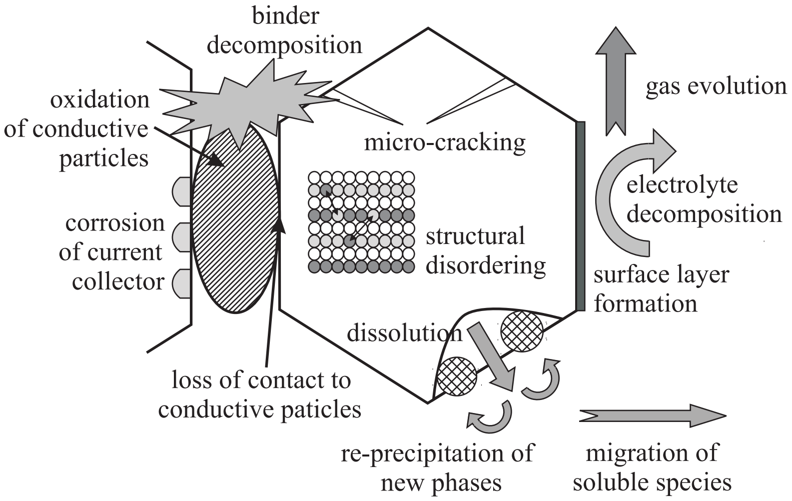

Figure 2.6.: Summary of basic aging mechanisms on the cathode according to [90].

2.2. The Open Circuit Voltage

If an electrode is operating at nearly currentless state, e.g. by discharging with an infinite load resistor, the electrochemical processes within the electrode are completely reversible. Thus, the potential obtained is always equal to the equilibrium or open circuit voltage (OCV). As stated in [6] the resulting change in the standard free energy ΔG^0 is given by

$$\Delta G^0 = -nFU^0 \tag{2.8}$$

with n the number of electrons involved in the reaction, Faradays constant F, and the open circuit voltage U^0. Additionally, the change in standard free energy can be regarded as the driving force to be able to deliver electrical energy according to [56]. To be able to deal with conditions different from the standard state the potential can be obtained by the Nernst equation

$$U = U^0 + \frac{RT}{nF}\ln\frac{\prod a_{\mathrm{ox}}}{\prod a_{\mathrm{red}}} \tag{2.9}$$

with a_{ox} representing the activities of the oxidized species and a_{red} the activities of the reduced species respectively. Because the activity coefficients are mostly unknown often the concentrations of the oxidized and reduced species together with a measured OCV curve are used instead.

2.3. Electrode Kinetics

The theoretical electrical energy deliverable by an electrode is defined by the standard free energy given in equ. 2.8. However, this theoretical value can only be achieved at very low discharge rates. By increasing the discharge current density i the voltage in each electrode u_{elec} is striding away from the open circuit voltage U^0 due to polarization effects including activation polarization due to charge transfer at the electrode/electrolyte interface (η_{ct}) and concentration polarization due to diffusion effects (η_{d}) as well as the 'ohmic polarization' or IR drop (η_{IR}). Under operating conditions when the battery is connected to an external load the effective achievable voltage of each electrode u_{elec} can be described by

$$u_{\mathrm{elec}} = U^0 - (\underbrace{\eta_{\mathrm{IR}}}_{iR_i} + \eta_{\mathrm{ct}} + \eta_{\mathrm{d}}) \tag{2.10}$$

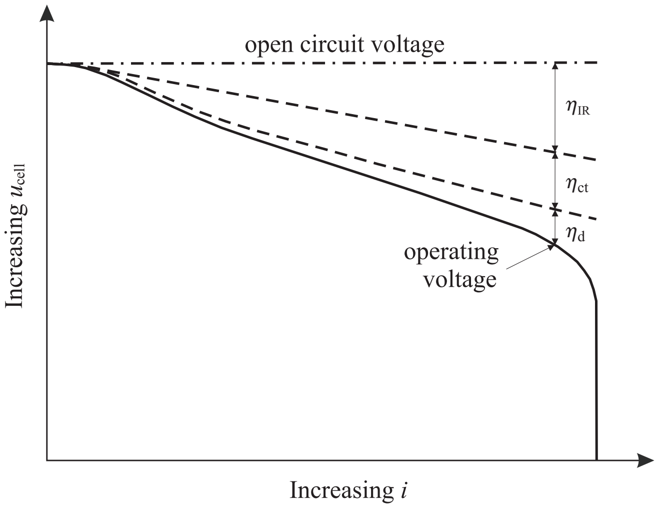

Figure 2.7.: Drop of the available cell voltage u_{cell} summarizing polarization effects in both electrodes and the electrolyte including activation polarizations (η_{ct}), concentration polarizations (η_{d}) and 'ohmic polarizaion' (η_{IR}) versus discharge current density i after [56].

considering polarization effects as well as the IR drop caused by the inner resistance R_i of the battery. In R_i the ionic resistance of the electrolyte, the electronic resistance of the active electrode material and the current collector as well as the contact resistance between the active material and the current collector are summarized. The effective cell voltage can then be obtained as the potential difference between the current collectors of both electrodes. In fig. 2.7 the relation between the operating voltage u_{cell} and discharge current density i is shown graphically summarizing the losses in both electrodes as well as the electrolyte according to [56].

2.3.1. Butler-Volmer Representation

For the derivation of the activation polarization it is assumed that only one electron is transferred at the interface between the species O and R according to [6]

$$O + e^- \underset{k_f}{\overset{k_b}{\rightleftharpoons}} R \tag{2.11}$$

with O being the oxidized and R the reduced species respectively. The reaction rate coefficients for the forward k_f and backward k_b reaction are resulting from the theory of the activated complex considering the change in the standard free energy from the initial state to the activated complex explained in [37]. In fig. 2.8 the change in the standard free energy $F\eta$ related to a potential shift η is shown. By analyzing the intersection region between the oxidized and the reduced species of the redox system the total change in the standard free energy can be divided into a forward $\alpha F\eta$ and a backward fraction $(1-\alpha)F\eta$ according to

$$\Delta G_f^0 - \Delta G_f = \alpha F\eta \tag{2.12}$$

$$\Delta G_b^0 - \Delta G_b = -(1-\alpha)F\eta \tag{2.13}$$

with $\alpha \in [0,\ 1]$ being the transfer coefficient assuming same as in [6] a one-step one-electron process. Using the definitions for the rate constants k_f and k_b of the Arrhenius type from [6] and considering no limitation by mass transfer effects this theory leads to the current-potential relation known as Butler-Volmer equation

$$i = i_0 \left[e^{\frac{\alpha F}{RT}\eta} - e^{-\frac{(1-\alpha)F}{RT}\eta} \right] \tag{2.14}$$

with i_0 being the exchange current density and η the deviation from the OCV. Due to the nonlinear characteristic of equ. 2.14 for a high overpotential η either the forward or the backward term, depending on the sign, can be neglected leading to a simplified form of the equation.

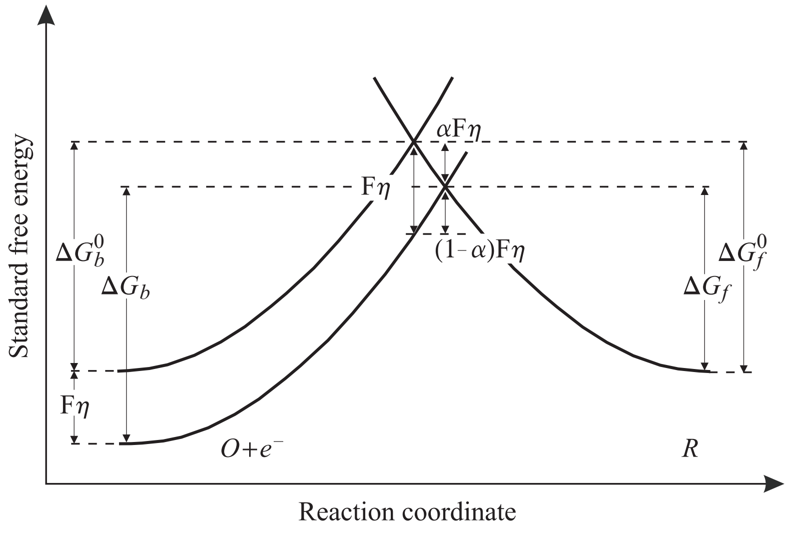

Figure 2.8.: Change in the standard free energies $\alpha F\eta$ and $(1-\alpha)F\eta$ related to a potential shift η for a redox system. Modified from [6].

2.3.2. Influence of the Electrochemical Double Layer

On the interface between the electrode and the electrolyte separation of charge occurs by forming a layer of charge in both species. This region is called the electrical double layer. Basically the electrical double layer can be divided into a compact (Helmholtz) and a diffusive (Gouy-Chapman) layer depicted in fig. 2.9 together with the potential distribution at the interface between the electrode (ϕ_s) and the solvent (ϕ_ℓ) due to charge separation. A detailed description of modeling approaches of the electrical double layer is given in [6, 37, 56].

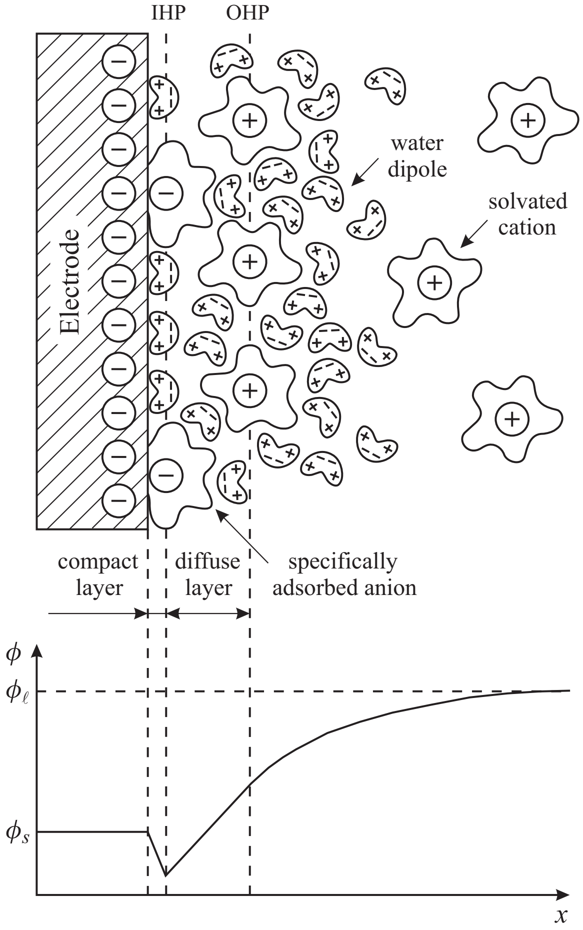

Figure 2.9.: Electrical double layer consisting of a compact (Helmholtz) and a diffusive (Guy-Chapman) layer together with the potential distribution at the interface between electrode and electrolyte. Modified from [45].

In this thesis, however, the simplest representation of the electrical double layer considering only the compact layer is used. This approach is comparable to a capacitor with a distance between the plates equal to the dimension of the compact layer. The current-voltage characteristics of the electrical double layer can then be described by

$$i = C_{\mathrm{dl}} \frac{\partial(\phi_s - \phi_\ell)}{\partial t} \tag{2.15}$$

with C_{dl} being the capacitance at the interface called double-layer capacitance.

2.3.3. Mass Transfer Limitation

During current flow a concentration profile c_ℓ is formed from the phase interface into the bulk. Thereby, the concentration on the interface is decreasing from the initial value c_ℓ^0 to a new value c_ℓ^{surf} depending on the allowed overpotential. The region where this concentration gradient is formed is called the Nernst diffusion layer δ_N. Its thickness is defined by the intersection of the tangent to the concentration profile at the interface to the initial horizontal profile c_ℓ^0 from [37]

$$\delta_N \quad = \quad \frac{c_\ell^0 - c_\ell^{\mathrm{surf}}}{(\partial c_\ell / \partial x)|_{(x=0)}} \; . \tag{2.16}$$

In Figure. 2.10 the movement of the concentration profile into the interior of the solution is shown for two cases 2 and 3 with 2a and 3a representing stationary conditions. Additionally, the current density is approaching its limiting value i_{lim} as the concentration on the surface is approaching 0 depicted in curves 3 and 3a. This

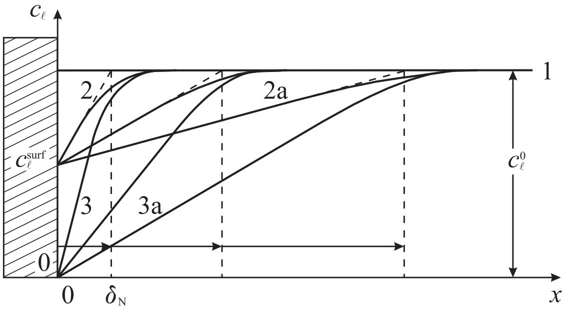

Figure 2.10.: Formation of a concentration profile during current flow for two cases 2 and 3 with 2a and 3a representing stationary conditions and δ_N being the thickness of the Nernst diffusion layer. In curves 3 and 3a the limiting current is applied. Modified from [37].

region where $c_\ell^{\mathrm{surf}} \rightarrow 0$ which goes along with an increased overpotential is called limiting current region. Because in that case the charge transfer reaction is fast compared to the diffusion process the overpotential can be reduced to the diffusion overpotential η_d. From the *Nernst Equation* η_d can be calculated as follows

$$\eta_d = \frac{RT}{F} \ln \frac{c_\ell^{\mathrm{surf}}}{c_\ell^0} \tag{2.17}$$

using the fraction between the concentration on the interface c_ℓ^{surf} and the bulk c_ℓ^0.

3. Mathematical Model Formulation

Whereas in the previous chapter the electrochemistry of a lithium-ion battery was discussed, this chapter provides a purely mathematical description of the previously described mechanisms in the battery. The model equations investigated are mostly based on a review on mathematical modeling of lithium batteries summarized in [89]. Since within the framework of this thesis only a fundamental mathematical description of the lithium battery will be given for a detailed deviation of the underlying theories and concepts it is referred to [61].

3.1. Model Simplifications

Due to the complexity of the internal processes within the battery in the following the assumptions made on the physics of the battery with focus on finding a trade-off between complexity and accuracy of the resulting model with focus on the current-voltage behavior are summarized in accordance to existing literature on battery modeling.

3.1.1. General Assumptions

As already stated in [71] for the lead-acid battery, the lithium-ion battery is considered as a closed system treated as isothermal. An additional thermal model considering electrochemical heat generation within the battery as well as heat transfer to the surroundings via the surface of the battery described in e.g. [43, 49, 77] is not incorporated.

The current collectors are supposed to be inert equipotential regions having homogeneous contact with the active electrode material across the whole area. Thus the contact resistance to the electrodes can be regarded as part of the inner resistance of the battery. Due to these properties the current collectors need not be considered separately in the modeling domain.

It is further assumed that the electrodes and the separator are uniform in their porosity distribution across the area allowing to relate all quantities to the cross-sectional area of the electrodes after [71]. Thus the computational domain can be reduced in the direction of the main reaction x.

According to [34] the electrolyte can be considered to be binary with only the Li^+ cations as the electroactive species. Due to electroneutrality the mass balance for both the anion and the cation must be the same. Thus, for simplicity reasons in [89] mass transport in the electrolyte is derived for the anion applying the *concentrated solution theory* described in [61]. It is further assumed that convection within the battery can be neglected and therefore species transport within the electrolyte is only due to diffusion and migration.

Volume changes of the electrode materials usually can be neglected and there is only little change in the morphology of the active material according to [89]. Therefore, the electrode porosity can be assumed as constant and there is no flow in the electrolyte due to displacement of the liquid phase. Furthermore, mechanical stress during lithium insertion/deinsertion into the active material as proposed in [98] as well as the repair of SEI damage due to intercalation-related stress is not considered.

Since all phases are considered to be electrically neutral, the dimension of the electrochemical double layer is assumed to be small relative to the pore volume according to [89].

Diffusivity of the solid (D_s) and liquid (D_ℓ) phase as well as the transference number t_+^0 are assumed to be constant values with respect to time after [34].

3.1.2. Porosity Modeling

To incorporate the properties of the porous electrodes without going into geometric detail a macroscopic description explained in [61] and [89] is used. Following this approach, instead of dealing with the exact position and shape of the particles and pores respectively, the properties of the electrode material are averaged over a volume small with respect to the overall dimensions but large compared to the pore structure. The particles within the electrodes are treated as spheres of uniform size according to [34].

A schematic representation of a porous electrode consisting of spherical particles is shown in fig. 3.1 (a) together with a detailed view of an infinitesimal electrode fragment of length dx composed of spherical particles of conductivity σ and diffusivity

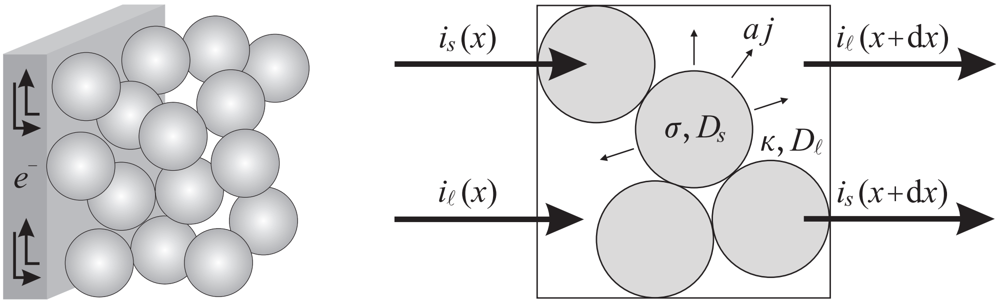

(a) (b)

Figure 3.1.: (a) Schematic representation of an electrode consisting of spherical particles; (b) Detailed view of an infinitesimal electrode fragment of length dx composed of spherical particles(b, based on [58]). Within the volume element current can flow in the solid and the liquid phase with both species interacting at the particle/electrolyte interface.

D_s surrounded by an electrolyte of conductivity κ and diffusivity D_ℓ depicted in fig. 3.1 (b) on the basis of [58]. Within the volume element current can be divided in a solid (i_s) as well as a liquid fraction (i_ℓ). Both species are interacting at the particle/electrolyte interface with aj being the reaction current per volume. The 'active' surface area per volume a where the charge transfer reaction takes place is often calculated by

$$a = \frac{A^{\text{surf}}}{V}\varepsilon_s = \frac{3\varepsilon_s}{r_p} \tag{3.1}$$

with A^{surf} and V being the surface area and the volume of the particles of radius r_p and ε_s being the volume fraction of the solid phase after [77]. Incorporating ε_s into equ. 3.1 is due to the contact between the particles and thus reducing the exchange surface between the solid and the electrolyte.

Since the material parameters of the solid and liquid phase are not directly accessible within the porous electrode often effective material properties based on known parameter values of the homogeneous materials are introduced. In most cases the Bruggeman relationship according to [61] considering porosity as well as tortuosity of the material is applied to obtain effective values for the conductivities of the solid and liquid phase

$$\sigma^{\text{eff}} = \sigma\varepsilon_s^{\text{brug}} \tag{3.2}$$

$$\kappa^{\text{eff}} = \kappa\varepsilon_\ell^{\text{brug}} \tag{3.3}$$

as well as the effective diffusivity of the electrolyte

$$D_\ell^{\text{eff}} = D_\ell\varepsilon_\ell^{\text{brug}} \tag{3.4}$$

with ε_s and ε_ℓ being the volume fraction of the solid and liquid phase and brug being the Bruggeman exponent. In equ. 3.2 to equ. 3.4 the influence of porosity and tortuosity is already summarized to a single correction term $\varepsilon_s^{\text{brug}}$ and $\varepsilon_\ell^{\text{brug}}$ respectively. Thus tortuosity τ_i can be expressed in terms of the volume fraction of the solid ε_s and liquid phase ε_ℓ to

$$\tau_i = \varepsilon_i^{1-\text{brug}} \quad \text{with} \quad i = \{s, \ell\} \tag{3.5}$$

according to [85] where also a summary of parameter values for equ. 3.5 for different porous structures can be found.

3.2. Model Equations

Considering the assumptions given at the beginning of this chapter in this section a system of governing equations for the following state variables is derived:

ϕ_s ... potential in the solid phase
ϕ_ℓ ... potential in the liquid phase
c_s ... concentration in the solid phase
c_ℓ ... concentration in the liquid phase

Therefore, the modeling domain of the lithium-ion battery is divided into three subdomains numbered from left to right as depicted in fig. 3.2 based on [97]. The subdomains $\Omega_1 = (0, L_1)$ and $\Omega_3 = (L - L_3, L)$ are representing the negative and positive electrode and subdomain $\Omega_2 = (L_1, L - L_3)$ the separator in between with $L = L_1 + L_2 + L_3$ being the total length of the whole modeling domain. Because there is no solid material within the separator some equations are only fulfilled for the electrodes. Thus, throughout this chapter the index j is used to define the validity

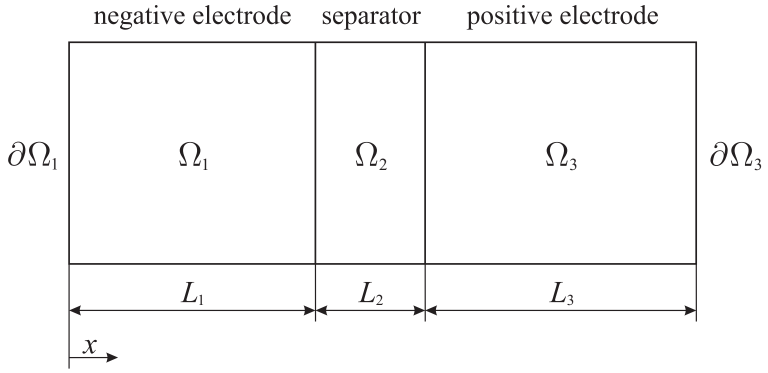

Figure 3.2.: Division of the battery in 3 subdomains Ω_1, Ω_2, Ω_3 representing the negative electrode, the separator, and the positive electrode according to [97].

area of each equation.

3.2.1. Potentials in the solid and liquid phase

Besides the potential distributions in the solid and liquid phase in the following the driving forces of electrons to flow in the matrix and ions to flow in the solution are summarized.

Potential in the solid phase – electric conduction

In the solid material the electrons move in response to an electric field E which is proportional to the negative gradient of the potential $\phi_{s,j}$

$$E = -\frac{\partial \phi_{s,j}}{\partial x}, \quad j = \{1,3\} \ . \tag{3.6}$$

The relation between current density $i_{s,j}$ and the potential gradient is given by Ohm's law

$$i_{s,j} = -\sigma_j^{\mathrm{eff}} \frac{\partial \phi_{s,j}}{\partial x}, \quad j = \{1,3\} \tag{3.7}$$

with σ_i^{eff} being the effective electrical conductivity of the electrodes. From the potential distribution in the solid phase the terminal voltage of the battery can be obtained by

$$u_{\text{cell}} \;=\; \phi_{s,3}|_{\partial\Omega_3} - \phi_{s,1}|_{\partial\Omega_1} - iR_i \tag{3.8}$$

with $\partial\Omega_1$ and $\partial\Omega_3$ being the contact points of the current collectors with the negative and positive electrode and the inner resistance R_i summarizing the ohmic losses of the battery.

Potential in the liquid phase – ionic conduction

In contrast to electron flow in the solid the motion of ions in the electrolyte is not only due to the presence of a potential gradient (migration) but also due to concentration gradients (diffusion) and fluid motion (convection). Thus the current density in the solution $i_{\ell,j}$ can be derived from the electrochemical net flux J_{net}

$$i_{\ell,j} \;=\; F(\underbrace{J_{\text{migration}} + J_{\text{diffusion}} + J_{\text{convection}}}_{\text{net flux } J_{\text{net}}}), \quad j = \{1,2,3\} \tag{3.9}$$

resulting in

$$i_{\ell,j} \;=\; \underbrace{-\kappa_j^{\text{eff}}(c_{\ell,j})\frac{\partial\phi_{\ell,j}}{\partial x}}_{\text{migration}} + \underbrace{\frac{2\kappa_j^{\text{eff}}(c_{\ell,j})RT}{F}\frac{\partial \ln c_{\ell,j}}{\partial x}}_{\text{diffusion}}, \quad j = \{1,2,3\} \tag{3.10}$$

with F being Faraday's constant, $\kappa_j^{\text{eff}}(c_{\ell,j})$ being the effective ionic conductivity of the electrolyte depending on the salt concentration $c_{\ell,j}$ and ϕ_ℓ being the potential of the electrolyte. According to [89] ϕ_ℓ is defined as the measured potential difference of a reversible lithium electrode versus a lithium reference electrode in a half-cell. As stated early in this chapter in equ. 3.10 the influence of convection is neglected.

Presetting the input current via boundary conditions

Assuming a homogeneous current distribution across the electrode surfaces the overall charge/discharge current I can be expressed in terms of the current density i

$$I \;=\; \int\limits_{A_{\text{elec}}} i \mathrm{d}A_{\text{elec}} \;=\; iA_{\text{elec}} \tag{3.11}$$

with A_{elec} being the cross-sectional area of the electrodes. Thus for galvanostatic operation of the battery the current density in the solid phase at the boundaries of the negative and positive electrode being in contact with the current collectors

$$i_{s,1}\big|_{\partial\Omega_1} \;=\; i_{s,3}\big|_{\partial\Omega_3} \;=\; i \tag{3.12}$$

is resulting. Within an electrode the total current density is transformed from an electronic partial current density into an ionic one and accordingly reversely on the counter electrode. Considering the separator as an ideal electric insulator between the electrodes the division of the total current density for all three modeling domains can be summarized

$$i \;=\; \begin{cases} i_{s,j} + i_{\ell,j}, & j = \{1,3\} \\ \;0 \;\;+ i_{\ell,j}, & j = \{2\}\ . \end{cases} \tag{3.13}$$

3.2.2. Conservation of Charge and Charge Transfer

Due to the prerequisite of electroneutrality it is advantageous to consider the conservation of charge compared to the conservation of current densities described in the previous section.

Conservation of Charge

Deriving equ. 3.13 with respect to the spatial coordinate x leads to

$$0 \;=\; \begin{cases} \dfrac{\partial i_{s,j}}{\partial x} + \dfrac{\partial i_{\ell,j}}{\partial x}, & j = \{1,3\} \\ \;\;0 \;\;+ \dfrac{\partial i_{\ell,j}}{\partial x}, & j = \{2\}\ . \end{cases} \tag{3.14}$$

By introducing the reaction current density at the interface j_j into the continuity equation we get a relation between the spatial derivative of the current density and the time derivative of charge in the form

$$\frac{\partial i_{\ell,j}}{\partial x} \;=\; -\frac{\partial \rho_j}{\partial t} \;=\; a_j j_j, \quad j = \{1,3\} \tag{3.15}$$

with ρ being the charge density and a_j the ‘active’ surface area per volume.. After employing equ. 3.7 and equ. 3.10 into equ. 3.14 and using the relation given in equ. 3.15 for the spatial derivative of $i_{\ell,j}$ one obtains the charge balance in the solid

$$-\,a_j j_j \;=\; -\frac{\partial}{\partial x}\left(\sigma_j^{\text{eff}}\frac{\partial \phi_{s,j}}{\partial x}\right), \quad j = \{1,3\} \tag{3.16}$$

and liquid phase

$$-\frac{\partial}{\partial x}\left(\kappa_j^{\mathrm{eff}}(c_{\ell,j})\frac{\partial\phi_{\ell,j}}{\partial x}-\frac{2\kappa_j^{\mathrm{eff}}(c_{\ell,j})RT}{F}\frac{\partial \ln c_{\ell,j}}{\partial x}\right) \;=\; \begin{cases} a_j j_j, & j=\{1,3\} \\ 0\;, & j=\{2\}\;. \end{cases} \tag{3.17}$$

To ensure that no additional charge is produced or consumed within the electrode domains the total current density can be expressed by the reaction current using an integral formulation of equ. 3.15

$$a_1\int\limits_{\Omega_1} j_1 \mathrm{d}x \;=\; -a_3\int\limits_{\Omega_3} j_3 \mathrm{d}x \;=\; i \tag{3.18}$$

considering the boundary conditions for the current densities given in the previous section.

Charge Transfer

The faradaic reaction current density $j_{j,f}$ determining the charge transfer reaction is usually described by the Butler-Volmer equation

$$j_{j,f} \;=\; i_{0,j}\left[e^{\alpha f\eta}-e^{-(1-\alpha)f\eta}\right],\quad j=\{1,3\}\;. \tag{3.19}$$

Thereby, according to [89], the surface overpotential η represents the deviation of the thermodynamic potential difference between the solid $\phi_{s,j}$ and liquid phase $\phi_{\ell,j}$

$$\eta \;=\; \phi_{s,j}-\phi_{\ell,j}-U_j^0(c_{s,j}^{\mathrm{surf}}),\quad j=\{1,3\} \tag{3.20}$$

with $U_j^0(c_{s,j}^{\mathrm{surf}})$ being the open circuit voltage depending on the local lithium concentration in the solid. According to [89] the concentration dependency of the exchange current density for an insertion electrode is often expressed by

$$i_{0,j} \;=\; Fk_j\left(c_{s,j}^{\max}-c_{s,j}^{\mathrm{surf}}\right)^{1-\alpha}\left(c_{s,j}^{\mathrm{surf}}\right)^{\alpha}\left(c_{\ell,i}\right)^{\alpha},\quad j=\{1,3\}\;. \tag{3.21}$$

with c_s being the concentration of the solid and c_ℓ the concentration of the liquid respectively and F being Faraday's constant. Instead of splitting up in a forward and backward part here the reaction rate is summarized in a single parameter k_j. As depicted in fig. 3.3 the exchange current density tends to zero for the concentration in the solid approaching either $c_s^{\max}$ or 0 resulting in high overpotentials η. The location of the maximum between these two extrema depends on the transfer coefficient α

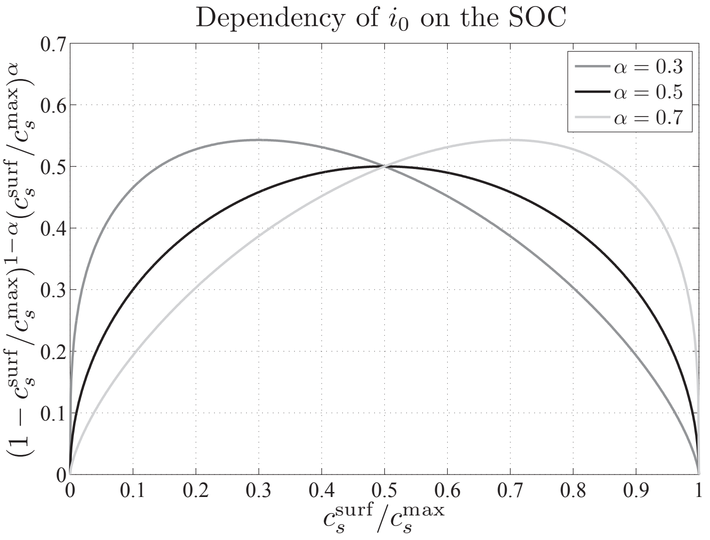

Figure 3.3.: Dependency of the exchange current density i_0 on the normalized surface concentration of the particle $c_s^{\mathrm{surf}}/c_s^{\mathrm{max}}$ being a measure for the local SOC.

which is usually set to 0.5. Thus, the behavior of i_0 is symmetric to the normalized amount of lithium at the surface of the particles $c_s^{\mathrm{surf}}/c_s^{\mathrm{max}}$ which can be regarded as a measure for the local state of charge. In the following it has been decided with experts in the 'Comet K2 project: *Modellierung, Validierung und Test von Lithium-Ionen-Batterien für Hybridfahrzeuge*' to use a more general approach for the charge transfer reaction of a redox system based on [6]

$$j_{j,f} \quad = \quad i_{0,j}\left[\left(\frac{c_{\ell,j}}{c_{\ell,j}^0}\right)e^{\alpha f\eta} - w\left(\frac{c_{s,j}^{\mathrm{surf}} - c_{s,j}^{\mathrm{min}}}{c_{s,j}^{\mathrm{ave}}}\right)e^{-(1-\alpha)f\eta}\right], \quad j = \{1,3\} \tag{3.22}$$

with the exchange current density

$$i_{0,j} \quad = \quad Fk_j\left(\frac{c_{s,j}^{\mathrm{surf}} - c_{s,j}^{\mathrm{min}}}{c_{s,j}^{\mathrm{max}}}\right)^{1-\alpha}\left(\frac{c_{\ell,j}}{c_{\ell,j}^0}\right)^{\alpha}, \quad j = \{1,3\}\ . \tag{3.23}$$

Hence, deviations from equilibrium are considered by the fraction from the local concentration to the bulk concentration for the solid and liquid phase. The additional parameter c_s^{min} is used to incorporate the amount of inactive lithium of the electrodes not participating in the reaction and w denotes an additional weighting factor between the forward and backward reaction.

Extension of the Charge Transfer Equation with the Electrochemical Double Layer

In addition to the faradaic fraction of the charge transfer reaction represented by the Butler-Volmer equation the influence of the interface between the electrode and the electrolyte forming an electrochemical double layer described in section 2.3.2 has to be considered. As already mentioned the relation between the double layer reaction current density $j_{j,\mathrm{dl}}$ and the potential difference at the interface $(\phi_{s,j} - \phi_{\ell,j})$ is given by

$$j_{j,\mathrm{dl}} = C_{\mathrm{dl},j} \frac{\partial(\phi_{s,j} - \phi_{\ell,j})}{\partial t}, \quad j = \{1, 3\} \tag{3.24}$$

with C_{dl} being the double layer capacitance which can be calculated by applying the Gouy-Chapman theory explained in [6]. Following this approach the total charge on the interface $Q_{\mathrm{dl,j}}$ can be calculated using Gauss's law

$$Q_{\mathrm{dl},j} = \oint \varepsilon E \mathrm{d}A = \varepsilon A_{\mathrm{elec}} \frac{\partial(\phi_{s,j} - \phi_{\ell,j})}{\partial x}\Big|_{\mathrm{surf}} \tag{3.25}$$

with A_{elec} being the electrode cross-sectional area, E the electric field strength, and ε the permittivity of the electrode material. The double layer capacitance $C_{\mathrm{dl,j}}$ results from the deviation of the charge density $(Q_{\mathrm{dl,j}}/A_{\mathrm{elec}})$ with respect to the difference of the potential in the solid $\phi_{s,j}$ and liquid phase $\phi_{\ell,j}$ evaluated at the electrode surface denoted by the subscript surf

$$C_{\mathrm{dl},j} = \frac{\partial(Q_{\mathrm{dl},j}/A_{\mathrm{elec}})}{\partial(\phi_{s,j} - \phi_{\ell,j})|_{\mathrm{surf}}} = \sqrt{2c_0\varepsilon f F} \cosh\left(\frac{f(\phi_{s,j} - \phi_{\ell,j})|_{\mathrm{surf}}}{2}\right) . \tag{3.26}$$

Thus, considering the double layer capacity $C_{\mathrm{dl,j}}$, the overall reaction current density j_j can be calculated by superposition of the faradaic $j_{j,f}$ and the double layer partial current density $j_{j,\mathrm{dl}}$

$$j_j = j_{j,f} + j_{j,\mathrm{dl}}, \quad j = \{1, 3\} . \tag{3.27}$$

In [62] the influence of the electrochemical double layer on the positive and negative half cell reactions is analyzed using pulse excitation in the ms range. A more detailed description on modeling the electrochemical double layer can be found in [89] and [73].

3.2.3. Diffusion Processes

To incorporate the influence of differences in concentration on the terminal voltage u_{cell} as well as the concentration dependency of several parameters such as the exchange current density $i_{0,j}$ in this section the diffusion equations for the solid and liquid phase are derived.

Concentration in the liquid phase

Neglecting side reactions mass transport in the electrolyte for a porous material can be deduced from the spatial derivative of the electrochemical flux $J_{\ell,j}$

$$\varepsilon_{\ell,j}\frac{\partial c_{\ell,j}}{\partial t} = -\frac{\partial J_{\ell,j}}{\partial x}, \quad j=\{1,2,3\} \tag{3.28}$$

with $c_{\ell,j}$ being the lithium concentration in the liquid and ε_ℓ being the volume fraction of the void. Considering the *concentrated solution theory* and neglecting structural changes of the electrode according to [89] one obtains

$$\varepsilon_{\ell,j}\frac{\partial c_{\ell,j}}{\partial t} = \begin{cases} \dfrac{\partial}{\partial x}\left(D_{\ell,j}^{\text{eff}}\dfrac{\partial c_{\ell,j}}{\partial x}\right) + \dfrac{1-t_+^0}{F}a_j j_j, & j=\{1,3\} \\ \dfrac{\partial}{\partial x}\left(D_{\ell,j}^{\text{eff}}\dfrac{\partial c_{\ell,j}}{\partial x}\right) & , \quad j=\{2\} \end{cases} \tag{3.29}$$

with a_j being the ‘active’ surface area per volume, $D_{\ell,j}^{\text{eff}}$ the effective diffusivity of the electrolyte, F Faraday’s constant and t_+^0 the transition number. Because there is no transport of lithium into the current collectors there is no electrochemical flux on the outer boundaries

$$D_{\ell,1}^{\text{eff}}\frac{\partial c_{\ell,1}}{\partial x}\bigg|_{\partial\Omega_1} = D_{\ell,3}^{\text{eff}}\frac{\partial c_{\ell,3}}{\partial x}\bigg|_{\partial\Omega_3} = 0 \tag{3.30}$$

whereas on the interface to the separator the electrochemical flux $J_{\ell,j}$ has to be preserved

$$-D_{\ell,1}^{\text{eff}}\frac{\partial c_{\ell,1}}{\partial x}\bigg|_{\partial\Omega_{12}} = -D_{\ell,2}^{\text{eff}}\frac{\partial c_{\ell,2}}{\partial x}\bigg|_{\partial\Omega_{12}}, \quad -D_{\ell,2}^{\text{eff}}\frac{\partial c_{\ell,2}}{\partial x}\bigg|_{\partial\Omega_{23}} = -D_{\ell,3}^{\text{eff}}\frac{\partial c_{\ell,3}}{\partial x}\bigg|_{\partial\Omega_{23}} \tag{3.31}$$

Furthermore, as initial condition the concentration $c_\ell(0,x)$ is assumed to be constant in all three modeling domains

$$c_\ell(0,x) = c_\ell^0, \quad j=\{1,2,3\} \tag{3.32}$$

representing the resting state of the battery.

Concentration in the solid phase

In the solid phase transport of lithium is modeled by particle diffusion. For a single particle of radius $r_{p,j}$ of the electrode the diffusion equation can be written in spherical coordinates

$$\frac{\partial c_{s,j}}{\partial t} = \frac{1}{r_j^2}\frac{\partial}{\partial x}\left(D_{s,j} r_j^2 \frac{\partial c_{s,j}}{\partial x}\right), \quad j = \{1,3\}\ . \tag{3.33}$$

assuming isotropic diffusion across the particle surface with $c_{s,j}$ being the lithium concentration and $D_{s,j}$ the diffusivity of the solid and r the spatial coordinate in radial direction. The electrochemical flux (j_j/F) is incorporated via the boundary conditions depending on the position of the particle within the electrode

$$-D_{s,j}\left.\frac{\partial c_{s,j}}{\partial r}\right|_{r_j=0} = 0 \quad \text{and} \quad -D_{s,j}\left.\frac{\partial c_{s,j}}{\partial r}\right|_{r_j=r_{p,j}} = \frac{j_j}{F}, \quad j = \{1,3\}\ . \tag{3.34}$$

Same as for diffusion in the electrolyte the initial concentration for diffusion in the particles $c_{s,j}(0, r_j)$ is assumed to be constant

$$c_{s,j}(0, r_j) = c_{s,j}^0, \quad j = \{1,3\}\ . \tag{3.35}$$

At this point it has to be mentioned that this approach only includes diffusion in radial direction whereas diffusion between neighboring particles is neglected. Nevertheless according to [89] the error resulting from this simplification is negligible.

4. Numerical Realization

This chapter deals with solving the set of governing equations introduced in the previous chapter. Although there exist some analytical approaches especially for the lithium insertion process in the electrodes as is discussed in [57, 40, 92] in this work only numerical solution techniques are considered. This is due to the complex coupling of the governing equations via the charge transfer equation. Thus, resulting in a nonlinear set of equations. For a better understanding of the solution strategies presented later on a short introduction on the used numerical methods is given at the beginning of this chapter. After a detailed description of the numerical realization the chapter concludes with some improvements made on the implementation to enhance the overall model performance.

4.1. Numerical Methods

In the following the principles of the Finite Difference Method (FDM), the Finite Element Method (FEM) and the Control Volume (CVM) or Finite Volume Method (FVM) are summarized briefly. Additionally, the strengths and limitations of each method are evaluated referring to [44] and [60]. Hence, the most appropriate method to solve the set of governing equations is selected.

4.1.1. The Finite Difference Method

The idea of the FDM is to approximate the derivatives in a differential equation with finite differences. Thus, according to [55] the derivative of a function $u(x)$ at a particular point x_n can be approximated by its neighboring points using a one-sided approximation

$$D_+u(x_n) \equiv \frac{u(x_n+h)-u(x_n)}{h} \quad , \quad D_-u(x_n) \equiv \frac{u(x_n)-u(x_n-h)}{h} \tag{4.1}$$

with D_+u and D_-u being the difference quotients from the left and right, respectively. Both expressions in equ. 4.1 give a first order accurate approximation to the derivative

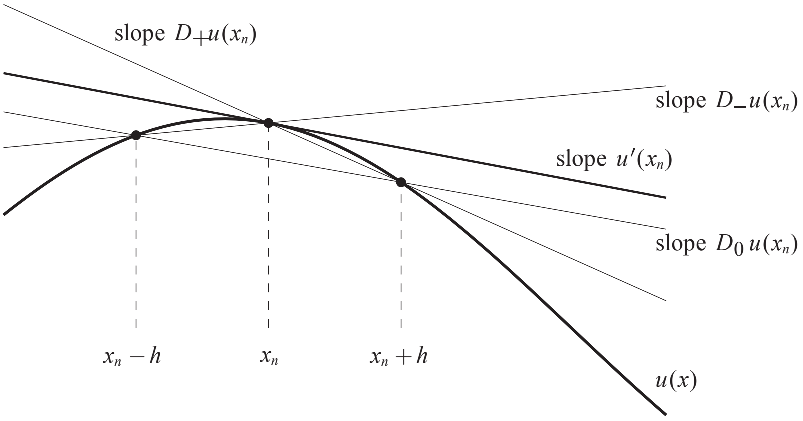

Figure 4.1.: Approximation of the derivative of $u(x)$ using one-sided approximations D_+u and D_-u as well as a centered approximation D_0u (modified from [55]).

of $u(x)$ with the error being proportional to h. Alternatively, the average of the one-side approximations D_+u and D_-u resulting in the centered approximation

$$D_0u(x_n) \quad \equiv \quad \frac{u(x_n+h)-u(x_n-h)}{2h} \quad = \quad \frac{1}{2}\left(D_+u(x_n)+D_-u(x_n)\right) \tag{4.2}$$

can be used. Thus, resulting in a second order accurate approximation with the error being proportional to h^2 instead of h as for the first order accurate approximation leading to a much smaller error for small values of h. In fig. 4.1 the slopes of the single approximations and the exact derivative at x_n are shown together with the the function $u(x)$.

Finally, the advantages and disadvantages of the FDM are summarized with respect to the applicability for solving the battery equations. Due to the simple geometry of the model the restrictions with respect to the geometry of the domain are neglected.

Advantages of the FDM

- well described in literature
- transparent method allowing straightforward implementation
- use of higher order approximations to derivatives possible
- well suited for rectangular domains (such as battery geometry)

Disadvantages of the FDM

- special treatment of Neumann- or mixed boundary conditions
- difficulties in handling problems with unsteady coefficients
- for non-rectangular domains the FDM tends to cause problems

4.1.2. The Finite Element Method

In contrast to the difference schemes the basis of the FEM is not the classical formulation but the so-called weak or variational formulation of the (partial) differential equation. According to [44] the variational formulation for the Poisson equation

$$\begin{aligned} \Delta u(x) &= f(x) \quad \text{in} \quad \Omega \\ -u(x) &= 0 \quad \text{on} \quad \partial\Omega \end{aligned} \tag{4.3}$$

can be derived by multiplying the differential equation equ. 4.3 with a basis function $v(x)$ and subsequent integration over the domain Ω. Applying integration by parts using the divergence theorem and integration of the boundary condition one obtains

$$\begin{aligned} \int\limits_{\Omega} f(x)v(x)\mathrm{d}x &= \int\limits_{\Omega} \nabla u(x)\cdot\nabla v(x)\mathrm{d}x - \underbrace{\int\limits_{\partial\Omega} \nabla u(x)\cdot\nu(x)v(x)\mathrm{d}x}_{=0} \\ &= \int\limits_{\Omega} \nabla u(x)\cdot\nabla v(x)\mathrm{d}x \end{aligned} \tag{4.4}$$

with the test function $v(x)$ being zero at $\partial\Omega$ and $\nu(x)$ being the outward unit surface normal to $\partial\Omega$. To get an approximate solution u_h to the variational problem the Galerkin approach

$$u_h(x) = \sum_{n=0}^{N} u_n p_n(x) \tag{4.5}$$

is used. Thus, according to [41] a linear combination of finite functions p_n being different from zero only in a ‘small’ subdomain is searched. The unknown node parameters u_n representing the approximate solution of $u(x_n)$ are determined by the solution of a linear equation system. Generally $u_h(x_n) = u(x_n)$ does not hold as can be seen in fig. 4.2 showing the exact solution u together with the approximate

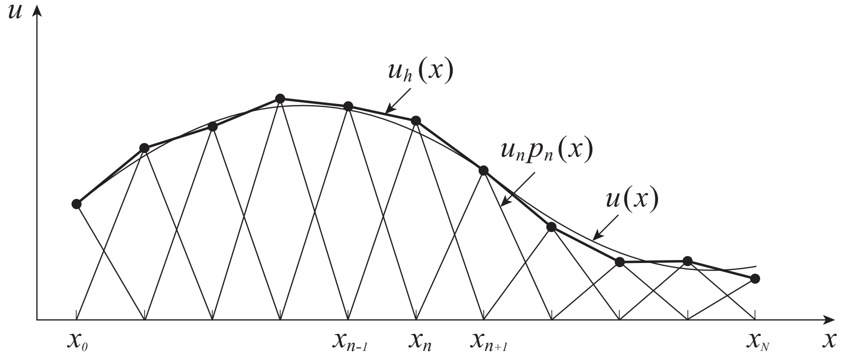

Figure 4.2.: Exact solution $u(x)$ and approximate solution $u_h(x)$ by a linear combination of finite functions p_n and node parameters u_n.

solution u_h. In contrast to the early described FDM where a vector consisting of the approximate solution of u at x_n is obtained for the FEM one obtains functions u_h and vectors containing the coefficients u_n of the Galerkin approach.

Same as for the FDM the advantages and disadvantages of the FEM with respect to the battery equations are summarized. Further, due to its wide application area there exist a lot of commercial software packages for the numerical solution of PDEs based on the FEM.

Advantages of the FEM

- wide application area
- use of higher order basis functions possible
- simple discretization of boundary conditions (especially the treatment of Neumann- or mixed boundary conditions)

Disadvantages of the FEM

- computation of the elements of the stiffness matrix and the entries of the load vector has to be carried out by numerical integration mostly (accuracy is depending on the amount of supporting points)

4.1.3. The Control Volume or Finite Volume Method

Although the CVM contains ideas of both the difference scheme as well as the finite element method it can be regarded as an independent discretization method.

Nevertheless, due to its affinity to the aforementioned methods the CVM is often interpreted as a ‘generalized difference scheme’ or an alternate formulation of the FEM. The main field of application of the CVM lies in the numerical approximation of hyperbolic continuity equations of the form

$$\frac{\partial u}{\partial t} + \nabla f(u) \quad = \quad s \tag{4.6}$$

with u being the accumulated quantity and f describing the flux. The generation term s in equ. 4.6 becomes 0 for conserved quantities that cannot be generated or destroyed. The basis of the CVM is the division of the modeling domain in N non-overlapping so-called control volumes (CVs) with the node points being located either in the center of the CV (cell-centered) or at the edges of the CV (cell-vertex) and building the integral over each control volume. After applying the divergence theorem one obtains

$$\frac{\partial}{\partial t}\int\limits_{\Omega_n} u\mathrm{d}x \quad = \quad -\int\limits_{\partial\Omega_n} \nu \cdot f(u)\mathrm{d}\sigma + \int\limits_{\Omega_n} s\mathrm{d}x \tag{4.7}$$

with ν being the outward normal to $\partial\Omega_n$. Within the control volumes the solution variables can either be treated as constant or linear in the case that the spatial derivative of the function is considered. In fig. 4.3 both situations are depicted for the one-dimensional case. Regarding the battery equations the ability of conservation of certain principles allowing among other things the successful handling of unsteady coefficients as is the case on the interfaces between the electrodes and the separator

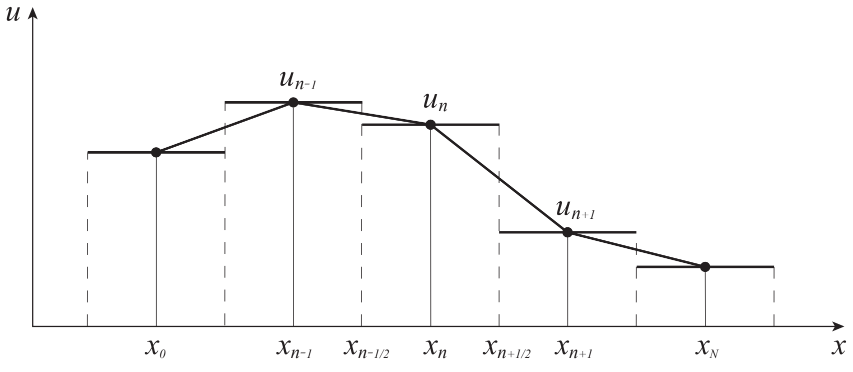

Figure 4.3.: Approximation of the solution variable u for the CVM by a constant or linear profile within the control volumes.

are the main benefits of the CVM. See also [67] where the CVM is used to describe nonlinear diffusion in lithium-ion batteries. After [44] the advantages and disadvantages of the method can be summarized as follows.

Advantages of the CVM

- simple assembling
- conservation of certain principles of the continuous problem (e.g. conservation laws, maximum principles). This allows amongst other things the successful handling of equations with unsteady coefficients as well as diffusion-convection-equations
- simple linearizeability of nonlinear problems (simpler than Finite-Element-Methods (Newton method))
- simple discretization of boundary conditions (same as Finite-Element-Methods, especially the treatment of Neumann- or mixed boundary conditions)

Disadvantages of the CVM

- smaller application area than Finite-Element-Method or Difference schemes
- problems with constructing methods of higher order (no so-called *p*-version as for the Finite-Element-Method existent)
- difficult mathematical analysis (stability, convergence,...)

4.2. Implementation of the Battery Model

In a first attempt the applicability of the lithium-ion battery model included in the batteries and fuel cells module of the commercial FEM simulation software COMSOL Multiphysics® [23] for the lithium iron phosphate battery used in this thesis has been investigated. Thus, material properties of the electrolyte and the active materials as well as geometric parameters such as electrode dimensions or particle size have been adapted. In fig. 4.4 the simulation result at C-rates from 0.5 C to 2 C are summarized. In contrast to the measurement the simulation shows a great difference between the charge and discharge behavior. Also the relaxation behavior at the end of the simulation when the current is turned off can not be reproduced accurately. Besides that a ‘complete’ charge/discharge of the battery is not possible because

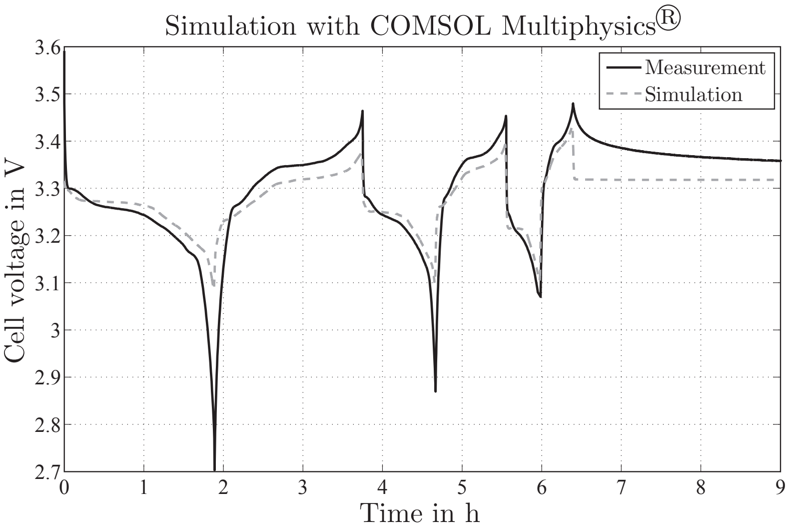

Figure 4.4.: Comparison between measured (solid) and simulated (dashed) cell voltage using the multiphysics software package COMSOL Multiphysics®.

the simulation stops before the cut-off voltage in the measurement is reached. This is due to concentration gradients in the solid phase as well as possible problems with the OCV values used in the extreme regions. Therefore, if the concentration at the particle surface at any position within the electrode reaches its minimum or maximum value the simulation is aborted. Due to the limited access into the solver architecture as well as the difficult implementation of a reliable exception handling for such 'undefined' states in the following the development of a numerical solver for the battery equations is derived. The focus of the implementation lies in obtaining a robust and accurate battery model which is able to cover a wide application area including a proper representation of the dynamical as well as the long term current-voltage behavior of the battery.

4.2.1. Presumptions for the implementation of the model

Before coming into detail on the implementation at first the simplifications and modifications performed on the set of equations as well as assumptions made on the state variables are summarized briefly.

Since only the boundary flux is known for the potential equations in the solid and liquid phase a reference potential has to be introduced to obtain unique solutions. Therefore, the potential in the solid phase is set to zero at the outer boundary of the negative electrode

$$\phi_{s,1}\big|_{\partial\Omega_1} \quad = \quad 0 \ . \tag{4.8}$$

Additionally, to simplify Ohm's law in the liquid phase a change of variables on the electrolyte potential of the form

$$\tilde{\phi}_\ell \leftarrow \phi_\ell - \frac{2}{f}\mathrm{ln}c_\ell \tag{4.9}$$

is used according to [97]. Thus equ. 3.17 can be brought into the same shape as the potential in the solid phase represented by equ. 3.16

$$-\frac{\partial}{\partial x}\left(\kappa_j^{\mathrm{eff}}(c_{\ell,j})\frac{\partial\tilde{\phi}_{\ell,j}}{\partial x}\right) \quad = \quad \begin{cases} a_j j_j, & j=\{1,3\} \\ \ \ 0\ \ , & j=\{2\}\ . \end{cases} \tag{4.10}$$

This change of variables of the liquid potential has to be considered in the calculation of the reaction current density j_j as well where the original potential $\phi_{\ell,j}$ is required. Thus, the surface overpotential in the Butler-Volmer equation represented by equ. 3.20 has to be modified to

$$\eta \quad = \quad \phi_{s,j} - \left(\tilde{\phi}_{\ell,j} + \frac{2}{f}\mathrm{ln}c_{\ell,j}\right) - U_j^0(c_{s,j}^{\mathrm{surf}}), \quad j=\{1,3\}\ . \tag{4.11}$$

Additionally, the double layer fraction of the reaction current density represented by equ. 3.24 has to be modified to

$$j_{j,\mathrm{dl}} \quad = \quad C_{\mathrm{dl},j}\frac{\partial\left(\phi_{s,j} - \left(\tilde{\phi}_{\ell,j} + \frac{2}{f}\mathrm{ln}c_{\ell,j}\right)\right)}{\partial t}, \quad j=\{1,3\} \tag{4.12}$$

incorporating the transformed potential $\tilde{\phi}_{\ell,j}$. Therefore the set of equations to be solved is complete.

Further, it is assumed that the concentrations are changing at a much lower rate than the potentials, especially if the load current is changed. Hence, for the calculation of the reaction current in the actual time step the concentrations of the previous time step can be used. Therefore, the overall cell voltage can be calculated without iterating the solution at each time step and thus reducing the calculation effort as well as the simulation time. In fig. 4.5 the division of the battery in finite volume elements so called control volumes (CVs) is shown with a spherical particle located in

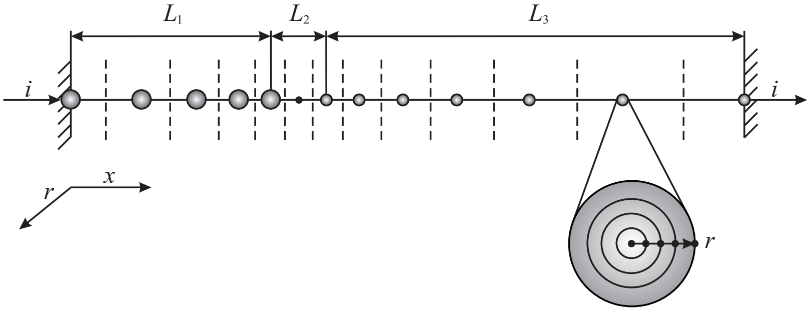

Figure 4.5.: Division of the battery in so called control volumes. In the electrode regions a spherical particles is introduced in each control volume to incorporate lithium diffusion in the solid phase resulting in a pseudo 2D representation of the battery (from [79]).

each CV of the electrodes resulting in a pseudo 2D representation of the battery. The discretization in x-direction was chosen such that the electrodes and the separator are sharing a discretization point at the interfaces allowing a simple treatment of the different material properties across the interface. Thus, each domain can be dealt with separately.

For simplicity reasons throughout the rest of this chapter the implementation is explained on the example of the negative electrode. Thus, the index indicating the number of the domain is omitted.

4.2.2. Discretization in Space and Time

Based on the information on numerical schemes at the beginning of this chapter the CVM is considered to be the most suitable method for solving the set of governing equations describing the lithium-ion battery. In the following the discretization scheme is explained on the example of the diffusion equation in the liquid phase. Same as in [71] for the lead-acid battery the development of the discretized system is strongly related to the CVM approach given in [64].

Spatial Discretization

In a first step the concentration equation is brought in an integral form by integrating over the modeling domain and reformulating the resulting equation using the divergence theorem. Applying the control volume method the integral is approximated by dividing the modeling domain in a finite number of non-overlapping control volumes and integrating over each control volume separately. For a single control volume the integral can be written in the form

$$\int_{w}^{e} \varepsilon_\ell \frac{\partial c_\ell}{\partial t} \mathrm{d}x = \int_{w}^{e} \frac{\partial}{\partial x}\left(D_\ell^{\mathrm{eff}} \frac{\partial c_\ell}{\partial x}\right) \mathrm{d}x + \frac{1-t_+^0}{F} a \int_{w}^{e} j \mathrm{d}x \tag{4.13}$$

with the lower case letters w and e denoting the interfaces to the neighboring control volumes. After dissolution of the integrals one obtains

$$\varepsilon_\ell \frac{\partial c_\ell}{\partial t} \Delta x = \left(D_\ell^{\mathrm{eff}} \frac{\partial c_\ell}{\partial x}\right)_e - \left(D_\ell^{\mathrm{eff}} \frac{\partial c_\ell}{\partial x}\right)_w + \frac{1-t_+^0}{F} a \bar{j} \Delta x \tag{4.14}$$

with the integral in the source term being approximated by the product of the average value of the reaction current density $\bar{j}$ and Δx the distance between the interfaces. The remaining differentials in equ. 4.14 are approximated using piecewise linear shape functions for interpolating the solution variable within the control volume. Thus, resulting in

$$\varepsilon_\ell \frac{\partial c_{\ell,P}}{\partial t} = \frac{1}{\Delta x}\left[\left(\frac{D_{\ell,e}^{\mathrm{eff}}(c_{\ell,E} - c_{\ell,P})}{(\delta x)_e}\right) - \left(\frac{D_{\ell,w}^{\mathrm{eff}}(c_{\ell,P} - c_{\ell,W})}{(\delta x)_w}\right)\right] + \frac{1-t_+^0}{F} a \bar{j} \tag{4.15}$$

for a control volume around a discretization point P and its neighboring points indicated by the upper case letters W and E as well as the distances between the grid points $(\delta x)_w$ and $(\delta x)_e$ across the interfaces denoted by the lower case letters w and e.

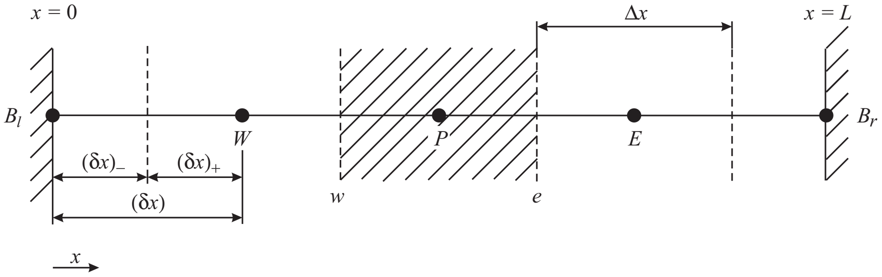

Figure 4.6.: Spatial discretization of the diffusion equation for a CV around a point P neighbored by the points W and E and interfaces between the grid points w and e as well as Δx being the distance between the interfaces indicated by the lower case letters w and e and δx the distance between the grid points indicated by the upper case letters W and E. To be able to calculate the concentration on the boundaries directly so-called ‘half’ control volumes are introduced at $x = 0$ and $x = L$ (modified from [64]).

In fig. 4.6 the spatial discretization is shown graphically for internal and boundary points. At the domain boundaries so-called ‘half’ control volumes are introduced to be able to calculate the solution at the boundary points directly. Furthermore, allowing a simple integration of the electrochemical flux across the boundary. For the 1D diffusion equation setting up the overall system results in a set of ordinary differential equations (ODEs) with a sparse system matrix of tridiagonal shape.

Interface Properties

Because in equ. 4.15 the diffusivity between the control volumes is required the interface diffusivity has to be calculated given only the values at the grid points. Using the arithmetic mean can lead to rather incorrect implications in some cases and can not deal with abrupt changes of material properties or even one control volume having a diffusivity of 0. Therefore the approach proposed in [64] is used instead to calculate the interface diffusivity

$$D_{\ell,n,n+1} = \left(\frac{1-\zeta}{D_{\ell,n}} + \frac{\zeta}{D_{\ell,n+1}}\right)^{-1} \tag{4.16}$$

with the interpolation factor being defined as

$$\zeta \equiv \frac{(\delta x)_+}{(\delta x)} . \tag{4.17}$$

For the discretization used, with the interfaces being midway between the grid points, $\zeta = 0.5$ equ. 4.16 becomes equivalent to the harmonic mean.

Time Discretization

In the next step the remaining time derivative in equ. 4.15 has to be approximated numerically. Therefore, to obtain the net flux generated within a control volume in a certain interval of time equ. 4.15 is integrated in the time interval from t to $t + \Delta t$ resulting in

$$\begin{aligned}\varepsilon_\ell \int\limits_t^{t+\Delta t} \frac{\partial c_{\ell,P}}{\partial t}\mathrm{d}t &= \frac{1}{\Delta x} \int\limits_t^{t+\Delta t} \left(\frac{D^{\mathrm{eff}}_{\ell,e}(c_{\ell,E} - c_{\ell,P})}{(\delta x)_e}\right) - \left(\frac{D^{\mathrm{eff}}_{\ell,\mathrm{w}}(c_{\ell,P} - c_{\ell,W})}{(\delta x)_\mathrm{w}}\right)\mathrm{d}t \\ &\quad + \frac{1-t^0_+}{F} a \int\limits_t^{t+\Delta t} \bar{j}\mathrm{d}t\end{aligned} \tag{4.18}$$

for the investigated control volume around the discretization point P. According to [64] the integrals on the right hand side of equ. 4.15 for $c_{\ell,P}$, $c_{\ell,E}$, and $c_{\ell,W}$ can be expressed by a linear combination of the concentrations at time t and $t + \Delta t$

$$\int_{t}^{t+\Delta t} c_{\ell,P} \mathrm{d}t = \left(\beta c_{\ell,P}^{m+1} + (1-\beta) c_{\ell,P}^{m}\right) \tag{4.19}$$

with β being a weighting factor ranging from 0 to 1. After introducing equ. 4.19 into equ. 4.15 one obtains the following expression

$$\begin{aligned} \varepsilon_\ell \frac{c_{\ell,P}^{m+1} - c_{\ell,P}^{m}}{\Delta t} &= \frac{\beta_1}{\Delta x} \left[\left(\frac{D_{\ell,e}^{\text{eff}} (c_{\ell,E}^{m+1} - c_{\ell,P}^{m+1})}{(\delta x)_e} \right) - \left(\frac{D_{\ell,\mathrm{w}}^{\text{eff}} (c_{\ell,P}^{m+1} - c_{\ell,W}^{m+1})}{(\delta x)_\mathrm{w}} \right) \right] \\ &+ \frac{(1-\beta_1)}{\Delta x} \left[\left(\frac{D_{\ell,e}^{\text{eff}} (c_{\ell,E}^{m} - c_{\ell,P}^{m})}{(\delta x)_e} \right) - \left(\frac{D_{\ell,\mathrm{w}}^{\text{eff}} (c_{\ell,P}^{m} - c_{\ell,W}^{m})}{(\delta x)_\mathrm{w}} \right) \right] \\ &+ \beta_2 \frac{1 - t_+^0}{F} a \bar{j}^{m+1} + (1-\beta_2) \frac{1 - t_+^0}{F} a \bar{j}^{m} . \end{aligned} \tag{4.20}$$

using different values of the weighting factor for the state variable and the source term. For the choice of the weighting factor β the following three standard cases known from literature can be distinguished.

- Explicit ($\beta = 0$)
- Semi implicit ($0 < \beta < 1$; e.g. Crank-Nicolson with $\beta = 0.5$)
- Fully Implicit ($\beta = 1$)

Due to the dependency of the source term on the state variables throughout the thesis a mixture of fully implicit scheme for the state variables and explicit scheme for the source term is used. Consequently, for the choice of the step sizes the Courant-Friedrichs-Lewy condition given in [60]

$$|D_\ell| \frac{\Delta t}{\Delta x} < 1 \tag{4.21}$$

has to be fulfilled for the resulting semi-implicit scheme to obtain physically realistic results. Setting up the overall system one obtains the desired linear set of equations for the 1D diffusion equation evolving from timestep m to $m+1$

$$\begin{pmatrix} a_{P,1} & -a_{E,1} & 0 & \cdots & 0 \\ -a_{W,2} & a_{P,2} & -a_{E,2} & \ddots & \vdots \\ 0 & \ddots & \ddots & \ddots & 0 \\ 0 & \ddots & -\,a_{E,N-1} & a_{P,N-1} & -a_{E,N-1} \\ 0 & \cdots & 0 & -a_{W,N} & a_{P,N} \end{pmatrix} \begin{pmatrix} c_{\ell,1}^{m+1} \\ c_{\ell,2}^{m+1} \\ \vdots \\ c_{\ell,N-1}^{m+1} \\ c_{\ell,N}^{m+1} \end{pmatrix} = \begin{pmatrix} b_1 \\ b_2 \\ \vdots \\ b_{N-1} \\ b_N \end{pmatrix} \tag{4.22}$$

with the coefficients of the system matrix

$$a_{E,n} \;=\; \frac{D_{\ell,e_n}^{\text{eff}}}{(\delta x)_{e_n}}, \quad a_{W,n} \;=\; \frac{D_{\ell,\mathrm{w}_n}^{\text{eff}}}{(\delta x)_{\mathrm{w}_n}}, \quad a_{P,n} \;=\; a_{E,n} + a_{W,n} + \varepsilon_\ell \frac{\Delta x_n}{\Delta t} \tag{4.23}$$

and the source term vector

$$b_n \;=\; \frac{1-t_+^0}{F} a \bar{j}_n^m \Delta x_n + \varepsilon_\ell \frac{\Delta x_n}{\Delta t} c_{\ell,n}^m \;. \tag{4.24}$$

Since only the main diagonal is affected by the discretization in time the tridiagonal shape of the system matrix from the set of ODEs is being preserved.

4.3. Solution Strategies

Due to the complex coupling of the potential equations in the solid and liquid phase in the electrodes via the reaction current density j the resulting discrete equivalent system of equations is of implicit structure. Thus an iterative solution strategy based on the Newton scheme to solve these equations is developed. For the remaining diffusion equations in the solid and liquid phase as well as the liquid potential in the separator region a standard tridiagonal matrix algorithm is implemented. In the following the basic concepts of both solution strategies are summarized briefly.

4.3.1. Tridiagonal Matrix Algorithm

The linear system of equations with a tridiagonal system matrix as obtained for the 1D diffusion equation can be solved efficiently with respect to calculation effort and memory requirement using the so-called tridiagonal matrix algorithm (TDMA) based on the Gaussian elimination principle. Therefore, as stated in [41] the system of equations 4.22 can be brought from tridiagonal into triangular shape as a result of the forward elimination

$$\begin{pmatrix} 1 & -\alpha_2 & 0 & \cdots & 0 \\ 0 & 1 & -\alpha_3 & \ddots & \vdots \\ 0 & \ddots & \ddots & \ddots & 0 \\ \vdots & \ddots & 0 & 1 & -\alpha_N \\ 0 & \cdots & 0 & 0 & 1 \end{pmatrix} \begin{pmatrix} c_{\ell,1}^{m+1} \\ c_{\ell,2}^{m+1} \\ \vdots \\ c_{\ell,N-1}^{m+1} \\ c_{\ell,N}^{m+1} \end{pmatrix} = \begin{pmatrix} \beta_2 \\ \beta_3 \\ \vdots \\ \beta_N \\ \beta_{N+1} \end{pmatrix} \tag{4.25}$$

with the new coefficients of the system matrix

$$\alpha_2 = \frac{a_{E,1}}{a_{P,1}}, \quad \alpha_{n+1} = \frac{a_{E,n}}{a_{P,n} - a_{W,n}\alpha_n} \quad \text{for} \quad n = 2, 3, \ldots, N-1 \tag{4.26}$$

and the new entries of the source term vector

$$\beta_2 = \frac{b_1}{a_{P,1}}, \quad \beta_{n+1} = \frac{b_n + a_{W,n}\beta_n}{a_{P,n} - a_{W,n}\alpha_n} \quad \text{for} \quad n = 2, 3, \ldots, N\ . \tag{4.27}$$

Instead of the forward elimination equ. 4.25 can also be derived using the LU-factorization of the system matrix $\boldsymbol{A} = \boldsymbol{LU}$ with $\boldsymbol{L}$ being a lower and $\boldsymbol{U}$ being an upper triangular matrix and multiplication of the resulting equation with $\boldsymbol{L}^{-1}$.

In the second step the solution of the system of equations 4.25 can be found by back substitution using the following relations

$$\begin{aligned} c_{\ell,N} &= \beta_{N+1} \\ c_{\ell,n} &= \beta_{n+1} + \alpha_{n+1} c_{\ell,n+1}, \qquad\qquad n = N-1,\ N-2, \ldots,\ 1\ . \end{aligned} \tag{4.28}$$

Therefore, in contrast to the standard Gaussian elimination in the presented method the number of arithmetic operations is proportional to the number of grid points N. Additionally, since only the non-zero elements of the system matrix have to be stored the memory requirement is of order N as well.

4.3.2. Iterative Solver

Same as for the diffusion equation in a first step the discrete equivalent system for the potential in the solid and liquid phase is derived. Due to the implicit structure of the equations via the Butler-Volmer equation the standard CVM is slightly modified. In the following the discretization scheme is described on the example of the potential in the solid phase within the negative electrode. Since the potential $\phi_{s,1}$ on the electrode boundary is known to be 0 from the equation for the first control volume

$$-\left(\sigma_{e_1}^{\text{eff}}\frac{(\phi_{s,2}-\phi_{s,1})}{(\delta x)_{e_1}}\right)_{e_1} = i - a\bar{j}_1\Delta x_1 \tag{4.29}$$

the potential in the second control volume $\phi_{s,2}$ can be derived with $a\bar{j}_1\Delta x_1$ being the boundary flux at the interface between the control volumes 1 and 2. Now that the potential $\phi_{s,2}$ is known the potential in the third control volume can be calculated from

$$-\left(\sigma_{e_2}^{\text{eff}}\frac{(\phi_{s,3}-\phi_{s,2})}{(\delta x)_{e_2}}\right)_{e_2} + \left(\sigma_{\text{w}_2}^{\text{eff}}\frac{(\phi_{s,2}-\phi_{s,1})}{(\delta x)_{\text{w}_2}}\right)_{\text{w}_2} = -a\bar{j}_2\Delta x_2 \; . \tag{4.30}$$

For symmetry reasons with the effective conductivities in the solid $\sigma_{e_1}^{\text{eff}} = \sigma_{\text{w}_2}^{\text{eff}}$ and the distances between the grid points $(\delta x)_{e_1} = (\delta x)_{\text{w}_2}$ this relation can be simplified by building the sum between equ. 4.29 and equ. 4.30 resulting in

$$-\left(\sigma_{e_2}^{\text{eff}}\frac{(\phi_{s,3}-\phi_{s,2})}{(\delta x)_{e_2}}\right)_{e_2} = i - a\bar{j}_1\Delta x_1 - a\bar{j}_2\Delta x_2 \; . \tag{4.31}$$

Thus, the same structure as in equ. 4.29 is obtained representing only a 'half' control volume and the flux entering via the western interface. This procedure of replacing the western 'half' control volume with the boundary flux can be continued successively throughout the whole electrode resulting in an equation system with a triangular system matrix

$$\begin{pmatrix} -a_{E,1} & 0 & 0 & \cdots & 0 \\ a_{E,2} & -a_{E,2} & \ddots & \ddots & \vdots \\ 0 & a_{E,3} & -a_{E,3} & \ddots & 0 \\ 0 & \ddots & \ddots & \ddots & 0 \\ 0 & \cdots & 0 & a_{E,N-1} & -a_{E,N-1} \end{pmatrix} \begin{pmatrix} \phi_{s,2} \\ \phi_{s,3} \\ \phi_{s,4} \\ \vdots \\ \phi_{s,N} \end{pmatrix} = - \begin{pmatrix} -i + b_1 + a_{E,1}\phi_{s,1} \\ -i + b_1 + b_2 \\ -i + b_1 + b_2 + b_3 \\ \vdots \\ -i + \sum_{n=1}^{N-1} b_n \end{pmatrix} \tag{4.32}$$

with the coefficients of the system matrix

$$a_{E,n} = \frac{\sigma_{e_n}^{\text{eff}}}{(\delta x)_{e_n}} \tag{4.33}$$

and the entries in the source term vector representing the flux between two neighboring control volumes

$$b_n \;=\; a\bar{j}_n \Delta x_n \;. \tag{4.34}$$

With $\phi_{s,1}$ being given due to the structure of the matrix the potential distribution can be obtained by applying forward elimination

$$\phi_{s,n} \;=\; -\frac{1}{a_{E,n-1}}\left(i - \sum_{k=1}^{n-1} b_k - a_{E,n-1}\phi_{s,n-1}\right) \quad \text{for} \quad n = 2, 3, \ldots, N \;. \tag{4.35}$$

In the same way, assuming $\tilde{\phi}_{\ell,1}$ being known as well, the relation for the potential distribution in the liquid phase can be derived as follows

$$\tilde{\phi}_{\ell,n} \;=\; -\frac{1}{a_{E,n-1}}\left(0 + \sum_{k=1}^{n-1} b_k - a_{E,n-1}\tilde{\phi}_{\ell,n-1}\right) \quad \text{for} \quad n = 2, 3, \ldots, N \;. \tag{4.36}$$

Looking at the terms in brackets in equ. 4.35 and 4.36 it can be observed that the electric current density is successively transferred into an ionic one throughout the electrode. The proposed method is related to multiple shooting where the boundary value problem is replaced by a series of initial value problems as described in e.g. [12], [26] or [66]. In fig. 4.7 this splitting of the current density into a solid and a

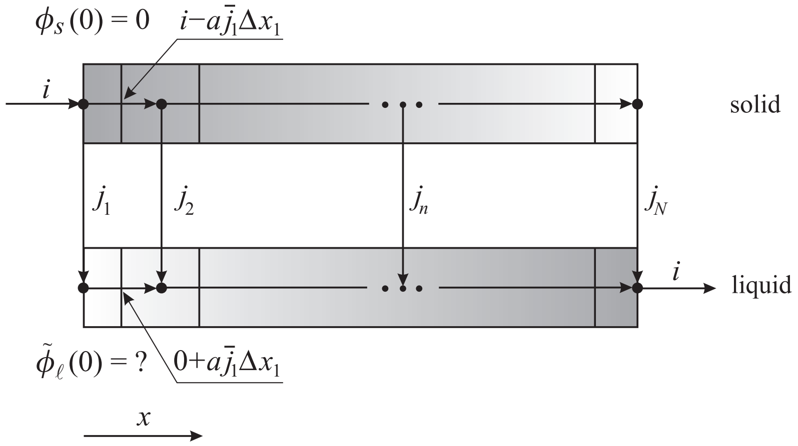

Figure 4.7.: Division of the current density into an electric and ionic fraction. Within the negative electrode the electric current density entering the electrode is transformed completely into an ionic current density (modified from [71]).

liquid fraction is shown graphically. Additionally, it has to be guaranteed that the integral of the reaction current density j equals the overall current density i entering via the electrode boundary. Thus, the integral is approximated by building the sum over all partial reaction current densities

$$a \int_0^L j \mathrm{d}x \; = \; \sum_{n=1}^{N} b_n \; = \; \sum_{n=1}^{N} a \bar{j}_n \Delta x_n \; = \; i \; . \tag{4.37}$$

From forward elimination the sum of b_n is already known until $N-1$. Therefore, only the last element has to be added to obtain the required sum. Since the calculation is only based on an assumption of $\tilde{\phi}_{\ell,1}$ in the next step a $\tilde{\phi}_{\ell,1}$ has to be found that fulfills equ. 4.37. Calculating the potential distributions on the positive electrode follows the same principle with the difference of $\tilde{\phi}_{\ell,1}$ being known and $\phi_{s,1}$ being the variable to be searched for. Due to the strong nonlinear coupling of the potentials with the reaction current densities via exponential functions the search for suitable values for $\phi_{s,1}$ and $\tilde{\phi}_{\ell,1}$ is numerically difficult. To ensure global convergence of the algorithm in the following a combination of the Newton algorithm with the bisection method as proposed in [71] is used. The applied strategy has the advantage that a possible overshoot in the accumulated reaction current density can be detected early and thus allowing an efficient problem handling avoiding early abortion of the algorithm. Improvements on the Newton algorithm as well as the introduction of the bisection method have been realized in cooperation with the *K2 Competence Center Virtual Vehicle*.

The Newton Method

Following the Newton approach the update of the solution variable from iteration step k to $k+1$ is calculated by

$$\tilde{\phi}_{\ell,1}^{(k+1)} \; = \; \tilde{\phi}_{\ell,1}^{(k)} + \lambda^{(k)} s^{(k)} \tag{4.38}$$

with the Newton step size

$$s^{(k)} = -\frac{f^{(k)}}{g^{(k)}} \tag{4.39}$$

and $\lambda^{(k)} \in (\, 0, 1 \,]$ being a scaling factor. To obtain an optimal performance for the applied method utilizing the full Newton step size $s^{(k)}$ whenever possible a backtracking scheme according to [25] is used for the calculation of the scaling factor $\lambda^{(k)}$. Whereas the error required in equ. 4.39 can be calculated directly by building the difference of the calculated to the desired value of the current density

$$f^{(k)} = \sum_{n=1}^{N} b_n^{(k)} - i \tag{4.40}$$

the gradient being the derivative of $f^{(k)}$ with respect to $\tilde{\phi}_{\ell,1}^{(k)}$ is only approximated. Therefore, since all potentials are depending on $\tilde{\phi}_{\ell,1}^{(k)}$ the gradient can be expressed by

$$g^{(k)} = \sum_{n=1}^{N} \frac{\partial b_n^{(k)}}{\partial \tilde{\phi}_{\ell,1}^{(k)}} = \sum_{n=1}^{N} \frac{\partial b_n^{(k)}}{\partial \tilde{\phi}_{\ell,n}^{(k)}} \frac{\partial \tilde{\phi}_{\ell,n}^{(k)}}{\partial \tilde{\phi}_{\ell,1}^{(k)}} \tag{4.41}$$

splitting up the derivative of $b_n^{(k)}$ after $\tilde{\phi}_{\ell,1}^{(k)}$ in two terms. Furthermore, the derivative of $\tilde{\phi}_{\ell,n}^{(k)}$ after $\tilde{\phi}_{\ell,1}^{(k)}$ in equ. 4.41 can be written as a product requiring only the derivatives of the potentials at neighboring points. Since the potentials can be assumed to be changing at a low rate between two neighboring control volumes the required derivative can be simplified to

$$\frac{\partial \tilde{\phi}_{\ell,n}^{(k)}}{\partial \tilde{\phi}_{\ell,1}^{(k)}} = \prod_{j=1}^{n-1} \frac{\partial \tilde{\phi}_{\ell,n-j+1}^{(k)}}{\partial \tilde{\phi}_{\ell,n-j}^{(k)}} \approx 1 \; . \tag{4.42}$$

Therefore the gradient can be approximated by

$$g^{(k)} \approx \sum_{n=1}^{N} \frac{\partial b_n^{(k)}}{\partial \tilde{\phi}_{\ell,n}^{(k)}} \tag{4.43}$$

requiring no inner derivative of $\tilde{\phi}_{\ell,n}^{(k)}$ after $\tilde{\phi}_{\ell,1}^{(k)}$. The end of the Newton iteration is reached when either the error falls below a specified tolerance limit tol

$$\left| \sum_{n=1}^{N} b_n^{(k)} - i \right| < \mathrm{tol} \tag{4.44}$$

or a maximum number of iterations is reached. Further, to spare iterations when $\tilde{\phi}_{\ell}^{(k)}$ is only changing insignificantly from one iteration to the other the step size $|s^{(k)}|$ should also be observed. The remaining rest current density is distributed equally over all control volumes within the electrode. Although the Newton method is a powerful technique of quadratic convergence it suffers from some limitations which can lead to non-convergence of the algorithm especially if a poor initial estimate $\tilde{\phi}_{\ell,1}^{(0)}$ is chosen. To avoid this behavior and to ensure global convergence of the algorithm the Newton scheme is extended with the bisection method.

The Bisection Method

Since the bisection or binary search method is based on the intermediate value theorem a bracket $[l,u]$ around $\tilde{\phi}_{\ell,1}$ minimizing the error f between the calculated and the desired value of the current density can be found such that $f(\ell)$ and $f(u)$ are of opposite sign. In the following in each iteration step the interval $[l,u]$ can be divided into two subintervals and a new bracket around $\tilde{\phi}_{\ell,1}^{(k)}$ can be determined by evaluating

$$\begin{array}{rcll} f(\ell)\cdot f(\tilde{\phi}_{\ell,1}^{(k)}) & > & 0 & l=\tilde{\phi}_{\ell,1}^{(k)} \\ f(\ell)\cdot f(\tilde{\phi}_{\ell,1}^{(k)}) & < & 0 & u=\tilde{\phi}_{\ell,1}^{(k)} \end{array} \tag{4.45}$$

with $\tilde{\phi}_{\ell,1}^{(k)}$ being the midpoint between l and u. In fig. 4.8 the principle of continuously narrowing the interval $[\ell,u]$ around the root of the error function $\tilde{\phi}_{\ell,1}$ is shown graphically. The main drawback of the method is that it converges very slowly compared to other methods. According to [18] the convergence behavior of the bisection method can be approximated by

$$|\tilde{\phi}_{\ell,1}^{(k)}-\tilde{\phi}_{\ell,1}| \leq \frac{u-\ell}{2^k} \qquad k \geq 1 \tag{4.46}$$

with k being the number of iterations. Nevertheless, as implied in equ. 4.46 the

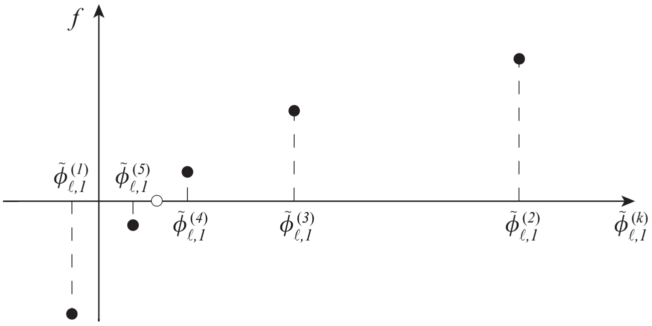

Figure 4.8.: Iterative approximation of $\tilde{\phi}_{\ell,1}^{(k)}$ to the root of the error function $\tilde{\phi}_{\ell,1}$ with the bisection method. The root of the error function is indicated by the white dot.

bisection method has the advantage that it always converges to a solution. Therefore, as proposed in [18], it can be used as a 'starter' giving a rough approximation to the solution for more efficient methods such as the Newton method described previously. However, in this thesis the bisection method is only used if either the solution does not convergence to a satisfactory solution within a specified number of iterations or a poor initial estimate has been chosen such that the calculated current density becomes infinite.

4.4. Improving the Model Performance

Because not every parameter in the lithium-ion battery is directly accessible parameter estimation routines are needed to parametrize the electrochemical model. Thus, the model has to be solved several times to obtain a proper set of parameters. To minimize the overall calculation effort besides an efficient parameter estimation routine a fast battery model is required. Therefore, in the following a variable time stepping as well as a model order reduction scheme are introduced. The latter is based on a reformulated version of the diffusion equation in the solid phase.

4.4.1. Adaptive Time Stepping Scheme

According to [48] for the choice of the step size for time discretization using a step-by-step method two things have to be considered. On the one hand the step size should not be chosen too small to avoid a large number of steps as well as the corresponding accumulation of the round-off error and on the other hand the step size should not be chosen too large to avoid a large truncation error. Additionally, to spare calculation time as well as memory requirements for long term simulations it is advantageous to use an adaptive step size considering these constraints. The adaptive time stepping scheme described in this section is based on the information given in [59] and has been realized with the support of the *K2 Competence Center Virtual Vehicle*. Therefore, as shown in fig. 4.9, the simulation result u_c obtained by taking a full step Δt and u_f taking two half steps $\Delta t/2$ are compared to each other introducing an error measure

$$\delta = \left\| \frac{u_c - u_f}{u_f} \right\|_\infty \tag{4.47}$$

being the maximum relative error between u_c and u_f. The decision whether to keep or discard an actual time step is determined by comparing δ to a local goal error δ_g

after the scheme proposed in [59].

```
if      $\delta < \frac{1}{2}\delta_g$
    accept solution + $\Delta t_{m+1} = \Delta t_m \cdot 1.5$
elseif  $\frac{1}{2}\delta_g \leq \delta < \delta_g$
    accept solution + $\Delta t_{m+1} = \Delta t_m$
elseif  $\delta_g \leq \delta < 2\delta_g$
    accept solution + $\Delta t_{m+1} = \Delta t_m \cdot 0.5$
elseif  $\delta \geq 2\delta_g$
    decline solution + $\Delta t_m = \Delta t_m \cdot 0.5$
end
```

This procedure is performed for all diffusion equations. Thus, the step size for the overall system is limited by the minimum step size obtained for the actual time step. The step size is bounded in the interval

$$1 \text{ ms} \leq \Delta t \leq 60 \text{ s} \tag{4.48}$$

avoiding a possible runaway of the step size in both directions. To guarantee a correct reproduction of a preset current profile the step size at the end of a charge or discharge pulse is shortened such that the interval boundary of a certain pulse is not exceeded.

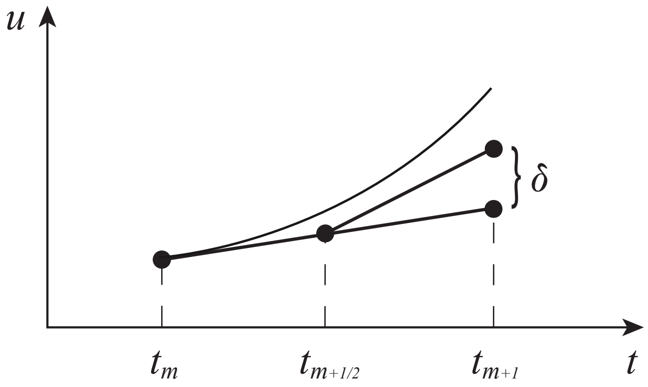

Figure 4.9.: Basic concept of the variable time stepping scheme comparing the solutions obtained taking a full step and two half steps introducing the error measure δ.

4.4.2. Reduction of the Calculation Effort for the Particle Diffusion

From the Butler-Volmer equation it can be seen that only certain values of the particle concentration are of interest and thus the exact concentration profile over the particle is not required. Therefore, in equs. 3.20 and 3.22 only the surface concentration c_s^{surf}, where the reaction with the electrolyte takes place, as well as the average concentration c_s^{ave} in the bulk, being a measure for the amount of lithium being transfered, are needed to solve the overall system of equations. Since the particles are distributed all over the electrode the concentration equation for the particles has to be calculated several times and thus requiring a lot of computation time. Therefore, to obtain a fast battery model the number of discretization points within the particle has to be minimized. By doing so one has to guarantee that the system dynamics on the one hand as well as the amount of lithium transferred is being preserved. Parts of the following section on the reduction of the calculation effort have already been published in [79] and [80].

Due to the nonlinear structure of the diffusion equation in a single particle in a first attempt equ. 3.33 is discretized following the approach given in [55] for the nonlinear heat conduction problem with a varying thermal conductivity. Therefore, same as for the CVM, the differential $r^2 D_s(\partial c_s/\partial x)$ is approximated at interfaces halfway between the grid points using a centered approximation resulting in

$$\left(r^2 D_s \frac{\partial c_s}{\partial x}\right)_e = r_e^2 D_{s,e}\frac{(c_{s,E}-c_{s,P})}{(\delta r)_e} \;;\; \left(r^2 D_s \frac{\partial c_s}{\partial x}\right)_{\mathrm{w}} = r_{\mathrm{w}}^2 D_{s,\mathrm{w}}\frac{(c_{s,P}-c_{s,W})}{(\delta r)_{\mathrm{w}}} . \tag{4.49}$$

In contrast to the standard CVM scheme where the whole equation is integrated within the interval w and e a second differentiation is performed. Therefore, one finally obtains a centered approximation for the right hand side of equ. 3.33 resulting in

$$\frac{1}{r^2}\frac{\partial}{\partial x}\left(r^2 D_s \frac{\partial c_s}{\partial x}\right) \approx \frac{1}{\Delta r}\left[\frac{r_e^2}{r_P^2}\left(\frac{D_{s,e}(c_{s,E}-c_{s,P})}{(\delta r)_e}\right)_e - \frac{r_{\mathrm{w}}^2}{r_P^2}\left(\frac{D_{s,\mathrm{w}}(c_{s,P}-c_{s,W})}{(\delta r)_{\mathrm{w}}}\right)_{\mathrm{w}}\right] \tag{4.50}$$

at the discretization point P which is equal to the result given in [19]. Since equ. 4.50 can be regarded as a balance equation between the input and output flux at the interfaces w and e the boundary conditions can be incorporated by simply replacing the derivatives on the boundaries by the given boundary flux. For the time discretization again the fully implicit scheme is used resulting in

$$\frac{\left(c_{s,P}^{m+1}-c_{s,P}^{m}\right)}{\Delta t} = \frac{1}{\Delta r}\left[\frac{r_e^2}{r_P^2}\left(\frac{D_{s,e}(c_{s,E}^{m+1}-c_{s,P}^{m+1})}{(\delta r)_e}\right)_e - \frac{r_{\mathrm{w}}^2}{r_P^2}\left(\frac{D_{s,\mathrm{w}}(c_{s,P}^{m+1}-c_{s,W}^{m+1})}{(\delta r)_{\mathrm{w}}}\right)_{\mathrm{w}}\right] \tag{4.51}$$

for the discretization point P. Since no 'half' control volumes on the domain boundaries are used according to [19] the required surface concentration is obtained by solving equ. 4.51 and approximating the outward concentration derivative by a three point backward difference. To investigate the influence of the discretization on the surface concentration an error analysis is performed. As a reference the surface concentration is calculated at the end of a 3400 s constant current discharge at 1 C where 97 % of the lithium within the particle are consumed using 1000 discretization points in the particle. Assuming a uniform current distribution across the electrode according to [78] the required boundary flux can be calculated from the preset discharge current density by $i/(aLF)$. In fig. 4.10 the distribution of the relative error with respect to the reference concentration $c_s^{\text{surf}}(t_{\text{end}})$ together with the calculation time required versus the number of discretization points N is shown. The strong decay of the relative error is related to the decreasing asymmetrie in the system matrix with the fraction r_e^2/r_P^2 and r_w^2/r_P^2 approaching 1 by increasing the number of discretization points N. Additionally for the three point backward difference significant points near the boundary are required to obtain reliable results for c_s^{surf}. Therefore, to overcome these limitations in the choice of N an alternative discretization scheme allowing a direct calculation of c_s^{surf} is sought after. Furthermore, according to [13]

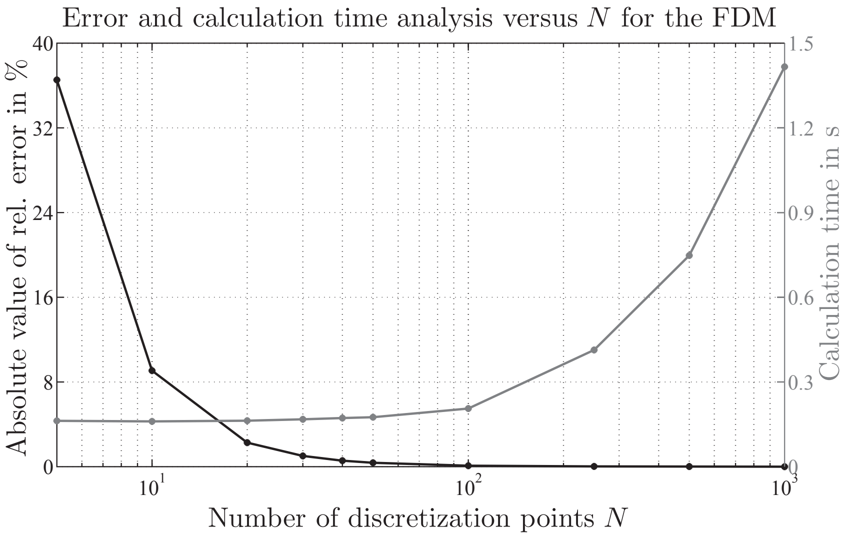

Figure 4.10.: Analysis of the relative error at the particle surface at the end of a 3400 s discharge at 1 C together with the calculation time required for a different number of discretization points N using the FDM approach (from [79]).

for a PDE with derivative terms included in both boundary conditions (e.g. Neumann or Robin type boundary conditions) the CVM is preferable since in contrast to the FDM it does not fail to preserve mass even for a low number of N.

Reformulation of Diffusion in the Particle

To exploit the property of the CVM of mass conservation also for the nonlinear diffusion equation in the particle represented by equ. 3.33 the change of variables proposed in [6] is performed

$$\tilde{c}_s \quad \leftarrow \quad r c_s \tag{4.52}$$

with $\tilde{c}_s$ being the transformed concentration. Additionally, same as for the diffusion in the liquid, the diffusion coefficient D_s is assumed to be constant within the particle. Therefore, one obtains the desired linear structure and the CVM can be applied directly

$$\int\limits_{\mathrm{w}}^{e} \frac{\partial \tilde{c}_s(r,t)}{\partial t} \mathrm{d}r \quad = \quad D_s \int\limits_{\mathrm{w}}^{e} \frac{\partial}{\partial r} \left[\frac{\partial \tilde{c}_s(r,t)}{\partial r} \right] \mathrm{d}r \tag{4.53}$$

requiring no approximation of the integrals over the single control volumes. Using an implicit time discretization scheme the discrete equivalent system for the particle diffusion for a discretization point P evolving from timestep m to $m+1$ can be written as follows

$$\frac{\left(\tilde{c}_{s,P}^{m+1} - \tilde{c}_{s,P}^{m}\right)}{\Delta t} \Delta r \quad = \quad \left(\frac{D_{s,e}(\tilde{c}_{s,E}^{m+1} - \tilde{c}_{s,P}^{m+1})}{(\delta r)_e} \right)_e - \left(\frac{D_{s,\mathrm{w}}(\tilde{c}_{s,P}^{m+1} - \tilde{c}_{s,W}^{m+1})}{(\delta r)_{\mathrm{w}}} \right)_{\mathrm{w}} . \tag{4.54}$$

After applying a back substitution and rearranging the resulting discretized equation one finally obtains

$$\frac{\left(c_{s,P}^{m+1} - c_{s,P}^{m}\right)}{\Delta t} \Delta r = \left(\frac{D_{s,e}(\frac{r_E}{r_P} c_{s,E}^{m+1} - c_{s,P}^{m+1})}{(\delta r)_e} \right)_e - \left(\frac{D_{s,\mathrm{w}}(c_{s,P}^{m+1} - \frac{r_W}{r_P} c_{s,W}^{m+1})}{(\delta r)_{\mathrm{w}}} \right)_{\mathrm{w}} \tag{4.55}$$

for the original concentration. Although the discretization dependency has been reduced with this approach the asymmetry in the system matrix is still present and thus limiting the reduction of N. Since the exact concentration profile, which is not accessible by measurements, is not required but mainly the amount of lithium transferred within a certain time interval is of interest the right hand side of equ. 4.55 can be approximated such that the balance between input and output flux is being preserved. Thus, to obtain the desired symmetric structure the spherical diffusion equation is mapped on an equivalent linear one

$$\frac{\left(c_{s,P}^{m+1} - c_{s,P}^{m}\right)}{\Delta t}\Delta r \approx \left(\frac{\tilde{D}_{s,e}(c_{s,E}^{m+1} - c_{s,P}^{m+1})}{(\delta r)_e}\right)_e - \left(\frac{\tilde{D}_{s,\mathrm{w}}(c_{s,P}^{m+1} - c_{s,W}^{m+1})}{(\delta r)_\mathrm{w}}\right)_w \tag{4.56}$$

with $\tilde{D}_{s,e}$ and $\tilde{D}_{s,w}$ representing the new diffusion coefficients at the interfaces between neighboring control volumes. Considering the assumptions made for the diffusion properties in porous media by introducing the spherical particle representation the approximation in equ. 4.56 can describe the diffusion characteristics in the solid with sufficient accuracy since most electrode materials have a preferred diffusion direction and are composed of particles of arbitrary shape and size. To compare the error distribution obtained with the CVM based method again the surface distribution at the end of a 3400 s discharge with 1 C is evaluated. In contrast to the FDM with the CVM c_s^{surf} can be calculated directly by introducing a 'half' control volume at the outer boundary. Figure 4.11 shows the resulting error distribution together

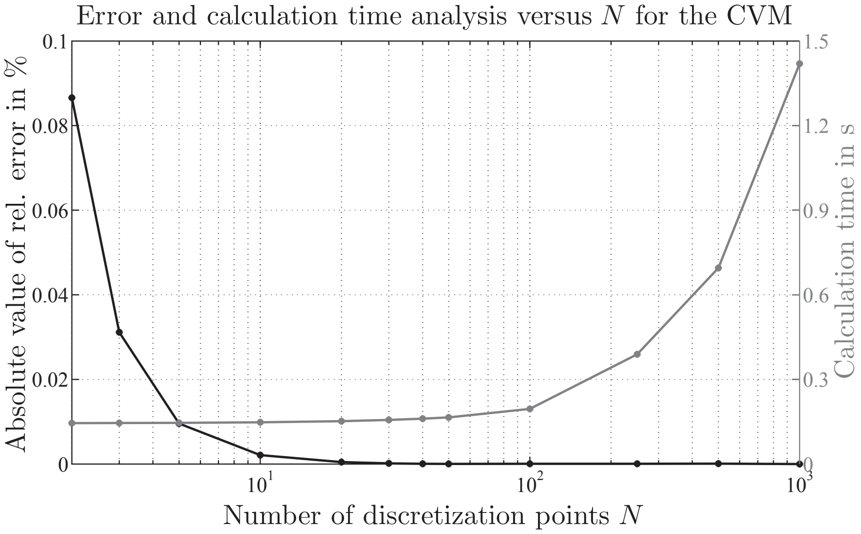

Figure 4.11.: Analysis of the relative error at the particle surface at the end of a 3400 s discharge at 1 C together with the calculation time required for a different number of discretization points N using the modified CVM approach (from [79]).

with the calculation time required against the number of discretization points N for the CVM. Whereas the distribution of the calculation time is nearly the same as for the FDM the error level for low numbers of N has been reduced remarkably with the error remaining < 0.1 % using $N < 5$. Thus, the error obtained with the CVM is even below the error between both methods using the reference discretization of $N = 1000$ being 0.31 %. In tab. 4.1 the results for the FDM and CVM are compared for two test cases. In the first case the discretization is chosen such that the same accuracy level for both methods is achieved whereas in the second case both methods are in the range of the error between the two methods. In both examples the CVM requires a factor 10 less discretization points.

Table 4.1.: Comparison of FDM to CVM results with respect to calculation speed and accuracy after a simulation time of 3400 s (from [79]).

method	number of discretization points N	rel. error on particle surface in %	calculation time in s
FDM	500	$2.7 \cdot 10^{-3}$	0.789
CVM	10	$2.1 \cdot 10^{-3}$	0.148
FDM	50	0.36	0.177
CVM	2	0.087	0.145

Since not only the static but also the dynamic behavior of the particle diffusion is of interest also simulations using pulse excitation are performed. Therefore, in fig. 4.12 and 4.13 the results obtained with the FDM are compared to the CVM results using 1 C pulses with a pulse length of 100 s by evaluating the normalized surface concentration $c_s^{\mathrm{surf}}/c_s^{\mathrm{max}}$ for two different values of the diffusion coefficient D_s. If there is no diffusion limitation related to a homogeneous concentration distribution in the particle as is the case in fig. 4.12 there is nearly no difference between both methods. On the other hand if there is a strong diffusion limitation related to a strong concentration gradient in radial direction as shown in fig. 4.13 the results are slightly differing. Since the shape of c_s^{surf} is preserved and the maximum error is still < 1 % for further investigations the CVM based approach can be used.

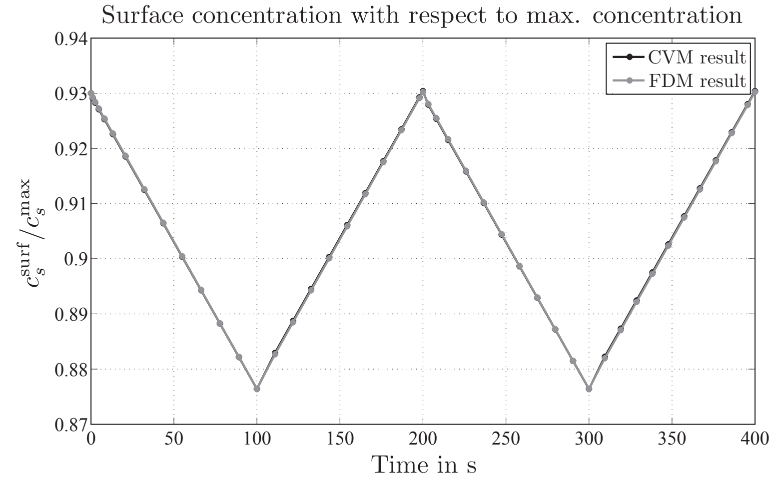

Figure 4.12.: Surface concentration with respect to the maximum concentration for a particle without diffusion limitation using 10 discretization points in the bulk. Due to the homogeneous concentration distribution there is nearly no difference between the CVM and FDM results being visible.

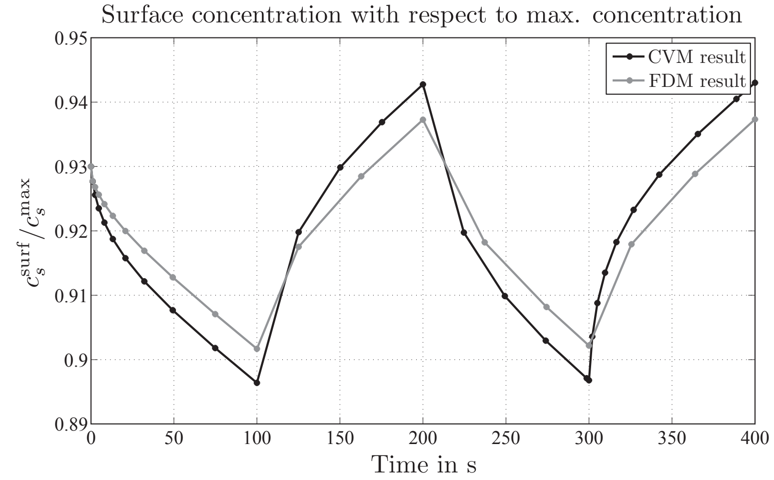

Figure 4.13.: Surface concentration with respect to the maximum concentration for a strong diffusion limitation using 10 discretization points in the bulk. Due to the stronger diffusion limitation and the resulting concentration gradient in the bulk the results of the CVM compared to the FDM are differing but still the maximum error remains $< 1\%$.

Investigation of the Particle Dynamics with POD

Since so far in this thesis only the advantage of the CVM of mass conservation even for a small number of N has been exploited in the following a more specific approach for the reduction of discretization points considering the particle dynamics is introduced. A reduced basis method for finite volume approximations has also been published in [36]. Same as in [19] the starting point for the proposed point reduction is a so-called proper orthogonal decomposition (POD) on the basis of which a low-dimensional representation of the high-dimensional problem without losses in the system characteristics can be derived. For discrete problems the required orthogonal basis functions $\{\boldsymbol{\varphi}_i\}_{i=1}^{\ell}$ can be obtained by solving the symmetric $N \times N$ eigenvalue problem

$$\boldsymbol{K}\bar{\boldsymbol{\varphi}}_i = \lambda_i \bar{\boldsymbol{\varphi}}_i \quad \text{for} \quad 1 \leq i \leq \ell \tag{4.57}$$

with eigenvalues λ_i and using the substitution

$$\bar{\boldsymbol{\varphi}}_i = \boldsymbol{W}^{1/2}\boldsymbol{\varphi}_i \,. \tag{4.58}$$

The kernel function

$$\boldsymbol{K} = \boldsymbol{W}^{1/2}\boldsymbol{Y}\boldsymbol{D}\boldsymbol{Y}^T\boldsymbol{W}^{1/2} \tag{4.59}$$

is composed of a precalculated high-dimensional solution to the concentration equation at M different time steps

$$\boldsymbol{Y} = [\boldsymbol{c}_s(t_1), \boldsymbol{c}_s(t_2), \ldots, \boldsymbol{c}_s(t_M)] \tag{4.60}$$

called snapshots, a $M \times M$ weighting matrix for the time discretization

$$\boldsymbol{D} = \operatorname{diag}\left\{\frac{\Delta t_1}{2}, \frac{\Delta t_1 + \Delta t_2}{2}, \ldots, \frac{\Delta t_{M-1} + \Delta t_M}{2}, \frac{\Delta t_M}{2}\right\} \tag{4.61}$$

containing the time step sizes Δt_m at each time step in the main diagonal as well as a $N \times N$ weighting matrix for the spatial discretization

$$\boldsymbol{W} = \operatorname{diag}\left\{\frac{\delta r_1}{2}, \frac{\delta r_1 + \delta r_2}{2}, \ldots, \frac{\delta r_{N-1} + \delta r_N}{2}, \frac{\delta r_N}{2}\right\} \tag{4.62}$$

with δr_n indicating the distance between the grid points. For the one dimensional case $\boldsymbol{W}$ has also only entries in the main diagonal. Due to the close connection between POD and singular value decomposition (SVD) for rectangular matrices as explained in [91] instead of equ. 4.57 a SVD of the discrete kernel function yielding

$$\mathrm{SVD}(\boldsymbol{K}) \quad = \quad \bar{\boldsymbol{\Phi}}\boldsymbol{\Lambda}\bar{\boldsymbol{\Phi}}^T \tag{4.63}$$

can be used. Therefore, from the column vectors of the square matrix $\bar{\boldsymbol{\Phi}}$, being the eigenvectors of $\boldsymbol{K}$, the orthogonal basis function $\{\boldsymbol{\varphi}_i\}_{i=1}^{\ell}$ can be calculated as follows

$$\boldsymbol{\varphi}_i \quad = \quad \boldsymbol{W}^{-1/2}\bar{\boldsymbol{\varphi}}_i \quad \text{for} \quad 1 \leq i \leq \ell \; . \tag{4.64}$$

Additionally a $N \times N$ diagonal matrix is obtained

$$\boldsymbol{\Lambda} \quad = \quad \mathrm{diag}\,\{\lambda_1, \lambda_2, \ldots, \lambda_N\} \tag{4.65}$$

containing the singular values which can be regarded as a measure for the importance of each orthogonal mode with N being the number of discretization points used. Furthermore, by applying the SVD the singular values and eigenvectors are sorted automatically such that the magnitude of λ_i is of decreasing order

$$\lambda_1 \geq \lambda_2 \geq \ldots \geq \lambda_N > 0 \; . \tag{4.66}$$

A more detailed analysis on using SVD for POD can be found in [52] and [83]. Alternatively, for more complex geometries where the calculation of $\boldsymbol{W}^{1/2}$ imply a high computational effort or for a large dimension of $\boldsymbol{W}$ the *method of snapshots* from [75] presents an efficient method to obtain the required orthogonal basis functions. Thus, instead of equ. 4.57 the symmetric $M \times M$ eigenvalue problem

$$\boldsymbol{K}\tilde{\boldsymbol{\varphi}}_i \quad = \quad \lambda_i\tilde{\boldsymbol{\varphi}}_i \quad \text{for} \quad 1 \leq i \leq \ell \tag{4.67}$$

with the kernel function

$$\boldsymbol{K} \quad = \quad \boldsymbol{D}^{1/2}\boldsymbol{Y}^T\boldsymbol{W}\boldsymbol{Y}\boldsymbol{D}^{1/2} \tag{4.68}$$

has to be solved. The orthogonal basis functions can than be calculated from

$$\boldsymbol{\varphi}_i \quad = \quad \frac{1}{\lambda_i}\boldsymbol{Y}\boldsymbol{D}^{1/2}\tilde{\boldsymbol{\varphi}}_i \quad \text{for} \quad 1 \leq i \leq \ell \; . \tag{4.69}$$

For further details it is referred to [91]. From the distribution of the singular values the characteristic modes of the system can be identified. To maintain the tridiagonal structure of the system matrix for the particle diffusion and thus requiring no modifications in the previously described solver architecture the calculation effort is not reduced by a transformation into a reduced order subspace based on the dominant orthogonal modes like in [19]. Instead, the POD is only used for data analysis to determine the required minimum discretization to preserve the dominant orthogonal modes in the system. Since there is no general rule on how to determine the number of the dominant orthogonal modes often same as in [19] the smallest number to satisfy the following inequality

$$\varepsilon(k) \quad = \quad \frac{\sum\limits_{i=1}^{k} \lambda_i}{\sum\limits_{i=1}^{N} \lambda_i} \geq 99.99\% \tag{4.70}$$

is chosen. Therefore the variable ε is called the energy content of the first k basis functions $\{\boldsymbol{\varphi_i}\}_{i=1}^{k}$. The challenging task is now to find a proper excitation to obtain a representative data set $\boldsymbol{Y}$ on the basis of which a low-dimensional representation of the diffusion in the particle can be derived. Thus, an a priori analysis as proposed in [52] is required. The applicability of a constant current charge/discharge profile with POD has already been published in [19] and [80]. Therefore, in this thesis, the analysis is extended to a dynamic test signal to cover as much operating conditions for a single particle and consequently the entire battery as possible. The resulting reduced particle model should also be able to reproduce rapid changes in the input signal, as is required for pulse excitation, correctly. Regarding these specifications white noise is considered to be a suitable test signal. Due to its wide bandwidth white noise is frequently used for system identification as well. Nevertheless, in the discrete case white noise can only be realized in a certain frequency band. Due to this property of band limitation a representative frequency band with sufficiently high frequency resolution for battery simulations has to be chosen. For the analysis a sample time of 50 ms and simulation time of 102.4 s with a frequency resolution of 9.8 mHz is used resulting in a bandwidth of 10 Hz. Additionally, due to the property of white noise of being zero-mean during the simulation with band-limited white noise nearly the same amount of lithium is inserted and deinserted in the particle respectively. In fig. 4.14 the distribution of the singular values of the kernel matrix $\boldsymbol{K}$ composed of the simulation results for excitation with band-limited white noise using a different

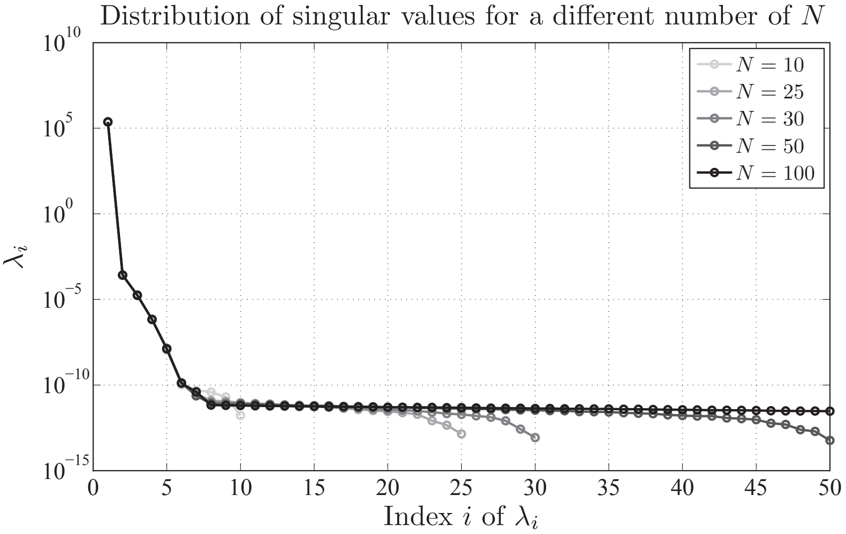

Figure 4.14.: Distribution of singular values of the kernel function $\boldsymbol{K}$ for white noise excitation using CVM for a different number of discretization points N in radial direction. For the dominant singular values there is nearly no discretization dependency visible.

number of discretization points N in radial direction is displayed. From the steep decay in the distribution of the singular values, indicating a low number of dominant orthogonal modes $\boldsymbol{\varphi}_i$, the applicability to derive a low-dimensional representation for the particle diffusion can be deduced. Since there is only a minor discretization dependency in the first few singular values, model order reduction can be performed by taking only a low number of points in the bulk. Even the shape of the curve is preserved except for the lowest number of discretization points of $N = 10$. However, due to the small values of the higher order singular values the energy content is mostly influenced by the lower order singular values. Investigating the orthonormal modes as shown in fig. 4.15 and 4.16 starting from the 4^{th} mode aliasing effects depending on the number of discretization points could be detected. Thus, convergence of the lower order models for $N \to \infty$ can be observed. A more detailed analysis on POD convergence and convergence rate can be found in e.g. [51] or [50]. Nevertheless, due to the dominance of the first mode these effects can be neglected although the ratio of the energy content falls slightly below the 99.99 % given in equ. 4.70. In tab. 4.2 the calculation times required together with the ratio of the energy content for the different number of discretization points are summarized. Therefore, the simulation time is increasing rapidly by taking more than 30 points.

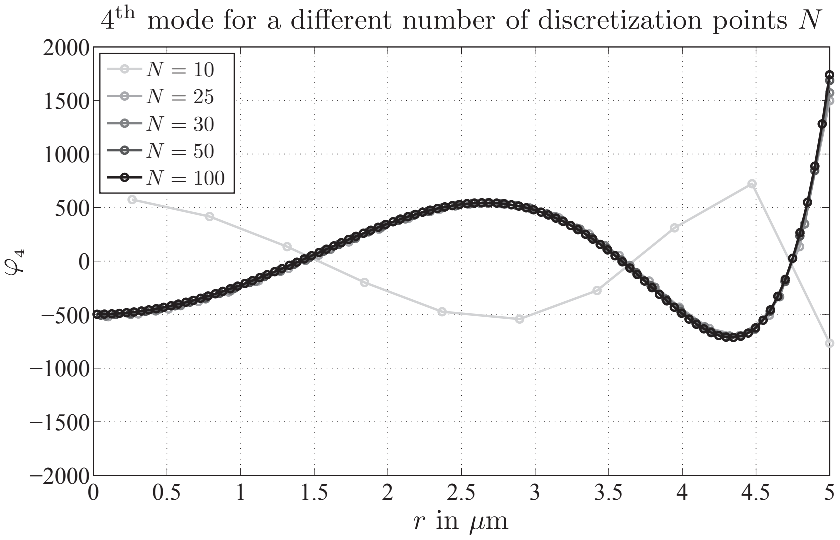

Figure 4.15.: 4th mode of the kernel function $\boldsymbol{K}$ for white noise excitation using CVM for a different number of discretization points N in radial direction. To avoid aliasing in the 4th mode N has to be > 10.

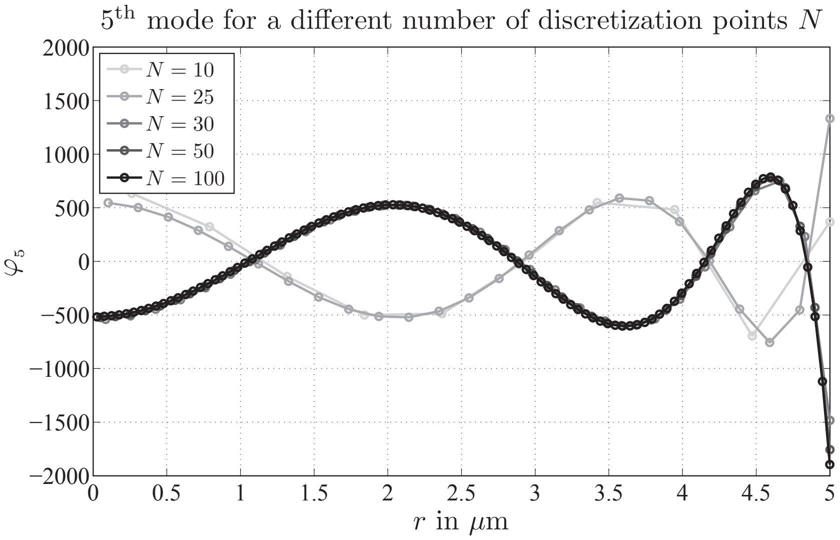

Figure 4.16.: 5th mode of the kernel function $\boldsymbol{K}$ for white noise excitation using CVM for a different number of discretization points N in radial direction. To avoid aliasing in the 5th mode N has to be > 25.

Thus, for the investigated particle for the choice of the discretization a trade-off between simulation time and accuracy in the interval $10 < N < 30$ is suggested.

Table 4.2.: Evaluation of the CVM with respect to energy content and calculation time for excitation with band-limited white noise using a different number of discretization points N.

# of N	$\sum_{i=1}^{N} \lambda_i \Big/ \sum_{i=1}^{100} \lambda_i$	calculation time in s
10	0.952	0.286
25	0.985	0.359
30	0.988	0.397
50	0.995	0.759
100	1.000	1.704

5. Results

In this chapter the ability of the developed model to reproduce the behavior of a lithium-ion battery and thus its applicability for battery condition monitoring is validated on small-size test cells. For that purpose a test pattern covering representative operating conditions for HEV and EV applications is simulated and the results compared to measurement data with the measured variables being terminal voltage and load current. Additionally, from these measurements internal quantities of the battery such as capacity, state of charge or cell impedance can be derived and monitored.

To ensure comparability between measurement and simulation a reference state for the model has to be defined. Therefore, to not change the amount of active lithium within the cell each simulation is started from the same SOC. Further, both for simulation and measurement all diffusion processes are assumed to be equalized. Thus, a rest period is required before each test pattern.

The 50 mAh Test Cell

For the comparison between measurement and simulation special 50 mAh LFP test cells made from commercial materials from Südchemie prepared by *GAIA*[1] are used. Due to their small capacity and accordingly energy content the fault behavior of the cells is rather unproblematic and testing of the cells can be performed in a standard testing environment. Further, large C-rates at comparatively low charge/discharge currents are possible allowing to test several cells simultaneously instead of one large-sized cell. Additionally, for the small-sized pouchbag cell a uniform temperature distribution can be assumed and thus requiring no additional thermal model of the cell. In fig. 5.1 the build-up of a non-activated test cell consisting of the active materials of the electrodes connected to the current collectors, a separator foil, an electrolyte bag, a plastic tube and pouch foil is displayed. For the measurements an additional lithium reference electrode is attached to distinguish between the fractions of the positive and negative electrode to the overall cell potential. After assembly of the

---

[1] `http://www.gaia-akku.com/`

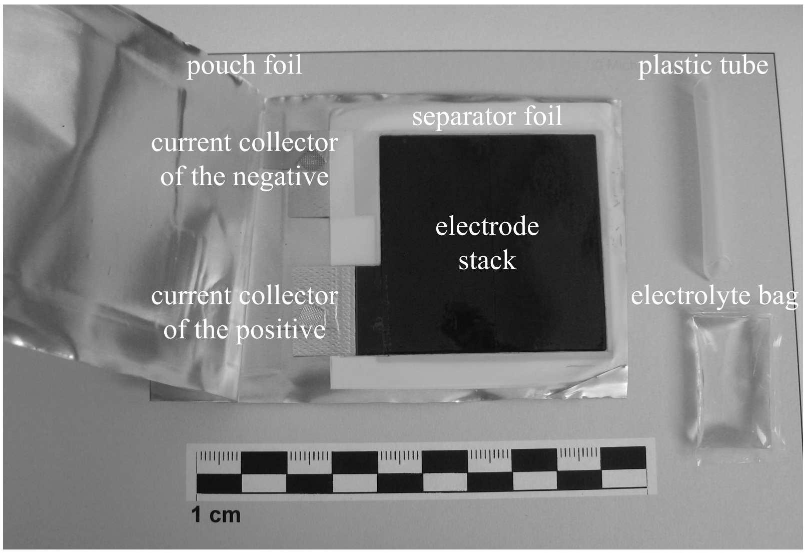

Figure 5.1.: Build-up of the 50 mAh pouchbag test cell consisting of the active materials of the electrodes, separator foil, current collectors, an electrolyte bag, a plastic tube, and pouch foil. After assembly of the whole system the pouch is evacuated and sealed with a welding line (foto provided by Michael Sternad of the Institute for Chemistry and Technology of Materials (ICTM), Graz University of Technology).

cell the pouch is evacuated and sealed with a welding line. To activate the cell the electrolyte bag has to be squashed. Due to the vacuum inside the cell the surplus electrolyte is collected in the free volume of the plastic tube. Before the cell is ready to be used a so-called formation process has to be run through until the cell reaches its full capacity.

At this point it has to be mentioned that the parametrization of the model is not part of this thesis. The set of parameters used for the upcoming simulations has been collected within the 'COMET K2 project: *Modellierung, Validierung und Test von Lithium-Ionen-Batterien für Hybridfahrzeuge*' and is composed of manufacturer informations as well as measurements. Furthermore, for the remaining parameters which are not accessible by measurements a parameter optimization is performed at the *K2 Competence Center Virtual Vehicle*[2] in accordance with literature values.

---

[2] http://www.vif.tugraz.at/

5.1. Measurements on the 50 mAh Test Cell in the Time Domain

For the measurements in the time domain the battery testing system BT 2000 from *Arbin Instruments*[3] located at the *K2 Competence Center Virtual Vehicle* is available. Due to the unhandiness of the BT 2000 additionally a 1 channel battery testing board offering a greater flexibility has been developed by Daniel Hrach at the institute. In fig. 5.2 the layout of the 1 channel battery testing board is shown. Due to the modular layout of the board the test system can be easily extended with further channels using a common power supply. Both testing equipments can provide a charge/discharge current up to 5 A/channel and are controlled via a host PC where the acquired measurement data for temperature, voltage and current are stored for later evaluation. The data handling for the comparison with the simulation results is carried out with the software package MATLAB®. Further, to be able to study the temperature behavior the cells are tested at several temperatures within a climatic chamber.

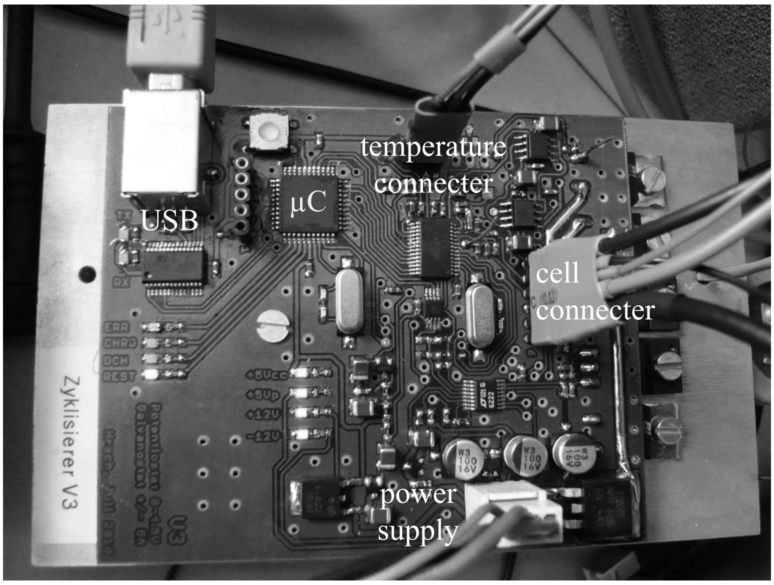

Figure 5.2.: 1 channel mobile battery testing board with current/voltage measurement using the 4-wire technique, temperature output, and USB communication to a host PC allowing a maximum charge/discharge current of 5 A developed by Daniel Hrach at the institute.

---

[3] `http://www.arbin.com/`

5.1.1. Measurement of the Open Circuit Voltage

The open circuit voltage can be determined by either discharging the battery at low discharge rates thus eliminating polarization or diffusion effects or by using pulse excitation such as the Galvanostatic Intermittent Titration Technique (GITT) explained in [94]. This method is mostly used to measure diffusion coefficients or ion mobility. On the other hand with this method the electrode potentials can be determined under load and in currentless state at the same time at different state of charges thus allowing a pointwise measurement of the OCV because after each excitation pulse the battery is returning to the equilibrium as is shown in fig. 5.3. During the pulse the charge

$$q \;=\; \int_{t_0}^{t_0+\tau} i\mathrm{d}t = I_0\tau \tag{5.1}$$

is transferred into the battery leading to a different state of charge after each pulse. Figures 5.4 and 5.5 show the OCV versus normalized lithium concentration for a graphite and and iron phosphate electrode based on a C/100 discharge provided by the *K2 Competence Center Virtual Vehicle*.

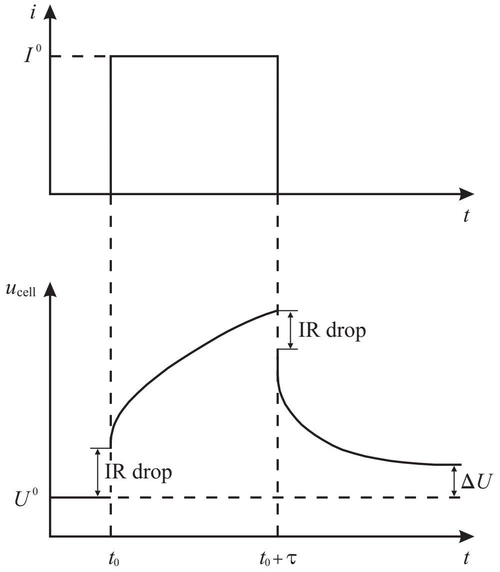

Figure 5.3.: GITT pulse with period τ and voltage response of a battery according to [94]. After each pulse the battery is returning to the equilibrium with the SOC being changed by $I_0\tau$ leading to the new OCV value $U_0 + \Delta U$.

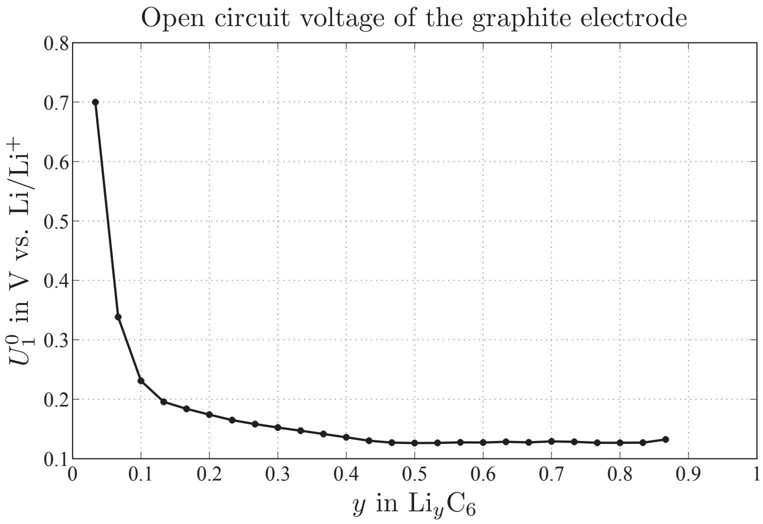

Figure 5.4.: Measured open circuit voltage for the graphite electrode versus normalized lithium concentration.

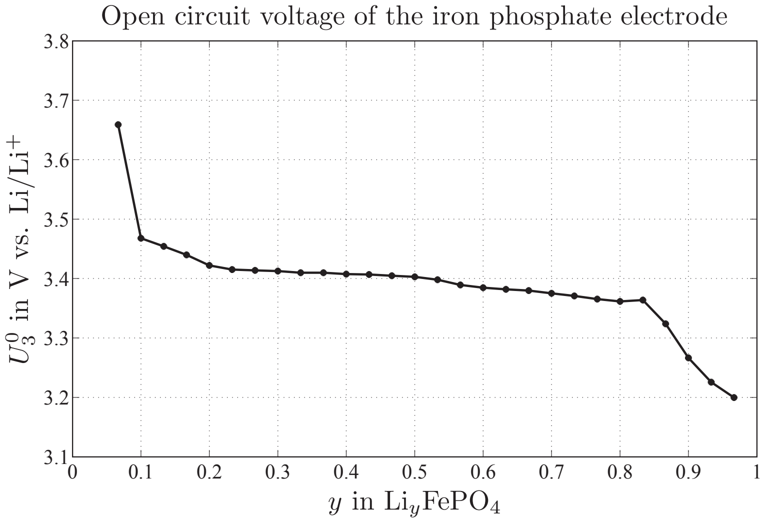

Figure 5.5.: Measured open circuit voltage for the iron phosphate electrode versus normalized lithium concentration.

Since the OCV in the extreme regions 0 and 1 is hard to access, to ensure that the cut-off voltages are reached, the OCV curves have to be slightly modified. Thus in the critical regions at the boundaries additional points are introduced before the OCV curves are incorporated into the model. Further, hysteresis effects of iron phosphate as reported e.g. in [30] are not considered in the model.

5.1.2. Validation of the Battery Model in the Time Domain

For the validation of the battery model each simulation is started at a common SOC of 0.5. Before each test a common procedure is carried out to obtain a basis of comparison between simulation and measurement. Therefore, the battery is charged to an upper limit of 3.8 V. Afterwards the discharge capacity at 1 C is determined by a discharge of the battery to the lower cut-off voltage of 2.5 V. The obtained value is taken as new cell capacity on the basis of which the charge/discharge current for the upcoming test procedure is calculated. Finally, the cell is charged to the upper cut-off voltage of 3.8 V again.

In the following the simulation results for a test matrix containing constant current as well as dynamic operating conditions are compared to measurements at three different temperatures 10°C, 30°C and 50°C. The presented test procedure has been defined in the 'COMET K2 project: *Modellierung, Validierung und Test von Lithium-Ionen-Batterien für Hybridfahrzeuge*'.

Test A – rate test

In the first test the long term behavior of the cell is investigated. Therefore, the cell runs through a series of charge and discharge sequences between the upper and lower cut-off voltages at 3.8 V and 2.5 V at C-rates [0.2, 0.5, 1, 2, 5] in ascending order. To avoid cell aging due to lithium plating by charging the battery at low temperatures at high C-rates the 2 C and 5 C sequences are skipped for 10°C. To compensate the dispersive capacities of the measurement cells among each other and for a better comparison to the simulated data a normalization is required. Therefore, a correction of the measurement and simulation data is made on the basis of the 1 C discharge sequence such that the 1 C discharge lasts exactly the expected 3600 s. Figure 5.6, 5.7 and 5.8 show the comparison between simulated (dashed line) and measured (solid lines) cell voltage for the rate test at 10°C, 30°C and 50°C. Furthermore, in fig. 5.9 a comparison between the relative cell voltage error at the different temperatures is given. Especially for the C-rates 0.2, 0.5 and 1 the charge and discharge behavior at 30°C and 50°C depicted in fig. 5.7 and 5.8 can be reproduced quite well. Nevertheless, for the C-rates 2 C and 5 C the shape of the cell voltage for the charge sequence starts to differ from the measurements resulting in an increasing error for charging the cell at higher C-rates. The simulated cell voltage at 10°C in fig. 5.6 shows a considerable offset to the measurements as a result from a too small inner resistance. Thus, with the actual set of equations with the temperature influence only being in-

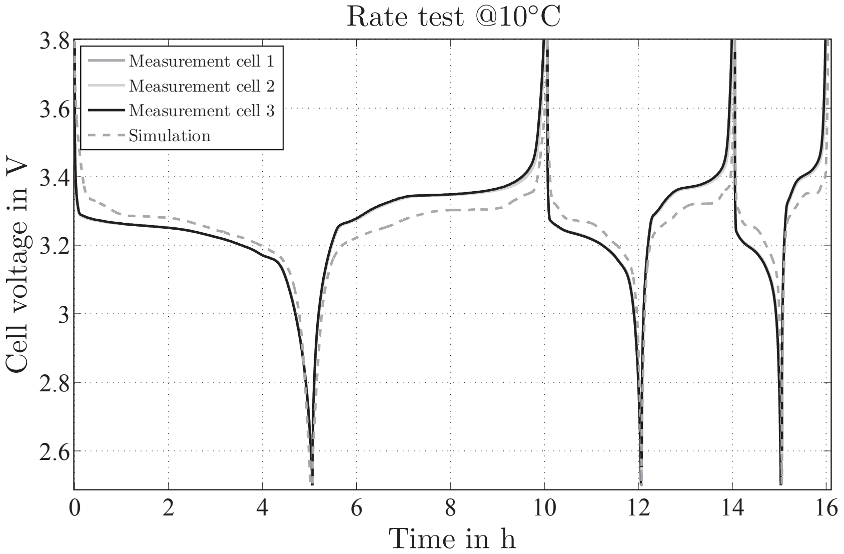

Figure 5.6.: Comparison of the simulated (dashed line) to the measured (solid lines) cell voltage for a charge/discharge sequence at C-rates [0.2, 0.5, 1] at 10°C. To avoid cell aging due to lithium plating the measurements at 2 C and 5 C are skipped.

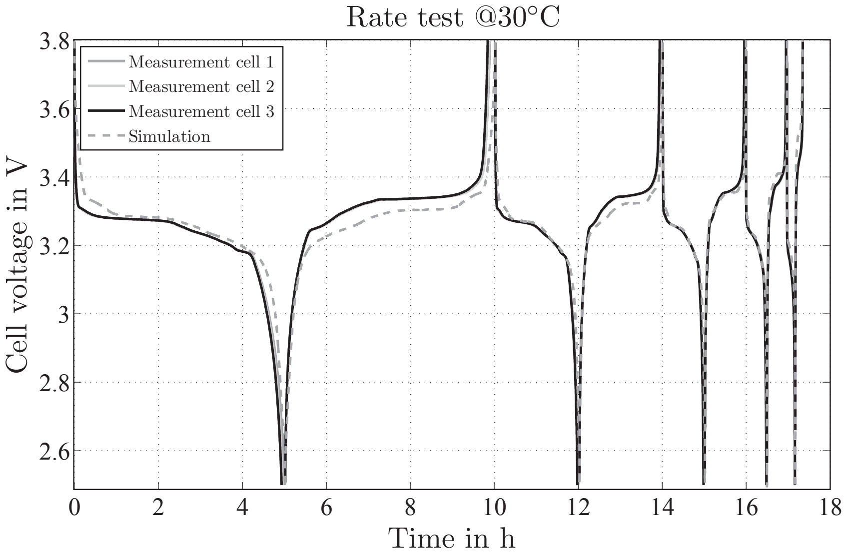

Figure 5.7.: Comparison of the simulated (dashed line) to the measured (solid lines) cell voltage for a charge/discharge sequence at C-rates [0.2, 0.5, 1, 2, 5] at 30°C.

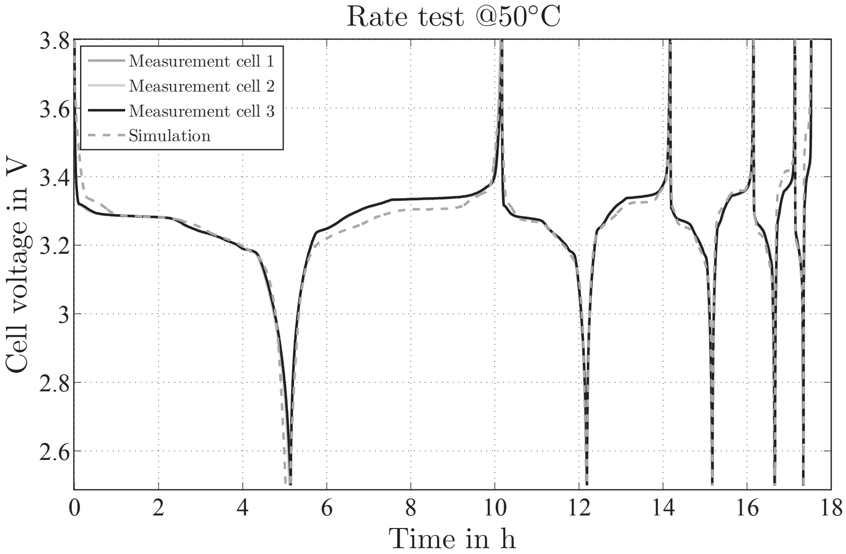

Figure 5.8.: Comparison of the simulated (dashed line) to the measured (solid lines) cell voltage for a charge/discharge sequence at C-rates [0.2, 0.5, 1, 2, 5] at 50°C.

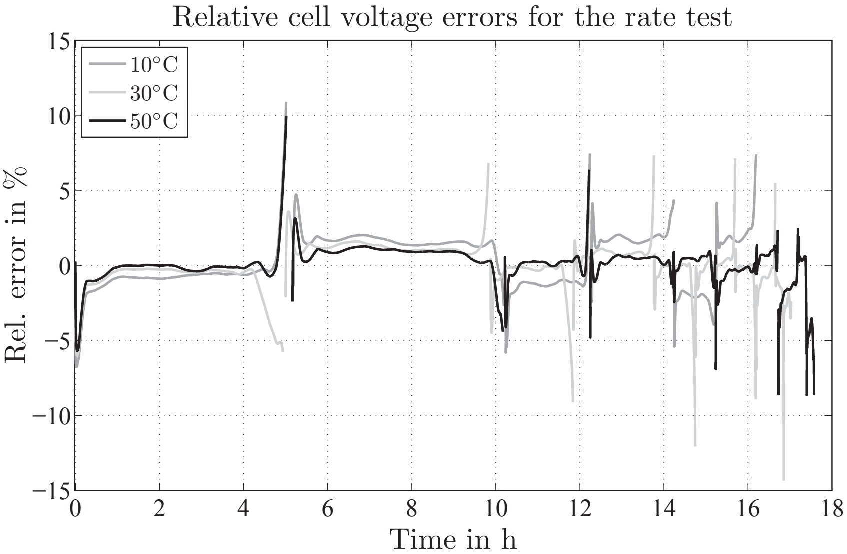

Figure 5.9.: Relative error of the cell voltage for the rate test consisting of a charge/discharge sequences at C-rates [0.2, 0.5, 1, 2, 5] at temperatures 10°C, 30°C and 50°C.

tegrated in the Butler-Volmer equation the rise of the inner resistance at lower temperatures can not be reproduced correctly. However, the deviation in reaching the upper and lower cut-off voltage at all C-rates is very low for all three temperatures applying the normalization to the 1 C discharge. The model gives a good estimate for the achievable charge/discharge capacity of each sequence. Therefore, in general the model allows to reproduce the long term behavior of the cell quite well with the relative error depicted in fig. 5.9 remaining mostly below 2.5 % except for the regions near the fully charged/discharged state of the battery.

Test B – pulse test

In the second test the dynamic behavior of the cell is investigated. Therefore, a dynamic test pattern consisting of charge/discharge pulses of length 1 s, 7 s and 49 s with increasing amplitudes of 0.5 C, 1 C and 5 C and a pause of 300 s between the different pulse lengths is run through. Again, to avoid lithium plating during charge, the 5 C pulses are skipped for the test at 10°C. To be able to observe the influence of the SOC on the cell response the test pattern is repeated at SOC = [0.8, 0.5, 0.2]. The simulated (dashed line) and measured (solid lines) voltage response to the entire

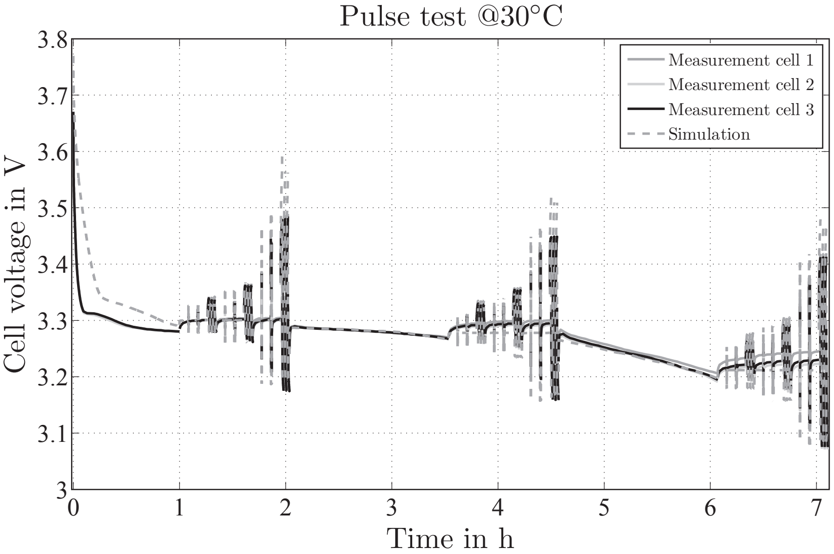

Figure 5.10.: Comparison between simulation (dashed line) and measurement (solid lines) at 30°C for the pulse test. The test pattern is composed of pulses of length 1 s, 7 s and 49 s with amplitudes of 0.5 C and 1 C and a pause of 300 s between the different pulse lengths. The sequence is run through at SOC = [0.8, 0.5, 0.2].

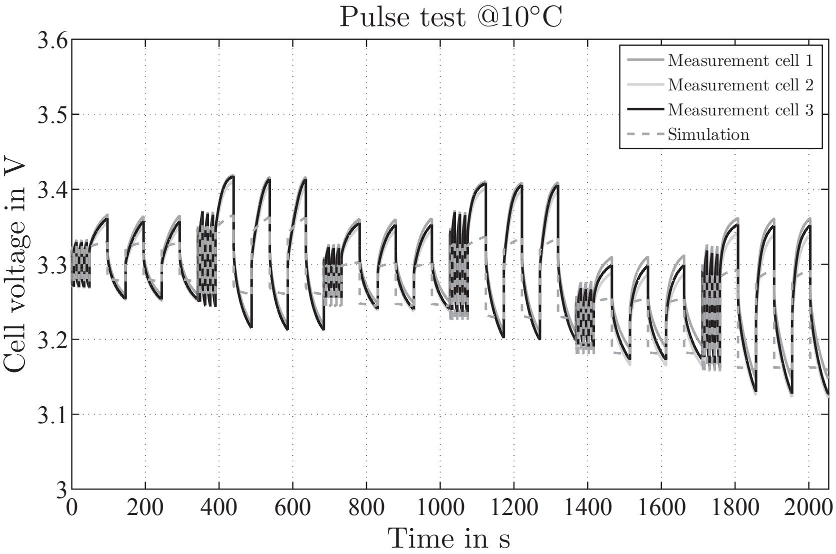

Figure 5.11.: Comparison between simulation (dashed line) and measurement (solid lines) at 10°C using pulse excitation. The test pattern is composed of pulses of length 1 s, 7 s and 49 s with amplitudes of 0.5 C and 1 C and is run through at SOC = [0.8, 0.5, 0.2]. The sequences between the pulses have been cut out. Again the 5 C current is skipped for 10°C.

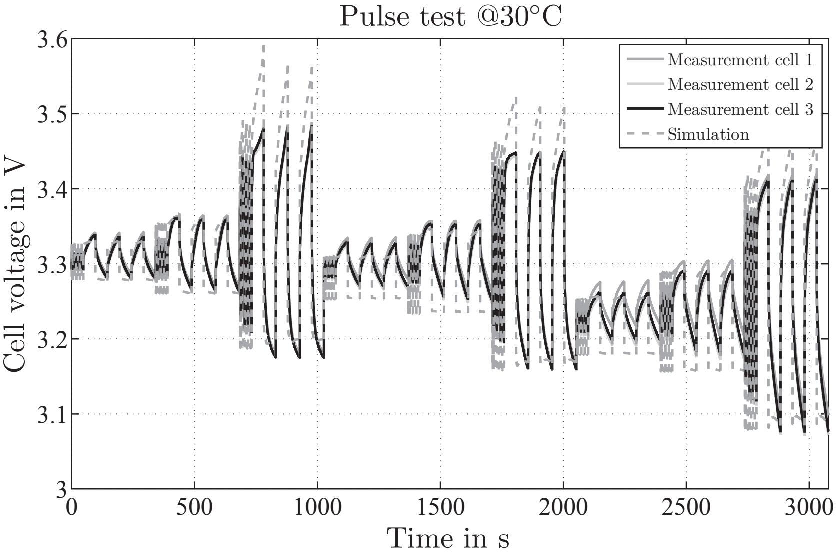

Figure 5.12.: Comparison between simulation (dashed line) and measurement (solid lines) at 30°C using pulse excitation. The test pattern is composed of pulses of length 1 s, 7 s and 49 s with amplitudes of 0.5 C, 1 C and 5 C and is run through at SOC = [0.8, 0.5, 0.2]. The sequences between the pulses have been cut out.

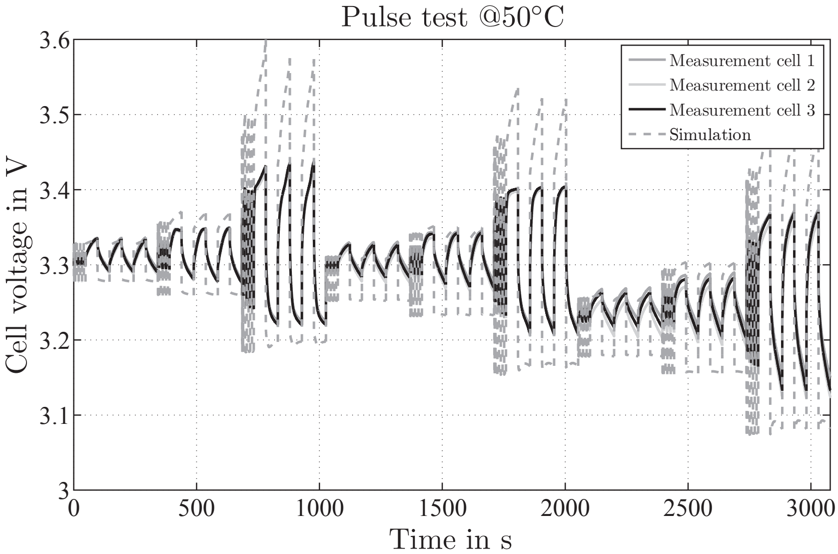

Figure 5.13.: Comparison between simulation (dashed line) and measurement (solid lines) at 50°C using pulse excitation. The test pattern is composed of pulses of length 1 s, 7 s and 49 s with amplitudes of 0.5 C, 1 C and 5 C and is run through at SOC = [0.8, 0.5, 0.2]. The sequences between the pulses have been cut out.

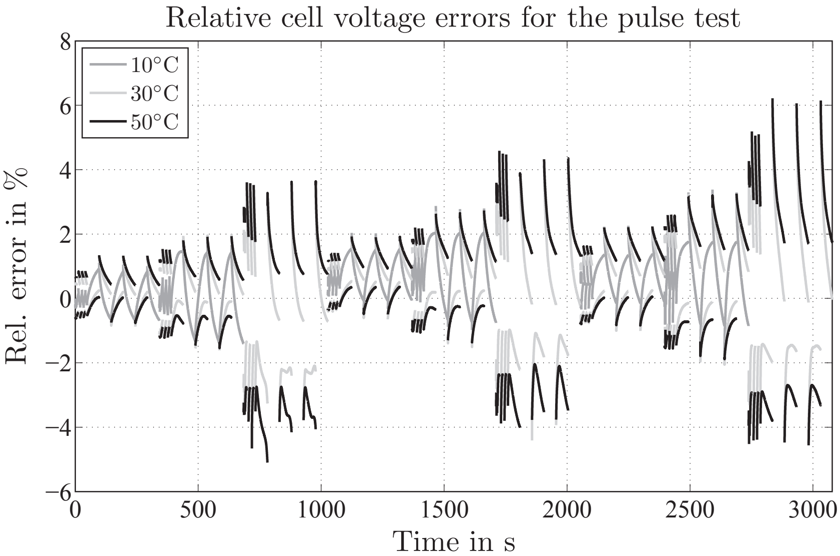

Figure 5.14.: Relative error of the cell voltage for the pulse test consisting of a sequence of pulses of length 1 s, 7 s and 49 s with amplitudes of 0.5 C, 1 C and 5 C and is run through at SOC = [0.8, 0.5, 0.2] at temperatures 10°C, 30°C and 50°C. The sequences between the pulses have been cut out.

test pattern at 30°C is depicted in fig. 5.10. For a better comparison in fig. 5.11, 5.12 and 5.13, showing the simulated (dashed line) and measured (solid lines) cell voltage at 10°C, 30°C and 50°C, the sequences between the pulses have been cut out because in this test only the shape of the pulses is of interest. Furthermore, in fig. 5.14 a comparison between the relative cell voltage error at the different temperatures is given. In contrast to the measurement in the simulation a distinct difference in the voltage response of the cell for the charge and discharge pulse is visible. Whereas for the charge pulse a similar voltage response is obtained for the discharge pulse the voltage is following the excitation too fast. Again the temperature influence can not be reproduced correctly. Therefore, for the test at 10°C depicted in fig. 5.11 the pulse height is slightly underestimated whereas for the test at 50°C shown in fig. 5.13 the pulse height is slightly overestimated. Especially for the 0.5 C and 1 C pulses at 30°C in fig. 5.12 the simulation correlates quite well to the measurements. The cell voltage is not drifting away in the simulation for all three temperatures and there is also only a small offset visible at $\mathrm{SOC} = 0.5$ and $\mathrm{SOC} = 0.2$. Although the maximum relative error is ~ 6 % in fig. 5.14 the error in the shape of the pulses is clearly visible.

Test C – pulse test with overlay

In the third test a combined load spectrum is designed since so far the long term behavior and the cell response to pulse excitation have only been dealt with separately. Thereby allowing a better insight of the influence of the SOC on the pulse behavior. The implemented test pattern consists of pulses of length 1 s, 7 s, and 49 s with pulse heights of 0.5 C and 1 C with an overlay of a 1 C constant current charge/discharge and increasing pulse length for each charge/discharge cycle. The simulated (dashed line) and measured (solid lines) voltage response to the entire test pattern at 30°C is given in fig. 5.15. For a better comparison in fig. 5.16, 5.17 and 5.18, showing the simulated (dashed line) and measured (solid lines) cell voltage at 10°, 30° and 50°, the sequences between the pulses have been cut out since as before the focus of this test is on the shape of the pulses. Furthermore, in fig. 5.19 a comparison between the relative cell voltage error at the different temperatures is given. Especially for the overlay with the 1 C discharge current at 30° C depicted in fig. 5.17 the simulation correlates quite well to the measurements. On the other hand at all three temperatures in the simulation an increased pulse height is observed during the charge overlay compared to the discharge overlay. Additionally, as expected the same temperature influence on the simulation as for the previous tests is obtained.

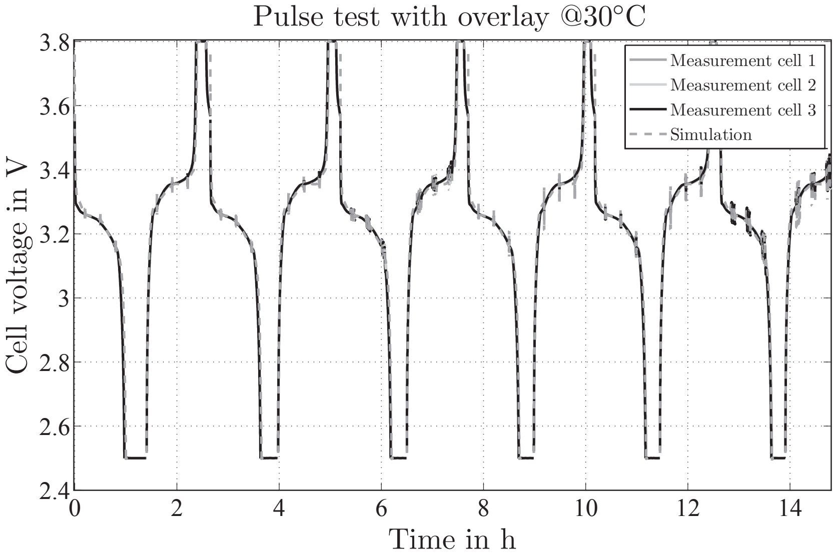

Figure 5.15.: Comparison between simulation (dashed line) and measurement (solid lines) at 30°C for the pulse test with overlay. The test pattern is composed of pulses of length 1 s, 7 s and 49 s with amplitudes of 0.5 C and 1 C overlaid with a 1 C current. The sequence is run through at SOC = [0.8, 0.5, 0.2].

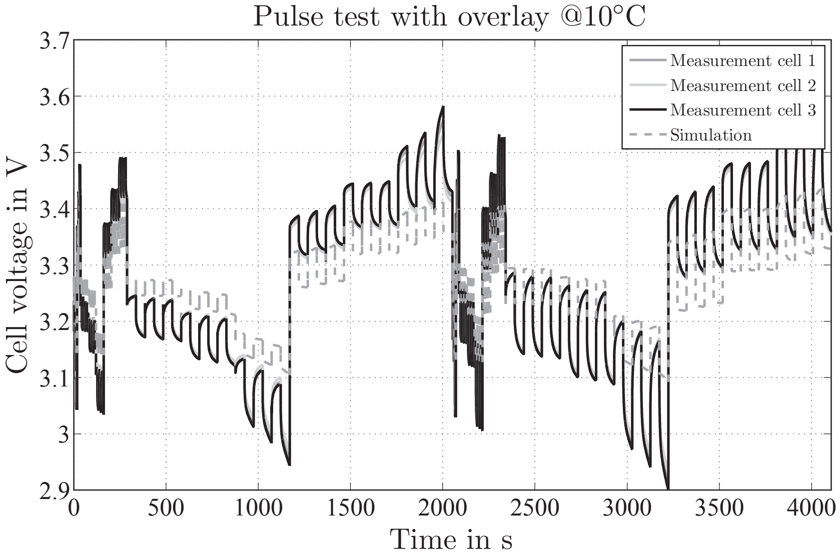

Figure 5.16.: Comparison between simulation (dashed line) and measurement (solid lines) at 10°C using pulse excitation overlaid with a 1 C current. The dynamic part of the test pattern is composed of pulses of length 1 s, 7 s and 49 s with amplitudes of 0.5 C and 1 C and is run through at SOC = [0.8, 0.5, 0.2]. The sequences between the pulses were cut out.

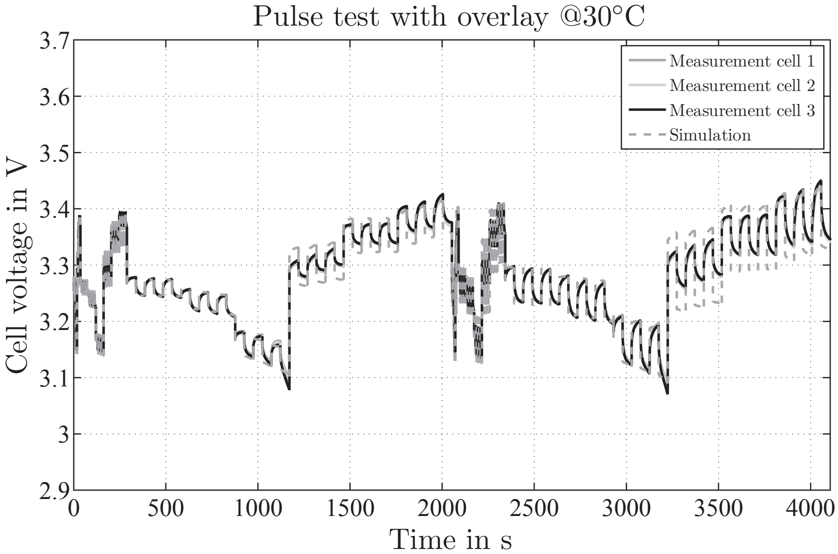

Figure 5.17.: Comparison between simulation (dashed line) and measurement (solid lines) at 30°C using pulse excitation overlaid with a 1 C current. The dynamic part of the test pattern is composed of pulses of length 1 s, 7 s and 49 s with amplitudes of 0.5 C and 1 C and is run through at SOC = [0.8, 0.5, 0.2]. The sequences between the pulses were cut out.

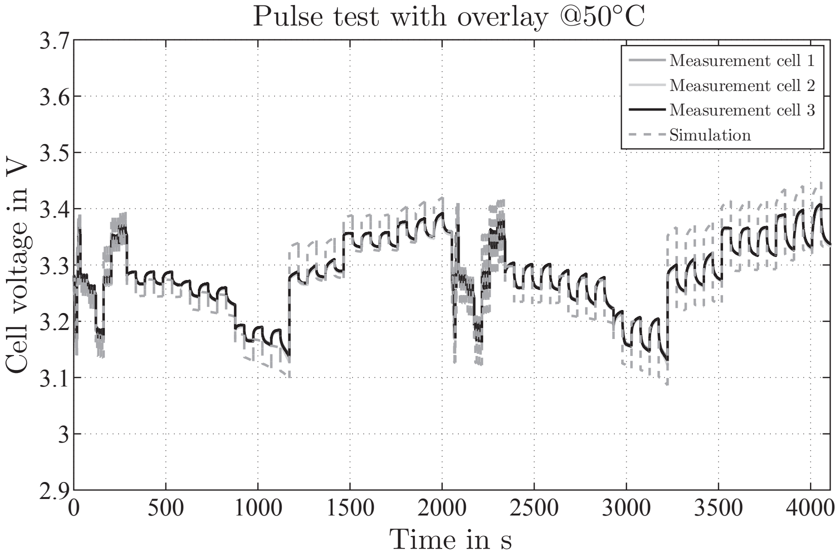

Figure 5.18.: Comparison between simulation (dashed line) and measurement (solid lines) at 10°C using pulse excitation overlaid with a 1 C current. The dynamic part of the test pattern is composed of pulses of length 1 s, 7 s and 49 s with amplitudes of 0.5 C and 1 C and is run through at SOC = [0.8, 0.5, 0.2]. The sequences between the pulses were cut out.

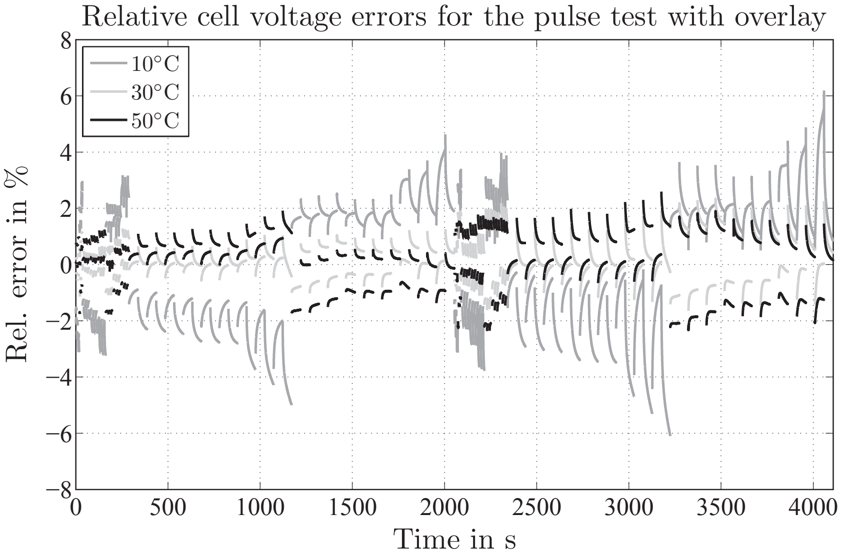

Figure 5.19.: Relative error of the cell voltage for the pulse test consisting of a sequence of pulses of length 1 s, 7 s and 49 s with amplitudes of 0.5 C, 1 C and 5 C overlaid with a 1 C current and is run through at SOC = [0.8, 0.5, 0.2] at temperatures 10°C, 30°C and 50°C. The sequences between the pulses have been cut out.

The simulation at 10° C in fig. 5.16 has also a small offset to the measurements. A difference in the pulse heights is obtained between measurement and simulation with an undersized pulse height at 10° C and an oversized pulse height at 50° C. Same as for the previous test as depicted in fig. 5.19 the problem is again the shape of the pulses with the maximum relative error being ∼ 6 % as well.

Test D – NEDC test

In the fourth test the usability of the battery model for automotive applications is investigated. Therefore, a current profile is derived for the simulation on the basis of the *New European Driving Cycle* (NEDC) [2] with the battery being discharged during acceleration and charged during deceleration due to recuperation. The data for the current profile have been provided within the 'COMET K2 project: *Modellierung, Validierung und Test von Lithium-Ionen-Batterien für Hybridfahrzeuge*'. Figure 5.20, 5.21 and 5.22 show the comparison between simulated (dashed line) and measured (solid lines) cell voltage for the NEDC at 10°C, 30°C and 50°C starting at SOC = 0.5. The maximum load current has been limited to 5 C. Further, in fig. 5.23 a comparison between the relative cell voltage error at the different temperatures is

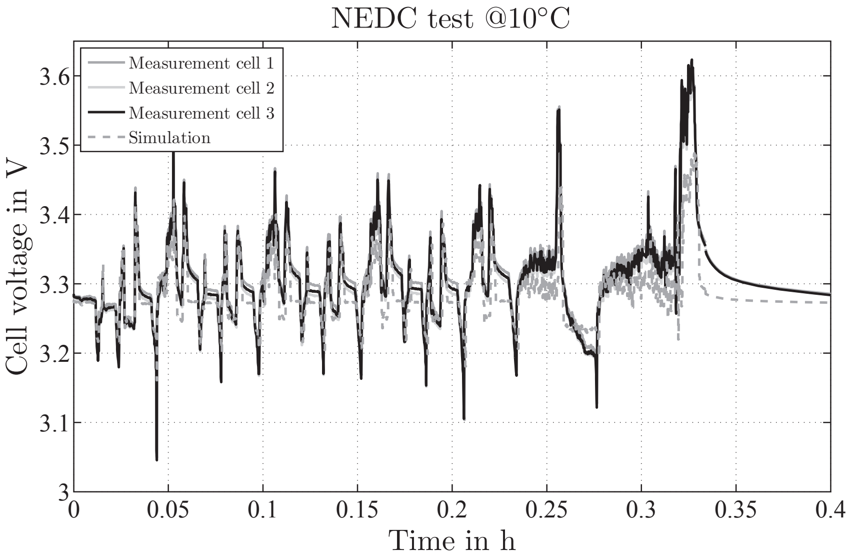

Figure 5.20.: Comparison between simulation (dashed line) and measurement (solid lines) for a current profile based on the NEDC by discharging the cell during acceleration as well as recuperative charging during deceleration starting at SOC = 0.5 at 10°C. The cell current has been limited to 5 C.

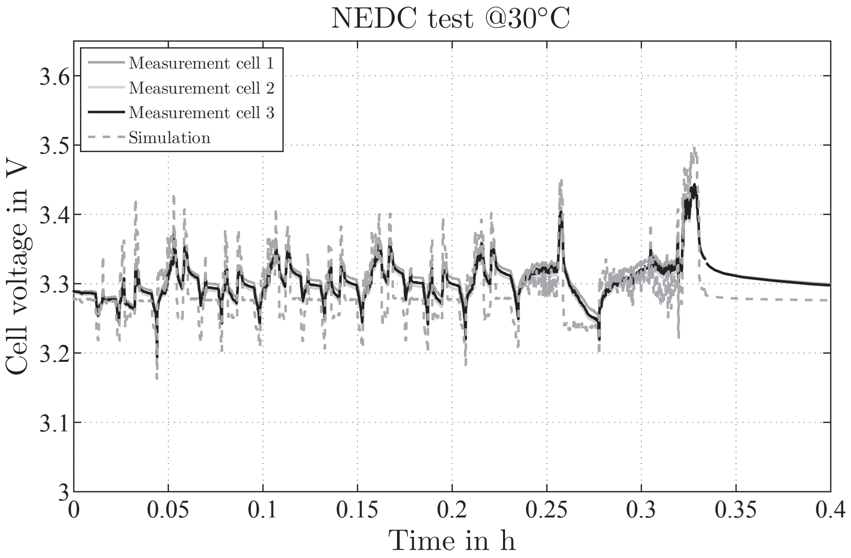

Figure 5.21.: Comparison between simulation (dashed line) and measurement (solid lines) for a current profile based on the NEDC by discharging the cell during acceleration as well as recuperative charging during deceleration starting at SOC = 0.5 at 30°C. The cell current has been limited to 5 C.

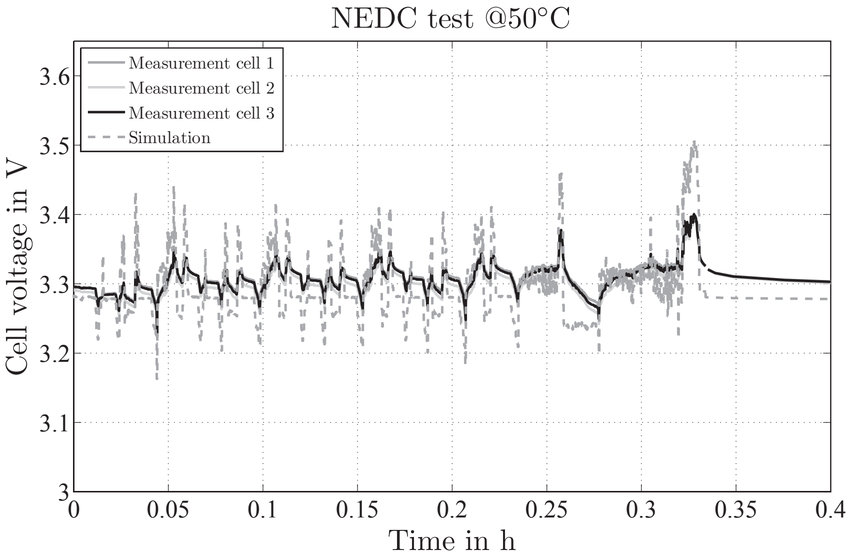

Figure 5.22.: Comparison between simulation (dashed line) and measurement (solid lines) for a current profile based on the NEDC by discharging the cell during acceleration as well as recuperative charging during deceleration starting at SOC = 0.5 at 50°C. The cell current has been limited to 5 C.

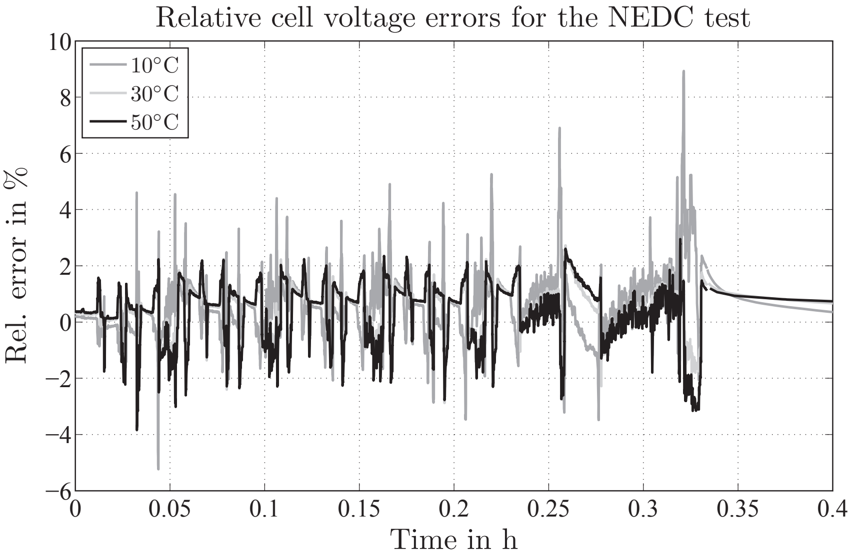

Figure 5.23.: Relative error of the cell voltage for a current profile based on the NEDC by discharging the cell during acceleration as well as recuperative charging during deceleration starting at SOC = 0.5 at temperatures 10°C, 30°C and 50°C. The cell current has been limited to 5 C.

given. In the measurements the temperature difference is clearly visible whereas in the simulation only a small difference in the cell voltage at the different temperatures can be observed. The displacement in the simulated cell voltage is too small for the simulation at 10°C depicted in fig. 5.20. On the other hand for the simulations at 30°C and 50°C shown in fig. 5.21 and 5.22 the displacement of the cell voltage is too big. Additionally, similar to the previous tests, in the simulation the cell voltage responds too fast to a change in the input current resulting in a nearly rectangular shape of the overall voltage profile. This behavior is clearly visible at the transition from the NEDC stress pattern to a constant current discharge at 0.2 C at the end of the simulation. But as can be seen in fig. 5.23 the relative error still remains < 10 %.

Regarding the calculation speed of the single tests depending on the test pattern and temperature a ratio between measurement and simulation time $t_{\mathrm{meas}}/t_{\mathrm{sim}}$ up to 50 can be reached.

Since the remaining error in the cell response to pulse excitation could not be eliminated by changing the model parameters and to identify the source of the deviation between measurement and simulation in the upcoming section the analysis of the cell is extended to the frequency domain.

5.2. Measurements on the 50 mAh Test Cell in the Frequency Domain

A deeper insight into the dynamical behavior of the lithium battery is required to be able to overcome the limitations of the model for pulse excitation. Therefore, in this section the cell impedance is analyzed using impedance spectroscopy (IS). Although this method is based on a small signal analysis of the current-voltage behavior at a single SOC, as stated in [7], it has the advantage that electrochemical reactions as well as diffusion processes within the battery can be assigned to a dedicated frequency range in the spectrum. Thus, the limiting factor in the voltage response during pulse excitation can be identified.

The measurements have been performed on a test bench consisting of a combined Potentiostat/Galvanostat 1287A and an Impedance/Gain-Phase Analyzer 1260A from Solartron[4] located at the Institute of Physical Chemistry (IPC), University of Muenster. As for the time domain measurements the data handling for the compari-

---

[4] http://www.solartronanalytical.com/

son between measurement and simulation is performed with the software package MATLAB®. The routine for the simulation of the impedance spectrum has been developed in cooperation with the *K2 Competence Center Virtual Vehicle*.

5.2.1. Validation of the Battery Model in the Frequency Domain

For the validation of the battery model in the frequency domain the simulation is again started at SOC = 0.5 and charged to the upper cut-off voltage of 3.8 V. In contrast to the time domain measurements the battery is charged from the lower cut-off voltage to the desired SOC directly after the determination of the cell capacity. The spectrum itself is obtained by driving the cell with a small sinusoidal current at different frequencies such that the voltage deviation does not exceed a peak to peak voltage of 50 mV. To ensure that the cell is operating at steady state three full periods are simulated at each frequency with the impedance being calculated for the last one.

Consistency Check of Measurement Data

In advance to the comparison to the simulated data the validity of the measured data has to be checked. Therefore, according to [14] and [87] to meet the requirements of causality, linearity, stability and stationarity the Kramers-Kronig transformations

$$\begin{aligned} Z_{Im}(\omega) &= \frac{2\omega}{\pi}\int\limits_0^\infty \frac{Z_{Re}(x) - Z_{Re}(\omega)}{x^2 - \omega^2}\mathrm{d}x \\ Z_{Re}(\omega) &= \frac{2}{\pi}\int\limits_0^\infty \frac{xZ_{Im}(x) - \omega Z_{Im}(\omega)}{x^2 - \omega^2}\mathrm{d}x \end{aligned} \tag{5.2}$$

relating the real and imaginary part of the impedance data have to be fulfilled. Since for measurement data the integrals in equ. 5.2 can not be solved an alternate approach based on RC-elements as in [14] and [87] is used. Therefore, with a single RC-element fulfilling the requirements in equ. 5.2 a series of these elements

$$Z_{kk} = R_\infty + \sum_{i=1}^{k} \frac{R_i}{\frac{j\omega}{\omega_{g,i}} + 1}, \quad \omega_{g,i} = \frac{1}{R_i C_i} \tag{5.3}$$

fitted to the measured impedance has to fulfill them too. The validation of the measurement data can be performed by evaluating the residuals between Z_{kk} in equ. 5.3 and the measurement data. On the basis of the described principle the data points at 100 Hz and 200 Hz have been identified as outliers in the measurements and thus been eliminated.

In fig. 5.24 and 5.25 the measured and simulated impedance spectra of the cell are depicted. The results between measurement and simulation in the frequency domain show distinct differences since the model has been parameterized on the basis of measurements in the time domain. Therefore, the diameter of the semicircle is clearly overestimated in the simulation whereas the cut-off frequency is underestimated. Further, in the measurements the center of the semicircle does not fall together with the real axis as is the case in the simulation. As has been observed by [71] for simulations of a lead-acid battery the behavior of the battery especially at low frequencies can not be reproduced correctly with an electrochemical model. In the simulation a constant real part of the cell impedance is obtained at frequencies below 1 Hz in contrast to the measurements where the beginning of a large semi-circle can be observed. In the following this low-frequency effect known as *Diffusion* or *Warburg Impedance* is further investigated since this is the frequency range relevant for the pulse lengths > 1 s used for the previous analysis of the dynamic behavior.

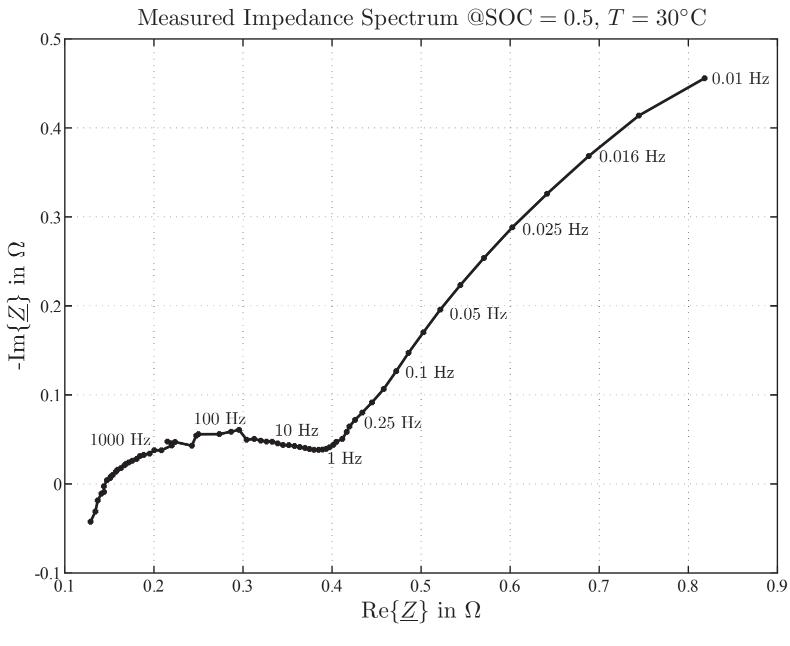
Measured Impedance Spectrum @SOC = 0.5, $T = 30°\mathrm{C}$

Figure 5.24.: Measured impedance spectrum of the 50 mAh pouchbag cell.

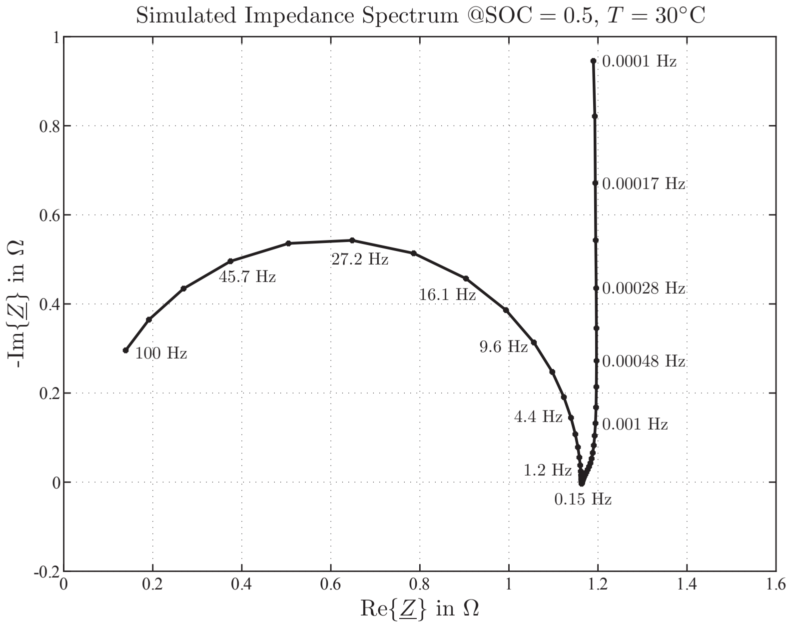

Figure 5.25.: Simulated impedance spectrum of the 50 mAh pouchbag cell.

The Warburg Impedance

As stated in [7] the *Warburg Impedance* can be regarded as the electrical analogue to diffusion processes in absence of migration by an equivalent circuit. Thus, in the first place the diffusion equation represented by Fick's 2nd law given e.g. in [6] and [37] has to be transformed in the frequency domain using the *Laplace Transformation* resulting in

$$sC(x) - c^0 \quad = \quad \nabla(D\nabla(C(x))) \tag{5.4}$$

with C being the transformed concentration denoted by the upper case letter and c^0 the concentration at $t = 0$. From the solution to the resulting ODE and inserting the transformed boundary condition at the electrode/electrolyte interface obtained from Fick's 1st law

$$J_W(0) \quad = \quad -DF\nabla(C(0)) \tag{5.5}$$

given e.g. in [6] and [37] the transfer behavior between the transformed input current density $J_W(0)$ and the transformed concentration $C(0)$ at the electrode surface can be derived with the upper case letters indicating a transformed variable. Further, to obtain the required impedance a relationship between the transformed ac overvoltage and the transformed concentration has to be found which, assuming only a small perturbation around the equilibrium, can be derived by a linearization of the diffusion overpotential represented by the *Nernst Equation* given e.g. in [6]. Depending on the boundary conditions three types of *Warburg Impedances* can be distinguished (see also [42] and [16]).

(i) semi-infinite diffusion layer:
$c = c_0$ for $x \to \infty$

$$Z_W = \frac{1}{c_0 f F \sqrt{2D}} \frac{1-j}{\sqrt{\omega}} = \sigma_W \frac{1-j}{\sqrt{\omega}} \tag{5.6}$$

(ii) limited diffusion layer with ideal reservoir at finite distance:
$c = c_0$ for $(x = l)$

$$Z_W = \frac{1}{c_0 f F} \frac{\tanh\left(l\sqrt{\frac{j\omega}{D}}\right)}{\sqrt{j\omega D}} \tag{5.7}$$

(iii) limited diffusion layer with non-permeable wall at finite distance:
$j_d = -DF\partial c/\partial x$ for $(x = l)$

$$Z_W = \frac{1}{c_0 f F} \frac{\coth\left(l\sqrt{\frac{j\omega}{D}}\right)}{\sqrt{j\omega D}} \tag{5.8}$$

The related impedance distributions are depicted in fig. 5.26.

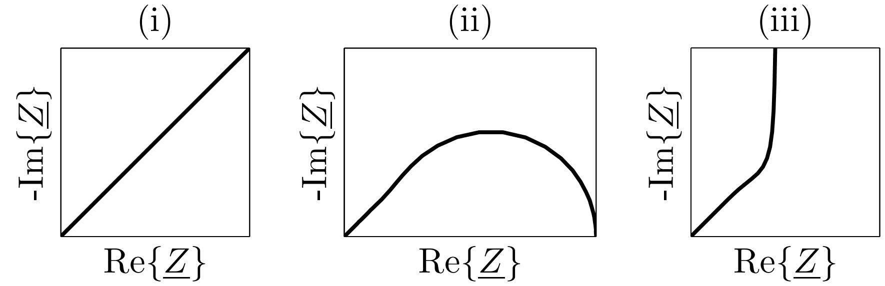

Figure 5.26.: Nyquist plots of different types of *Warburg Impedances*: (i) semi-infinite diffusion layer; (ii) limited diffusion layer with ideal reservoir; (iii) limited diffusion layer with non-permeable wall.

A more detailed analysis of the *Diffusion Impedance* dealing besides planar diffusion with diffusion in cylindrical and spherical symmetry as well is given in [39].

5.3. Simulation of a 70 Ah Lithium Polymer Cell based on Impedance Data

To show the influence of the cell impedance on the dynamic as well as the relaxation behavior of the battery in [72] an equivalent circuit model for a large-sized lithium polymer cell suitable for EV and HEV applications based on the Randles equivalent circuit [68] has been developed. Since for the used 70 Ah cell no measurements with a lithium reference are available in fig. 5.27 no distinction between the positive and negative electrode is made. Further, assuming limited diffusion with an ideal reservoir, the *Warburg Impedance* can be approximated with an additional RC-element as described in [3]. To be able to analyze the dynamic as well as the relaxation behavior simultaneously the 70 Ah cell is discharged by applying a series of 60 s discharge pulses at 3 C with a pause of 96 s in between. Comparing the simulated to the measured cell response at SOC $\approx$ 0.5 depicted in fig. 5.28 only minor differences in the cell response are visible. Although the results of the equivalent circuit model are in good agreement with the measurements and thus the origin of the deficiencies in the dynamic behavior obtained with the electrochemical model can be explained by the missing *Warburg Impedance* the remaining question on how to reproduce this behavior with the electrochemical model has not been solved yet, especially with not violating the demand of including no empirical terms without a clear physico-chemical background into the model.

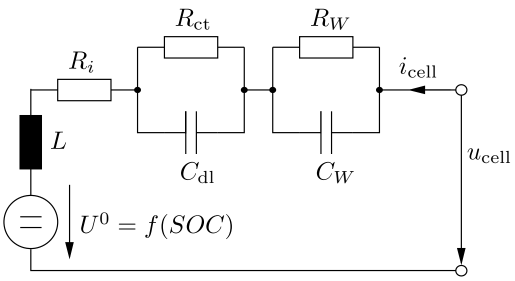

Figure 5.27.: Simple battery model based on the Randles equivalent circuit [68] of the electrode/electrolyte interface with the *Warburg Impedance* being approximated with an additional RC-element assuming limited diffusion with an ideal reservoir (from [72]).

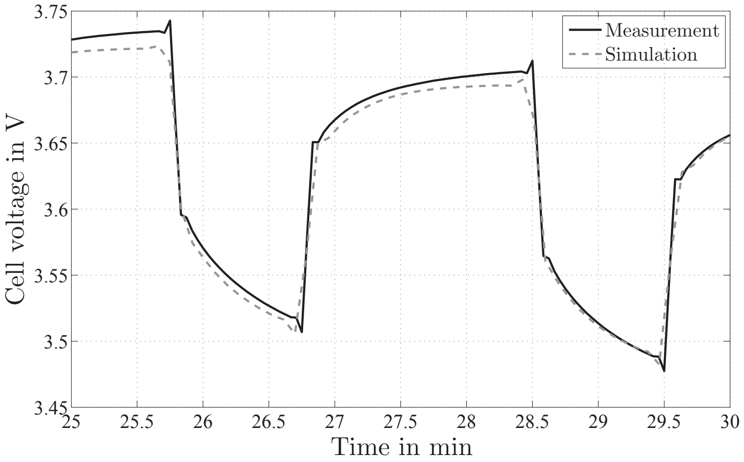

Figure 5.28.: Zoomed view of the voltage response of the cell to a series of 60 s discharge pulses at 3 C with a pause of 96 s in between at SOC ≈ 0.5 allowing a simultaneous investigation of the dynamic as well as the relaxation behavior (from [72]).

6. Conclusion & Outlook

As stated in chapter 1 the goal of this thesis has been the development of a fast and accurate battery model with respect to the comparison to measurable quantities such as the current-voltage behavior for battery condition monitoring with focus on automotive applications. Since for that purpose a deep insight into the electrochemical fundamentals and the underlying processes within the battery (chapter 2) is required a physico-chemical representation of the battery has been chosen as a promising candidate. In chapter 3 a set of coupled partial differential equations based on a review on modeling of lithium batteries given in [89] is presented with focus on reduction of the model complexity under consideration of the underlying physics of the battery as well as model accuracy. Thus, the geometry has been reduced into 1D with an additional coordinate for radial diffusion.

Chapter 4 deals with the numerical realization of the set of governing equations. Therefore, starting from a basic implementation of the model applying the control volume method, the model performance has been improved with respect to numerical stability using a modified Newton scheme and calculation speed introducing an adaptive time stepping routine. Further, a detailed analysis of the particle diffusion to reduce the number of discretization points in the bulk as well as the overall calculation effort and thus resulting in an performance increase of the model has been made at the end of the chapter considering both constant current as well as dynamic excitation of the battery.

The developed battery model is able to reproduce the long term behavior of the investigated cell quite well although some deficiencies of the model regarding the temperature behavior as well as in the voltage response to pulse excitation have been observed in chapter 5. Same as in [71] it is assumed that the deviations in the dynamic behavior are related to the missing *Diffusion* or *Warburg Impedance* occurring at low frequencies in the impedance spectrum. The question on how to reproduce this behavior with the set of governing equations has not been solved yet, especially not without violating the prerequisite for a pure physico-chemical representation. Despite the aforementioned small deviation of the cell response to pulse excitation the implemented battery model offers an acceptable accuracy level for battery condition monitoring systems fulfilling the additional requirements on calculation speed and robustness. Thus, the maximum relative error in the cell voltage in the investigated test cases is < 10 % and a ratio between measurement and simulation time $t_{\text{meas}}/t_{\text{sim}}$ up to 50 depending on the input current can be achieved.

Besides further investigations on improving the dynamic behavior of the model e.g. by following a combined electrochemical/equivalent circuit approach as proposed in [76] further extensions of the model regarding the thermal as well as the long term behavior are required which are both topics of ongoing research at the *K2 Competence Center Virtual Vehicle*. Thus, in a future work, temperature dependencies as well as parameter variations due to cell aging as well as concentration dependencies of diffusion within the battery have to be included into a reliable battery condition monitoring system. Applying model order reduction on the entire set of governing equations and thus sparing calculation time future work may also include an extension of the actual 1D model into a complete 3D representation with adequate model performance. Furthermore, the scalability of the model parametrized for the small 50 mAh pouch cell for large-sized pouch and cylindrical cells used in automotive applications has to be investigated.

A. List of Abbreviations

Short Symbols

symbol	description
CMS	condition monitoring system
CV	control volume
CVM	control volume method
FDM	finite difference method
GITT	galvanostatic intermittent titration technique
OCV	open circuit voltage
ODE	ordinary differential equation
Li	lithium
PCA	principal component analysis
PDE	partial differential equation
POD	proper orthogonal decomposition
SEI	solid electrolyte interface
SOC	state of charge
SVD	singular value decompostion

B. List of Symbols

Parameters

symbol	unit	description
A_{elec}	m^2	electrode face
a_j	m^2/m^3	'active' surface area per volume in region $j = \{1, 3\}$
α_j	-	transfer coefficient in region $j = \{1, 3\}$
brug_j	-	bruggeman coefficient in region $j = \{1, 3\}$
$C_{j,\text{dl}}$	F/m^2	double layer capacity in region $j = \{1, 3\}$
$c_{s,j}^{\text{min}}$	mol/m^3	minimum lithium concentration of particles in region $j = \{1, 3\}$
$c_{s,j}^{\text{ave}}$	mol/m^3	average lithium concentration of particles in region $j = \{1, 3\}$
$c_{s,j}^{\text{max}}$	mol/m^3	maximum lithium concentration of particles in region $j = \{1, 3\}$
$c_{s,j}^{0}$	mol/m^3	initial lithium concentration of particles in region $j = \{1, 3\}$
c_{ℓ}^{0}	mol/m^3	initial lithium concentration in the liquid phase
$D_{i,j}$	m^2/s	diffusion coefficient of species $i = \{s, \ell\}$ in region $j = \{1, 2, 3\}^*$
E	V/m	electrical field strength
$\varepsilon_{s,j}$	-	active material fraction in region $j = \{1, 3\}$
$\varepsilon_{\ell,j}$	-	porosity of region $j = \{1, 2, 3\}$

---

* note that there is no solid material in the separator region thus the index $\{s, 2\}$ is not possible

F	As/mol	Faraday constant
f	1/V	$\frac{F}{RT}$
i	A/m^2	charge/-discharge current density
i_0	A/m^2	exchange current density
j_j	A/m^2	transfer current density in region $j = \{1, 3\}$
$J_{i,j}$	mol/m^{2}s	electrochemical flux of species $i = \{s, \ell\}$ in region $j = \{1, 2, 3\}$
k_j	-	reaction rate in region $j = \{1, 3\}$
κ_j	S/m	conductivity of the liquid phase in region $j = \{1, 2, 3\}$
L_j	m	layer thickness of region $j = \{1, 2, 3\}$
$r_{p,j}$	m	mean particle radius in region $j = \{1, 3\}$
R	J/molK	gas constant
ρ	As/m^3	charge density
σ_j	S/m	conductivity of the solid phase in reg. $j = \{1, 3\}$
t_+^0	-	transition number
T	K	temperature
U_j^0	V	open circuit voltage in region $j = \{1, 3\}$

State Variables

symbol	unit	description
$c_{s,j}$	mol/m^3	lithium concentration of the solid phase in region $j = \{1, 3\}$
$c_{\ell,j}$	mol/m^3	lithium concentration of the liquid phase in region $j = \{1, 2, 3\}$
$\phi_{s,j}$	V	potential of the solid phase in region $j = \{1, 3\}$
$\phi_{\ell,j}$	V	potential of the liquid phase in region $j = \{1, 2, 3\}$

Mathematical Symbols

symbol	description
$\mathbf{a}$	vector
$\mathbf{A}$	matrix
$\mathrm{diag}\{\cdot\}$	diagonal matrix
$\mathrm{Im}\{\cdot\}$	imaginary part
$\mathrm{Re}\{\cdot\}$	real part
r_j	radial coordinate in the particle in region $j = \{1, 3\}$
t	time coordinate
x	spatial coordinate in direction of the main reaction
λ	eigenvalue
$\boldsymbol{\varphi}$	eigenvector
Ω_i	mathematical domain
$\partial\Omega_i$	domain boundary

Subscripts

symbol	description
1	negative electrode
2	separator
3	positive electrode
dl	double layer
s	solid phase
ℓ	liquid phase

Superscripts

symbol	description
0	initial value
ave	average value
eff	effective property
min	minimum value
max	maximum value
surf	surface value

Bibliography

[1] Battery Design LLC, Battery Design Studio®, `http://www.cd-adapco.com/products/battery_design_studio/index.html`. 3

[2] HYBRID-AUTOS.INFO, Driving Cycles, `http://www.hybrid-autos.info/en/erblick-verschiedener-fahrzyklen.html`. 79

[3] D. Andre, M. Meiler, K. Steiner, H. Walz, T. Soczka-Guth, and D. U. Sauer. Characterization of high-power lithium-ion batteries by electrochemical impedance spectroscopy. ii: Modelling. *Journal of Power Sources*, 196:5349–5356, 2011. 3, 87

[4] D. Aurbach. Review of selected electrode–solution interactions which determine the performance of `Li` and `Li` ion batteries. *Journal of Power Sources*, 89:206–218, 2000. 11

[5] P. B. Balbuena and Y. Wang, editors. *Lithium-Ion Batteries: Solid-electrolyte Interface*. Imperial College Press, 2004. 11

[6] A. J. Bard and L. R. Faulkner. *Electrochemical Methods - Fundamentals and Applications*. John Wiley & Sons, Inc., 2nd edition, 2001. 14, 15, 16, 17, 28, 29, 55, 85, 86

[7] E. Barsoukov and J. R. Macdonald, editors. *Impedance Spectroscopy - Theory, Experiment, and Applications*. John Wiley & Sons, Inc., 2nd edition, 2005. 82, 85

[8] K. Becker-Steinberger, S. Funken, M. Landstorfer, and K. Urban. A mathematical model forc all solid-state lithium ion batteries. *ECS Transactions*, 25(36):285–296, 2010. 3

[9] J. O. Besenhard, editor. *Handbook of Battery Materials*. WILEY-VCH Verlag GmbH & Co, 1999. 11

[10] J. O. Besenhard and M. Winter. Insertion reactions in advanced electrochemical energy storage. *Pure & Applied Chemistry*, 70(3):603–608, 1998. 7, 10

[11] I. Bloom, B. W. Cole, J. J. Sohn, S. A. Jones, E. G. Polzin, V. S. Battaglia, G. L. Henriksen, C. Motloch, R. Richardson, T. Unkelhaeuser, D. Ingersoll, and H. L. Case. An accelerated calendar and cycle life study of Li-ion cells. *Journal of Power Sources*, 101:238–247, 2001. 11

[12] H. G. Bock and K. J. Plitt. A multiple shooting algorithm for direct solution of optimal control problems. In *Proceedings of the 9th IFAC World Congress*, 1984. 47

[13] G. G. Botte, J. A. Ritter, and R. E. White. Comparison of finite difference and control volume methods for solving differential equations. *Computer & Chemical Engineering*, 24:2633–2654, 2000. 54

[14] B. A. Boukamp. Impedance spectroscopy, strength and limitations. *Technisches Messen*, 71(9):454–459, 2004. 83

[15] M. Broussely, S. Herreyre, P. Biensan, P. Kasztejna, K. Nechev, and R. J. Staniewicz. Aging mechanisms in Li ion cells and calendar life predictions. *Journal of Power Sources*, 97-98:13–21, 2001. 12

[16] S. Buller. *Impedance-Based Simulation Models for Energy Storage Devices in Advanced Automotive Power Systems.* Dissertation, RWTH Aachen University, Institute for Power Electronics and Electrical Drives, 2003. 2, 7, 86

[17] S. Buller, M. Thele, E. Karden, and R. W. D. Donker. Impedance-based non-linear dynamic battery modeling for automotive applications. *Journal of Power Sources*, 113:422–430, 2003. 3

[18] R. L. Burden and J. D. Faires. *Numerical Analysis.* PWS Publishers, 3rd edition, 1985. 50, 51

[19] L. Cai and R. E. White. Reduction of model order based on proper orthogonal decomposition for lithium-ion battery simulations. *Journal of The Electrochemical Society*, 156(3):A154–A161, 2009. 3, 53, 54, 59, 61

[20] H. A. Catherino, J. F. Burgel, A. Rusek, and F. Feres. Modelling and simulation of lead-acid battery charging. *Journal of Power Sources*, 80:17–20, 1999. 2

[21] C. Chan, E. Lo, and S. Weixiang. The available capacity computation model based on artificial neural network for leadacid batteries in electric vehicles. *Journal of Power Sources*, 87:201–204, 2000. 2

[22] F. Codec, S. M. Savaresi, and G. Rizzoni. On battery state of charge estimation: a new mixed algorithm. In *17th IEEE International Conference on Control Applications*, 2008. 3

[23] COMSOL. *1D Isothermal Lithium-Ion Battery,* `http://www.comsol.com/showroom/documentation/model/686/`. 3, 37

[24] D. Danilov and P. H. L. Notten. Mathematical modelling of ionic transport in the electrolyte of li-ion batteries. *Electrochimica Acta*, 53:5569–5578, 2008. 10

[25] J. E. Dennis, Jr. and R. B. Schnabel. *Numerical Methods for Unconstrained Optimization and Nonlinear Equations.* Prentice-Hall, Inc., 1996. 49

[26] P. Deuflhard and F. Bornemann. *Texts in Applied Mathematics 42: Scientific Computing with Ordinary Differential Equations.* Springer, 2002. 47

[27] M. Doyle, T. F. Fuller, and J. Newman. Modeling of galvanostatic charge and discharge of the lithium/polymer/insertion cell. *Journal of The Electrochemical Society*, 140(6):1526–1533, 1993. 3

[28] M. Doyle and J. Newman. Comparison of modeling predictions with experimental data from plastic lithium ion cells. *Journal of The Electrochemical Society*, 143(6):1890–1903, 1996. 3

[29] W. Dreyer, M. Gaberšček, C. Guhlke, R. Huth, and J. Jamnik. Phase transition in a rechargeable lithium battery. *European Journal of Applied Mathematics*, 22(3):267–290, 2011. 3

[30] W. Dreyer, C. Guhlke, and R. Huth. The behavior of a many-particle electrode in a lithium-ion battery. *Physica D: Nonlinear Phenomena*, 240(12):1008–1019, 2011. 3, 69

[31] EU WHITE PAPER. Roadmap to a single european transport area towards a competitive and resource efficient transport system, `http://eur-lex.europa.eu/LexUriServ/LexUriServ.do?uri=COM:2011:0144:FIN:EN:PDF`, 2011. 1

[32] T. F. Fuller, M. Doyle, and J. Newman. Simulation and optimization of the dual lithium ion insertion cell. *Journal of The Electrochemical Society*, 141(1):1–10, 1994. 3

[33] L. Gao, S. Liu, and R. A. Dougal. Dynamic lithium-ion battery model for system simulation. In *IEEE Transactions on Components and Packaging Technologies*, volume 25, pages 495–505, 2002. 3

[34] P. M. Gomadam, J. W. Weidner, R. A. Dougal, and R. E. White. Mathematical modeling of lithium-ion and nickel battery systems. *Journal of Power Sources*, 110:267–284, 2002. 21

[35] J. B. Goodenough, A. K. Padhi, K. S. Nanjundaswamy, and C. Masquelier. Cathode materials for secondary (rechargeable) lithium batteries, 1999. 6

[36] B. Haasdonk and M. Ohlberger. Reduced basis method for finite volume approximations of parametrized linear evolution equations. *ESIAM: Mathematical Modelling and Numerical Analysis*, 42:277–302, 2008. 59

[37] C. H. Hamann and W. Vielstich. *Elektrochemie.* WILEY-VCH Verlag GmbH & Co, 4th edition, 2005. 16, 17, 18, 85

[38] T. Handschuh. *Untersuchung des Betriebs- und Alterungsverhaltens von Blei-Säure-Akkumulatoren bei für Hybridantriebssysteme typischen Belastungen.* PhD thesis, Universität Ulm, Fakultät für Ingenieurwissenschaften und Informatik, 2007. 2

[39] T. Jacobsen and K. West. Diffusion impedance in planar, cylindrical and spherical symmetry. *Electrochimica Acta*, 40(2):255–262, 1995. 87

[40] M. R. Johan and A. K. Arof. Modeling of electrochemical intercalation of lithium into a $\mathrm{LiMn_2O_4}$ electrode using green function. *Journal of Power Sources*, 170:490–494, 2007. 32

[41] M. Jung and U. Langer. *Methode der finiten Elemente für Ingenieure: Eine Einführung in die numerischen Grundlagen und Computersimulation.* B.G. Teubner GmbH, 2001. 34, 44

[42] E. Karden. *Using low-frequency impedance spectroscopy for characteriza-tion, monitoring, and modeling of industrial batteries.* Dissertation, RWTH Aachen University, Fakultät für Elektrotechnik und Informationstechnik, 2001. 3, 86

[43] G.-H. Kim, A. Pesaran, and R. Spotnitz. A three-dimensional thermal abuse model for lithium-ion cells. *Journal of Power Sources*, 170:476–489, 2007. 20

[44] P. Knaber and L. Angermann. *Numerik partieller Differentialgleichungen: Eine anwendungsorientierte Einführung.* Springer, 2000. 32, 34, 37

[45] S. Koller and M. Schmuck. *Batteries and Supercapacitors*, Lecture Notes, Graz University of Technology, Institute for Chemistry and Technology of Materials, 2009. 9, 17

[46] J. Kowal, J. B. Gerschler, C. Schäper, T. Schoenen, and D. U. Sauer. Efficient battery models for the design of ev drive trains. In *14th International Power Electronics and Motion Control Conference, EPE-PEMC 2010*, 2010. 2, 3

[47] H. Kren. *About the Continuous Growth of the Solid Electrolyte Interphase in Lithium Ion Batteries.* PhD thesis, Graz University of Technology, Institute for Chemistry and Technology of Materials, 2011. 11, 13

[48] E. Kreyszig. *Advanced Engeneering Mathematics.* John Wiley & Sons, Inc., 1993. 51

[49] K. Kumaresan, G. Sikha, and R. E. White. Themal model for a Li-Ion cell. *Journal of The Electrochemical Society*, 155(2):A164–A171, 2008. 20

[50] K. Kunisch and S. Volkwein. Galerkin proper orthogonal decomposition methods for a general equation in fluid dynamics. *SIAM Journal on Numerical Analysis*, 40(2):492–515, 2002. 62

[51] K. Kunisch and S. Vollkwein. Galerkin proper orthogonal decomposition methods for parabolic problems. *Numerische Mathematik*, 90(1):117–148, 2001. 62

[52] O. Lass and S. Volkwein. POD Galerkin schemes for nonlinear elliptic-parabolic systems. submitted 2011, 2011. 60, 61

[53] A. Latz and J. Zausch. Thermodynamic consistent transport theory of li-ion batteries. Bericht 195, Fraunhofer ITWM, 2010. 3

[54] A. Latz, J. Zausch, and O. Iliev. Modeling of species and charge trans-port in li-ion batteries based on non-equilibrium thermodynamics. Bericht 191, Fraunhofer ITWM, 2010. 3

[55] R. J. LeVeque. *Finite Difference Methods for Ordinary and Partial Differential Equations - Steady State and Time-Dependent Problems.* Siam, 2007. 32, 33, 53

[56] D. Linden and T. B. Reddy, editors. *Handbook of Batteries.* McGraw-Hill, 3rd edition, 2002. 14, 15, 17

[57] S. Liu. An analytical solution to $\mathtt{Li}/\mathtt{Li}^+$ insertion into a porous electrode. *Solid State Ionics*, 177:53–58, 2006. 32

[58] J. P. Meyers, M. Doyle, R. M. Darling, and J. Newman. The impedance response of a porous electrode composed of intercalation particles. *Journal of the Electrochemical Society*, 147(8):2930–2940, 2000. 22

[59] S. E. Minkoff and N. M. Kridler. A comparison of adaptive time stepping methods for coupled flow and deformation modeling. *Applied mathematical modelling*, 30(9):993–1009, 2006. 51, 52

[60] C.-D. Munz and T. Westermann. *Numerische Behandlung gewöhnlicher und partieller Differentialgleichungen.* Springer, 2006. 32, 43

[61] J. Newman and K. E. Thomas-Alyea. *Electrochemical Systems.* John Wiley & Sons, Inc., 3rd edition, 2004. 20, 21, 22

[62] I. J. Ong and J. Newman. Double-layer capacitance in a dual lithium ion insertion cell. *Journal of the Electrochemical Society*, 146(12):4360–4365, 1999. 29

[63] P. E. Pascoe and A. H. Anbuky. A vrla battery simulation model. *Energy Conversion and Management*, 45:1015–1041, 2004. 2

[64] S. V. Patankar. *Numerical Heat Transfer and Fluid Flow.* Hemisphere Publishing Corperation, 1980. 40, 41, 42, 43

[65] E. Peled. The electrochemical behavior of alkali and alkaline earth metals in nonaqueous battery systems - the solid electrolyte interphase model. *Journal of the Electrochemical Society*, 126(12):2047–2051, 1979. 10

[66] H.-J. Pesch and P. Rentrop. Numerical solution of the flow between two-counter-rotating infinite plane discs by multiple shooting. *Journal of Aplied Mathematics and Mechanics ZAMM*, 58(1):23–28, 1978. 47

[67] P. Popov, Y. Vutov, S. Margenov, and O. Iliev. Finite volume discretization of equations describing nonlinear diffusion in li-ion batteries. Bericht 191, Fraunhofer ITWM, 2010. 37

[68] J. E. B. Randles. Kinetics of rapid electrode reactions. *Discussions Faraday Society*, 1:11–19, 1947. 87

[69] M. Y. Saïdi and J. Barker. The Safety Advantages of Valence's SAPHION® Technology. Technical report, Valence Technology, 2004. 6

[70] S. Santhanagopalan, Q. Zhang, K. Kumaresan, and R. E. White. Parameter estimation and life modeling of lithium-ion cells. *Journal of The Electrochemical Society*, 155(4):A345–A353, 2008. 12

[71] B. Schweighofer. *Simulation of the Dynamic Behavior of a Lead-Acid Battery.* Dissertation, Graz University of Technology, Institute of Electrical Measurement and Measurement Signal Processing, 2007. 20, 21, 40, 47, 48, 84, 89

[72] B. Schweighofer, H. Wegleiter, M. Sommer, and M. Recheis. Fast and accurate battery model applicable for system level simulation. In *European Electric Vehicle Congress EEVC 2011*, 2011. 4, 87, 88

[73] G. Sikha, R. E. White, and B. N. Popov. A mathematical model for a lithium-ion battery/electrochemical capacitor hybrid system. *Journal of The Electrochemical Society*, 152(8):A1682–A1693, 2005. 29

[74] P. Singh, J. Craig Fennie, and D. Reisner. Fuzzy logic modelling of state-of-charge and available capacity of nickel/metal hydride batteries. *Journal of Power Sources*, 136:322–333, 2004. 2

[75] L. Sirovich. Turbulence and the dynamics of coherent structures, parts i-iii. *Quaterly of Applied Mathematics*, XLV:561–590, 1987. 60

[76] K. Smith, C. D. Rahn, and C.-Y. Wang. Control oriented 1d electrochemical model of lithium ion battery. *Energy Conversion and Management*, 48:2565–2578, 2007. 90

[77] K. Smith and C.-Y. Wang. Power and thermal characterization of a lithium-ion battery pack for hybrid-electric verhicles. *Journal of Power Sources*, 160:662–673, 2006. 20, 22

[78] K. A. Smith, C. D. Rahn, and C.-Y. Wang. Model order reduction of 1D diffusion systems via residue grouping. *Journal of Dynamic Systems, Measurement and Control*, 130:011012.1–011012.8, 2008. 3, 54

[79] M. S. Sommer, D. Hrach, B. Schweighofer, and M. Cifrain. Fast algorithm for calculating the surface concentration of spherical particles for lithium-ion battery simulations. In *Procedia Engineering*, volume 5, pages 389–392, 2010. 4, 40, 53, 54, 56, 57

[80] M. S. Sommer and C. F. Wallinger. Reduction oft the calculation effort for the Li-diffusion in Li-ion battery modeling. In *Proceedings of the 14th International IGTE Symposium 2010*, 2010. 4, 53, 61

[81] R. Spotnitz. Simulation of capacity fade in lithium-ion batteries. *Journal of Power Sources*, 113:72–80, 2003. 11

[82] M. Sternad, M. Cifrain, D. Watzening, G. Brasseur, and M. Winter. Condition monitoring of lithium-ion batteries for electric and hybrid electric vehicles. *e & i Elektrotechnik und Informationstechnik*, 126(5):186–193, 2009. 2, 7

[83] A. Studinger and S. Volkwein. Numerical analysis of pod a-posteriori error estimation for optimal control. submitted 2011, 2011. 60

[84] The Newman Research Group. Fortran programs for the simulation of electrochemical systems, `http://www.cchem.berkeley.edu/jsngrp/`. 3

[85] I. V. Thorat, D. E. Stephenson, N. A. Zacharias, K. Zaghib, J. N. Harb, and D. R. Wheelera. Quantifying tortuosity in porous li-ion battery materials. *Journal of Power Sources*, 188:592–600, 2009. 23

[86] U. Tröltzsch. *Modellbasierte Zustandsdiagnose von Gerätebatterien.* Dissertation, Universität der Bundeswehr München, Fakultät für Elektrotechnik und Informationstechnik, 2005. 2

[87] U. Tröltzsch and O. Kanoun. Implementierung der Impedanzspektroskopie in vollautomatischen Messsystemen am beispiel der batteriezustandsdiagnose. *Technisches Messen*, 73(7-8):393–403, 2006. 83

[88] U. Tröltzsch, O. Kanoun, and H.-R. Tränkler. Characterizing aging effects of lithium ion batteries by impedance spectroscopy. *Electrochimica Acta*, 51:1664–1672, 2006. 3

[89] W. A. van Schalkwijk and B. Scrosati, editors. *Advances in Lithium-Ion Batteries*. Kluwer Academic Publishers, 2002. 5, 8, 9, 11, 20, 21, 25, 27, 29, 30, 31, 89

[90] J. Vetter, P. Novák, M. R. Wagner, C. Veit, K.-C. Möller, J. O. Besenhard, M. Winter, M. Wohlfahrt-Mehrens, C. Vogler, and A. Hammouche. Ageing mechanisms in lithium-ion batteries. *Journal of Power Sources*, 147:269–281, 2005. 12, 13

[91] S. Volkwein. *Model Reduction Using Proper Orthogonal Decomposition*, Lecture Notes, University of Konstanz, Department of Mathematics & Statistics, 2010. 60, 61

[92] X. Wang and K. Aoki. Transition of current of lithium intercalation from solution to graphite. *Journal of Electroanalytical Chemistry*, 64:101–108, 2007. 32

[93] D. Watzenig, M. S. Sommer, and G. Steiner. Engine state monitoring and fault diagnosis of large marine diesel engines. *e & i Elektrotechnik und Informationstechnik*, 126(5):173–179, 2009. 2, 5

[94] W. Weppner and R. A. Huggins. Electrochemical investigation of the chemical diffusion, partial ionic conductivities, and other kinetic parameters in Li_3Sb and Li_3Bi. *Journal of Solid State Chemistry*, 22:297–308, 1977. 68

[95] M. Winter, J. O. Besenhard, M. E. Spahr, and P. Novák. Insertion electrode materials for rechargeable lithium batteries. *Journal of The Electrochemical Society*, 10(10):725–763, 1998. 8

[96] M. Winter, G. H. Wrodnigg, and J. O. Besenhard. Dilatometric investigations of graphite electrodes in nonaqueous lithium battery electrolytes. *Journal of The Electrochemical Society*, 147(7):2427–2431, 2000. 8

[97] J. Wu, J. Xu, and H. Zou. On the well posedness of mathematical model for lithium-ion battery systems. *Methods and Applications of Analysis*, 13(3):275–298, 2006. 23, 24, 39

[98] X. Zhang, W. Shyy, and A. M. Sastry. Numerical simulation of intercalation-induced stress in li-ion battery electrode particles. *Journal of The Electrochemical Society*, 154(10):A910–A916, 2007. 21